Applied Research Laboratory

Technical Report

DEVELOPMENT OF A DUAL-BEAM SWEEP PARTICLE IMAGE VELOCIMETER USING AN EXTENDED SEARCH REGION ALGORITHM

by

19980526 160

PENNSTATE

1855

The Pennsylvania State University
APPLIED RESEARCH LABORATORY
P. O. Box 30
State College, PA 16804

DEVELOPMENT OF A DUAL-BEAM SWEEP PARTICLE IMAGE VELOCIMETER USING AN EXTENDED SEARCH REGION ALGORITHM

by

Gregory A. Meyer

Technical Report No. TR   98-002
March 1998

L. R. Hettche, Director
Applied Research Laboratory   ˒

REPORT DOCUMENTATION PAGE

1. AGENCY USE ONLY (Leave blank)	2. REPORT DATE	3. REPORT TYPE AND DATES COVERED
	August 1997	Thesis; Master of Science

4. TITLE AND SUBTITLE

DEVELOPMENT OF A DUAL-BEAM SWEEP PARTICLE IMAGE VELOCIMETER USING AN EXTENDED SEARCH REGION ALGORITHM

5. FUNDING NUMBERS

6. AUTHOR(S)

Gregory A. Meyer

7. PERFORMING ORGANIZATION NAME(S) AND ADDRESS(ES)

Applied Research Laboratory
The Pennsylvania State University
P. O. Box 30
State College, PA 16804

8. PERFORMING ORGANIZATION REPORT NUMBER

TR- 98-002

9. SPONSORING / MONITORING AGENCY NAME(S) AND ADDRESS(ES)

ARL E&F and ONR Initiatives

10. SPONSORING / MONITORING AGENCY REPORT NUMBER

11. SUPPLEMENTARY NOTES

12a. DISTRIBUTION / AVAILABILITY STATEMENT

APPROVED FOR PUBLIC RELEASE: DISTRIBUTION UNLIMITED

12b. DISTRIBUTION CODE

13. ABSTRACT (Maximum 200 words)

Particle image velocimetry (PIV) is a two-step fluid velocimetry technique which is able to capture 2-D qualitative as well as quantitative velocity information at many points instantaneously with respect to the relevant time scales of the flow field. A pulsing laser light sheet is used in conjunction with an image recording device to record images of fluid embedded particles on one multi-exposed image frame or on successive individual image frames separated by time Δt. Utilizing 2-D statistical techniques on numerous small regions within the image frame, the average particle displacement, hence the average velocity, within each region is determine.

(continued on separated page)

14. SUBJECT TERMS			15. NUMBER OF PAGES
			16. PRICE CODE

17. SECURITY CLASSIFICATION OF REPORT	18. SECURITY CLASSIFICATION OF THIS PAGE	19. SECURITY CLASSIFICATION OF ABSTRACT	20. LIMITATION OF ABSTRACT
UNCLASSIFIED	UNCLASSIFIED	UNCLASSIFIED	

ABSTRACT (Continued)

A dual-beam-sweep PIV system, DBS-PIV, utilizing two continuous-beam Argon-ion lasers, was constructed primarily from existing components to avoid the need to fabricate or purchase major parts. Dual-beam-sweep PIV was chosen because of its use of available continuous-beam lasers and its ability to resolve moderately high velocity flow fields.

New and existing PIV interrogation software were developed for use with real flow field data. A 2-D spatially cross-correlation algorithm to determine the velocity from small regions of a multi-exposed image that makes use of an "extended search region" was developed and tested. Velocity statistics estimated with PIV data obtained with the DBS-PIV hardware and this software for determining velocity values were tested against LDV velocity data. The LDV data were taken in a turbulent pipe flow at locations between $3 \leq y^+ \leq 30$ by Fontaine (1993) at a Reynolds number of approximately $Re_p = 10,000$. Statistical data compared well within experimental uncertainties of both data sets with some deviation in the normal component rms values and at locations closer to the pipe wall than $y^+ = 5$.

ABSTRACT

Particle image velocimetry (PIV) is a two-step fluid velocimetry technique which is able to capture 2-D qualitative as well as quantitative velocity information at many points instantaneously with respect to the relevant time scales of the flow field. A pulsing laser light sheet is used in conjunction with an image recording device to record images of fluid embedded particles on one multi-exposed image frame or on successive individual image frames separated by time Δt. Utilizing 2-D statistical techniques on numerous small regions within the image frame, the average particle displacement, hence the average velocity, within each region is determined.

A dual-beam-sweep PIV system, DBS-PIV, utilizing two continuous-beam Argon-ion lasers, was constructed primarily from existing components to avoid the need to fabricate or purchase major parts. Dual-beam-sweep PIV was chosen because of its use of available continuous-beam lasers and its ability to resolve moderately high velocity flow fields.

New and existing PIV interrogation software were developed for use with real flow field data. A 2-D spatial cross-correlation algorithm to determine the velocity from small regions of a multi-exposed image that makes use of an "extended search region" was developed and tested. Velocity statistics estimated with PIV data obtained with the DBS-PIV hardware and this software for determining velocity values were tested against LDV velocity data. The LDV data were taken in a turbulent pipe flow at locations between $3 \le y^+ \le 30$ by Fontaine (1993) at a Reynolds number of approximately $Re_D \approx 10,000$. Statistical data compared well within experimental uncertainties of both data sets with some deviation in the normal component rms values and at locations closer to the pipe wall than $y^+ \approx 5$.

TABLE OF CONTENTS

LIST OF TABLES

LIST OF FIGURES

NOMENCLATURE

Symbol		Definition
C	-	nondimensional particle concentration per interrogation spot
DNS	-	Direct Numerical Simulation
D_o	-	"Detectability" criterion
d_t	-	diameter of a particle image
d_I	-	interrogation region size in pixels (square)
d_B	-	spatial separation of laser beams
d_p	-	diameter of particle
FFT	-	Fast Fourier Transform
f^+	-	characteristic frequency of flow field as a function of the viscous parameters
Ip_1	-	first image in an image pair
Ip_2	-	second image in an image pair
LDV	-	Laser Doppler Velocimetry
LSV	-	Laser Speckle Velocimetry
L_B	-	distance from laser beam axis of rotation to the test-section's inner wall
M	-	parameter giving pixel size of an interrogation region, also

optical magnification

m	-	x-dimension of correlation map
N	-	parameter describing size of search region R_S
N_i	-	number of image pairs per integration spot
n	-	index of refraction, y-dimension of correlation map
n_i	-	index of refraction of the ith medium
PIV	-	Particle Image Velocimetry
R	-	radius of test section pipe
r	-	distance from test section walk along unit vector directed toward the cross-sectional center of the test-section
Re_D	-	Reynolds number based on pipe diameter
R_S	-	roaming search region
R_L	-	distance from laser beam rotating mirror to measurement point in the test section
Re_θ	-	Reynolds number based on the momentum thickness
Re_*	-	Reynolds number based on the displacement thickness
U	-	average axial velocity
u_l	-	average local axial velocity
$\overline{U^+}$	-	axial mean velocity nondimensionalized with inner wall variable u^*
u^*	-	friction velocity ($u^* = \sqrt{\dfrac{\tau_w}{\rho}}$)

u'^+ - axial rms velocity nondimensionalized with u^*

$\overline{uv}^+$ - x-y Reynolds Stress term without density and nondimensionalized with u^{*2}

V_B - velocity of rotating laser beams

$\overline{V}^+$ - average normal velocity nondimensionalized with u^*

v'^+ - normal rms velocity nondimensionalized with u^*

w - instantaneous out-of-plane velocity component

x^+ - inner wall variable in x-direction (axial), $x^+ = xu^*/\nu$

y^+ - inner wall variable in y-direction (normal), $y^+ = yu^*/\nu$

θ - angle describing azimuthal position

α - diffraction angle for a Younge's fringe

Δ - relative difference

λ - wavelength of laser light

π - pi

τ_w - shear stress at the wall

ω - mirror angular velocity

ν - kinematic viscosity of glycerin

q_c - angle of incidence of laser beam to the test-section's longitudinal axis

Δx - movement of particle in the x- direction

Δz_o - laser sheet thickness

Δt -   time separation between pulses

ρ -   density of medium

q_i -   angle of incidence of a light ray in the ith medium

τ_p -   3 dB response time to an impulsive velocity change

Δu -   local velocity gradient parameter

Δu_s -   slip velocity between particle and fluid

$\Delta \rho$ -   difference between density of particle and fluid

SUPERSCRIPTS

$+$ -   denotes normalization by wall variables, u^* and v

$'$ -   denotes fluctuating value

SUBSCRIPTS

1   -   associated with first image from a double exposer image

2   -   associated with 2nd image from a double exposer image

b   -   denotes association with laser beam

f   -   denotes association with frequency or fluid

I   -   denotes association with interrogation region

i   -   counting index

o   -   denotes a base or constant value

p   -   denotes association with an individual particle

S   -   denotes a roaming search region parameter

s   -   associated with slip velocity

MISCELLANEOUS NOTATION

$\overline{x}, \overline{X}$ -   overbar represents ensemble average of variable x or X

ACKNOWLEDGMENTS

I acknowledge the support and guidance my advisor Howard L. Petrie has provided throughout this study. His example of hard work and creative thinking in all facets of engineering endeavor have been lessons that have made the research both challenging and rewarding. Dr. Petrie's encouragement and persistence in teaching have been a true blessing to me, encouraging tenacity and patience in problem solving and better yet, life. I also acknowledge Dr. Steven Deutsch, for allowing me to use the glycerin tunnel and Ms. Suzanne Grant for originally coding and testing the correlation software.

I would also like to thank the undergraduate students who have worked with me in this study. Denis Williams was very helpful in the acquisition of the data and in preparing this text. Paul Petruzzi was also helpful in the preparation of the text. I also acknowledge the support of Dan Rhodes, Brian Kline and Bob Grove who provided valuable support to the project even though no funds were available. Also Michael Jonson who was always eager to help and encourage.

My wife Amy was my biggest cheerleader and friend along with the little one whom the Lord has blessed us with. Without their patience and encouragement to proceed, the end would have seemed too far away. I also thank my wonderful family, dad, mom, Chris and friends Rob, Eric and Keith.

And with my life, I thank Jesus Christ for His goodness, kindness, mercy and grace at all times. Without Him I am nothing.

Chapter 1

INTRODUCTION

1.1 Rationale for Imaging Velocimetry

Flow visualization is often used in fluid mechanics as a qualitative tool both to identify structures within a flow field and to study their interactions. Quantitative techniques such as laser Doppler velocimetry (LDV) are useful in determining average velocities at a point within a flow field. It is clearly desirable to combine the accuracy of such single-point velocity techniques as LDV with the multi-point nature of flow visualization. Multi-point velocimetry techniques such as particle image velocimetry (PIV) are extensions of flow visualization which can determine instantaneous velocity vectors over a region in the flow at hundreds to thousands of points with an accuracy approaching LDV and hot wire techniques (Adrian (1986), Fingerson et al. (1991)).

Velocimetry techniques which obtain velocity information over a two or three-dimensional region are valuable in the study of a large number of fluid mechanic problems. Multi-point techniques are useful in tracking particulate matter in a two-phase or multi-phase flow as described by Hassan and Canaan (1991) and Farrell (1991). Because of their ability to instantaneously, relative to the smallest time scales, resolve velocities over a given area or volume, image velocimetry techniques are useful in studying unsteady flows, turbulence and flow/structure interactions where single-point measurement techniques have limitations.

Instantaneous information is useful in the study of turbulence where the instantaneous velocity field may look very different from the average field. Studies of coherent structures in turbulence frequently use flow visualization techniques,

conditional averaging techniques or both. PIV information on instantaneous turbulent structure affords new insights into issues of interpreting flow visualization patterns or smoothing of conditionally averaged data. On this basis, Adrian (1988) points out that PIV is similar to large scale direct numerical simulation (DNS). Unlike DNS, PIV allows for the study of complex geometries and complex boundary conditions as well as the study of flows in which the governing equations are unknown or poorly specified, e.g., non-Newtonian fluids. Since turbulent flows usually have a large range of scales of motion, at least for large Reynolds numbers, it is advantageous to have a velocimetry technique which is capable of measuring over areas of the flow which encompass entire flow structures with spatial resolution refined enough to resolve the smaller scales (Adrian (1986) and Eggels (1994)).

Multi-point velocimetry techniques are useful in a multitude of unsteady flow problems. The study of unsteady aerodynamics is enhanced by the ability to acquire qualitative large scale information with one image capture while correlating the motion of the large scale with quantitative velocities. Studies of transient vortices behind an oscillating airfoil (Lourenco and Krothapalli, (1986)) and a rotating wind turbine (Grant et al. (1991)) as well as the oscillating Karman vortex street behind a circular cylinder (Kimura and Takamori, (1986)) are a few examples of implementations of PIV to unsteady flow fields. By acquiring the qualitative and quantitative information simultaneously, the need for single point statistical estimation procedures is significantly reduced.

Image velocimetry techniques have progressed to the state in which they are presently available through a number of commercial sources. Unlike LDV however, image velocimetry systems vary considerably in their modes of operation for both data acquisition and data analysis. Some are optimized for slow speed flows and can capture images at rates equaling current framing rates of electronic cameras. These techniques do not require photographic developing. Other systems are optimized for

moderate and high speed flow fields and use still photography or high speed cameras which require film development and subsequent analysis.

Like LDV, PIV estimates the velocities of particles within the flow field and assumes the particle velocity accurately represents the surrounding fluid velocity. In this regard, PIV techniques vary considerably in the concentration of particles used for the fluid velocity approximating process as well as in the manner in which velocities are determined from the recorded particle information .

The first image velocimetry technique developed uses the laser speckle method as described by Barker and Fourney (1977) and Simpkins and Dudderar (1978). Since that time there have been significant improvements in image velocimetry theory and performance. Comprehensive overviews of the history and status of image velocimetry techniques exist in the literature, the most well known from Adrian (1986), Adrian (1991) and Buchhave (1992). The next section gives a general overview of the existing image velocimetry techniques.

1.2   Image Velocimetry Methods

1.2.1   Particle Tracing Velocimetry

Particle tracing velocimetry (PTV) is one of the oldest and simplest types of image velocimetry. As purely flow visualization, particle tracing was first used by Prandtl and Tietjens (1934) in fluids using simple lighting sources. Today, seed particles within the flow field are illuminated by a laser light sheet and the "traces" of the illuminated particles are recorded. The tracing effect is achieved by either pulsing or chopping a laser beam, so the duration of the pulse is long enough to cause the particle image to streak, or by using a continuous beam effectively shuttered with a

digitally shuttered electronic camera, e.g., electronic camera with 1/30 sec. framing rate. Though obtaining particle traces is relatively simple, measuring their lengths is not trivial. Image processing algorithms must be developed for the specific methods used by whomever is carrying out the measurements.

In general, particle tracing does not possess the spatial and temporal resolution nor the dynamic range possible with other image velocimetry techniques. This is due to the relatively large image trace lengths required and the uncertainty in measuring the length of the image traces. This uncertainty may be prohibitive since it is difficult to quantify errors associated with the image processing techniques required to automatically process the large number of particle images required for statistical averaging, especially for highly turbulent flows. Furthermore, if seeding concentrations become large and relatively high turbulence intensities exist, trace overlap becomes a problem for image processing software. As a consequence of low seeding densities and of the Nyquist sampling criterion, any characteristic scale of the flow field with a wavelength shorter than twice the average distance between particles cannot be retrieved from the data due to aliasing effects (Agui and Jimenez (1987)). Methods of improving particle tracing are discussed by Willert and Gharib (1988) and Altman (1991).

1.2.2 Particle Tracking Velocimetry

Particle Tracking Velocimetry is like particle tracing velocimetery in that small particle concentrations are used. It differs from PTV in that short, relative to the smallest scales of the flow field, laser light pulses are used to record particle positions at some time t_1 and some later time, t_2, rather than continuous traces. Particle image displacements are recorded electronically or photographically. As

described by Agui and Jimenez (1987) and Gharib and Willert (1989), particle concentrations are small enough such that individual particles may be tracked from exposure to exposure, with the measured displacement between individually tracked particle positions providing estimates of the surrounding fluid velocity. Each double-exposed particle produces a velocity vector. Particle tracking is often employed when flow visualization is needed along with quantitiative velocity data or when particle seed density is low.

Particle tracking in general provides fewer velocity vectors per unit volume of the flow field than high particle concentration image velocimetry methods, a concequence of low seeding density. The reliability of particle correspondence may furthermore be uncertain, especially for large pulse separations, Δt (Shekarriz et al. (1992)). Since individual particle images must be tracked, overlapping of particle images may necessitate the use of edge detection algorithms along with other image processing algorithms to aid in the tracking process.

1.2.3   Particle Image Velocimetry

Particle image velocimetry is presently the most common velocimetry system throughout the literature. Particle image velocimetry systems have two generally separate subsystems, the image acquisition system and the image interrogation system. The image acquisition system uses a thin, pulsing laser light sheet to illuminate the fluid flow; the rationale for using lasers as light sources is described in chapter 2. Because of the finite thickness of the laser light sheet, acquisitions of particle images are taken over a three-dimensional space in which the third dimension of the light sheet is much smaller than any other dimension. Particles within the flow field are illuminated within a pulsing laser light sheet in such a way that particle

positions within the light sheet are recorded at some time t_1 and some t_2 later. Some systems use more than two pulses (Keane and Adrian (1991)). Particle image displacements are recorded electronically or photographically. The resulting multi-exposed particle displacement information is used to determine the velocity within the recorded field of view.

The recorded images are "interrogated", usually in a piecewise procedure, by a statistical analysis of small regions of the image known as interrogation spots or volumes. Unlike PTV, or particle tracking, in which only one particle trace is needed to obtain a velocity for a given position within the flow field, there are typically several particle image pairs within each PIV interrogation volume. In fact, having enough particle image pairs per interrogation volume, i.e., a high particle image pair concentration, is required for good results. The particle image concentration, however, is such that individual particle images are discernable within the interrogation volume. The result of the statistical analysis is some sort of average of the particle image displacements within the interrogation volume. Velocities are found by dividing the particle displacements by the time over which the displacements took place.

1.2.4   Laser Speckle Velocimetry

Laser speckle velocimetry (LSV) is a planar multi-pulse technique like particle image velocimetry. A laser light source is pulsed in such a way that particle positions within the light sheet are recorded at some time t_1 and some t_2 later. The resulting double exposed displacement information is used to determine the velocity within the recorded field of view. Like with PIV, the laser light sheet is pulsed at very short time separations, smaller than any relevant time scales within the flow

field, and particle images are recorded. LSV differs from PIV in that particle seeding concentrations, which are at very high levels, cause a high level of seemingly random particle image overlapping. The overlapping produces a speckle pattern from which phase information is extracted and converted to velocity.

Generally, individual particles are not discernable in LSV images. Laser speckle velocimetry requires high particle seeding densities such that the flow field may no longer be the original flow field of study due to modification by the multi-phase flow effects. Moreover, as the algorithms and programming methods are sensitive to the quality of particle images and recording methods, laser speckle velocimetry may not be as ideal or user friendly as particle image velocimetry. The LSV method generally requires special recording optics and a relatively complex data processing system to extract information from the speckle patterns resulting in an increased sensitivity to processing inaccuracies (Adrian (1984, 1986), Lourenco (1986)).

1.2.5   3-D Velocimetry Techniques

There are also a number of three-dimensional image velocimetry techniques. These are usually based upon recording particle images with a two camera system in which two fields of view provide three-dimensional information. Such a system is described by Adrian (1986). A novel system presented by Komine and Brosnan (1991) uses the Doppler shift created by the moving particles through a laser light sheet. Velocities are determined from an optical frequency-to-intensity image converter which yields images whose intensity is directly correlated to the Doppler shift. Grant et al. (1991) use one camera and a mirror system to impose two frames of reference onto one film plane. Using a mathematical method described by Hall

(1979), Grant is able to extract the third component of velocity. Grant et al. (1991) also describes holographic three-dimensional image velocimetry systems which use software developed for stereoscopic PIV to extract information from holograms. Other three-component image velocimetry systems have used magnetic resonance (Durnoulin et al. (1987)) and acoustic measurement methods (Johnson (1976)).

Three-dimensional velocimetry techniques are obviously desirable. They are, however, usually more computationally demanding and hardware intensive. At the present time, their practical implementation is not as developed as their two-dimensional counterparts, especially particle image velocimetry. This may be prohibitive to many potential users of an image velocimetry system.

1.3   Motivation and Objective of the Present Study

The motivation behind this study was the need to develop and experimentally qualify an image velocimetry system to aid in the interpretation of LDV velocity measurements taken within an existing unsteady turbulent flow field. The flow field is a fully-developed turbulent pipe flow, with glycerin as the fluid medium, with a small Gaussian shaped wall protrusion mounted on the acrylic test-section wall.

Fontaine (1993) studied the flow field about the protrusion in order to understand its effects on Reynolds stress production within the buffer region of the pipe flow near wall region. In an attempt to resolve the form of the dominant flow structures downstream of the protrusion, Fontaine (1993) used conditional averaging techniques. Though LDV measurements are routinely made in unsteady turbulent flow fields, the interpretation of conditionally averaged data is often difficult. An image velocimetry system, providing an instantaneous velocity "picture" of the desired flow field, would allow an accurate interpretation of conditionally averaged

LDV data.

Commercial image velocimetry systems are typically very expensive and afford little to no variability in their velocity estimating methods. The ability to vary and independently control velocity estimating procedures is desirable when analyzing complex flow fields in which one method of velocity analysis, or one parameter within the process, may not be optimized for the given flow field characteristics. Commercial systems however are usually optimized for processing speed, which is highly desirable when calculating thousands of velocity vectors per recorded particle image frame.

Therefore, an image velocimetry system was developed with an attempt to provide a high degree of variability within the velocity estimation procedures while optimizing processing speed and reducing cost. Because of the inherent advantages described above of particle image velocimetry over other image velocimetry techniques, PIV is used for the present study. Chapter 2 is devoted to describing in detail general PIV theory while chapter 3 explains the present study's interpretation and development of a practical particle image velocimetry system.

The objective of this study is to develop and test a working PIV system for which no major parts need be designed or purchased. To this end, a dual-beam-sweep PIV system is constructed from existing laser and optical components. Dual-beam-sweep PIV was chosen because of its use of available continuous beam lasers and its ability to resolve moderately high velocity flow fields.

New and existing PIV interrogation methods are implemented for use with real flow field data. A spatial autocorrelation algorithm making use of an "extended search region", described in chapter 3, is tested. The extended search region autocorrelation algorithm is used in an attempt to decrease limitations and errors associated with traditional algorithms. Particular attention is given also to processing time and programming simplicity as compared to traditional PIV algorithms.

System software for determining velocities and velocity statistics are developed and used to test PIV data against LDV data taken by Fontaine (1993) in a glycerin tunnel at a pipe Reynolds number of approximately $Re_D \approx 10,000$. The high viscosity of the glycerin facilitates examination of the near wall region because the flow scales are large. The focus is on the near wall region, between $2 \leq y^+ \leq 30$, of the fully-developed turbulent pipe flow and near the small wall mounted Gaussian shaped protrusion previously studied by Fontaine (1993).

Chapter 2

PIV THEORY AND PRACTICE

2.1   Introduction

There are a number of reviews such as Adrian (1991) and Buchhave (1992) which describe in detail the theory and practice of image velocimetry techniques currently used throughout the literature and the techniques which hold promise for the future. This chapter is not a complete literature review such as the aforementioned writings, but focuses on conventional PIV theory and practice as it exists in the literature. Conventional PIV denotes high image density and 2-D, statistical analysis, either optical or digital, of recorded images. Emphasis is placed on principles which are fundamental to all PIV techniques with aspects which are relevant to the present DBS-PIV study.

The basic principle underlying PIV, as shown in Figure 2.1, is to measure localized particle image displacements in two dimensions within small, specified subregions of the overall field-of-view called "interrogation" regions. To record the particle displacements, a pulsing light source is used. The assumptions are made that seed particles, most often added to the fluid, follow the flow field well enough to accurately describe the motion of the fluid and that these particles all move at nearly the same velocity within a given interrogation region (Adrian (1991), Gharib and Willert (1991)).

Interrogation regions or spots are the regions in the flow field where the displaced particle image field is analyzed to determine one unique velocity vector corresponding to that position. The interrogation region size is either preset or variable depending upon the interrogation method employed. For the entirety of this

Second image of
particle "A" at time t+Δt

(X_2, Y_2)

First image of
particle "A" at time t

(X_1, Y_1)

ΔY

ΔX

$$U = \lim_{\Delta t \to 0} \frac{X_2 - X_1}{\Delta t}, \quad V = \lim_{\Delta t \to 0} \frac{Y_2 - Y_1}{\Delta t}$$
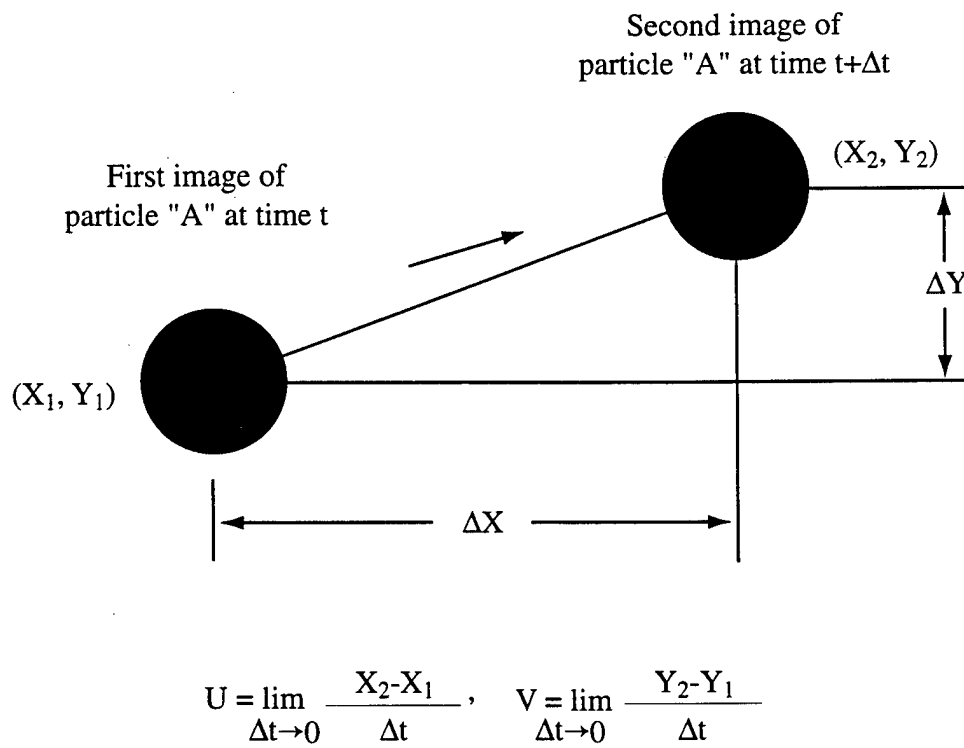
Figure 2.1 Basic principle of PIV is to measure distances between
particle image displacements (Abbot, [1994])

manuscript, interrogation volume and interrogation region or spot are used interchangeably and the interrogation region is assumed to be three-dimensional in real space and two-dimensional in image space.

Generally, a laser light source is double pulsed, though more than two pulses are often used, so particle positions within the light sheet are recorded at some time t_1 and then some later time t_2. Referring to Figure 2.1, particle images which correspond to the first exposure are designated Ip_1 and the displaced second exposure images are designated Ip_2. Though the end objective of the interrogation process is to determine some average particle displacements between all Ip_1 and Ip_2 images for a given interrogation region, the fundamental means of the process is to accurately *match* corresponding Ip_1 and Ip_2 images within the region (Hassan and Canaan, (1991)).

Matching of image pairs is made possible on the supposition that a unique grouping of particle images exists within each interrogation region which only correlates well with itself at future times. If the time separation, Δt, between light sheet pulses is small relative to the smallest time scales of the flow field, then Ip_2 images will closely represent the same respective grouping as the original Ip_1 images. Furthermore, each Ip_2 image within the second grouping is assumed to proportionately shift spatially from its corresponding Ip_1 image within the first grouping. This is not totally true since some particles will leave the region and some particles will enter the region over the time between pulses, Δt, reducing the probability of valid particle image matching. Matching of corresponding images within the interrogation region is quantitatively measured using statistical techniques. The resulting double exposed particle image displacement information and laser pulse time separation are used to determine the velocity within the interrogation region.

Statistical techniques are used in conjunction with high seeding densities in order to avoid having to track individual particles. A sufficiently large number of

particles within the interrogation volume greatly increases the probability of the existence of a unique grouping or, more precisely, a grouping that will only correlate well with itself at future times (Keane and Adrian (1991)). The assumption of a unique grouping is not valid if particle seeding is too low. Typical image concentrations cited within the literature have ranged between 4 image pairs to upwards of 20 image pairs per interrogation region. Adrian (1991) refers to this as "high image density" PIV.

Similarly, a unique grouping is not maintained between times t_1 and t_2 if the interrogation region contains high velocity gradients. Since velocities are statistically averaged over the area of the interrogation region, any gradient information within the interrogation spot is lost and the measured velocity is biased by the gradient (Adrian (1991)). Adrian (1991) also points out that the displacement between particle images at t_1 and those at t_2 should also be less than a quarter of the light sheet thickness Δz_0 in the out-of-plane dimension and no greater than one quarter of the interrogation dimension d_I in the in-plane direction for good results with most methods of image analysis. Specific errors associated with PIV are described in detail in section 2.4.

PIV image displacements are acquired by any number of photographic or electronic imaging processes which in return are interrogated for the velocity field using one or a combination of statistical averaging techniques. Examples of the foremost acquisition and interrogation techniques follow.

2.2   PIV Image Acquisition Techniques

2.2.1   Particle Image Illumination

The purpose of any image recording technique is to effectively illuminate and accurately record particle images over known time intervals. Though white light sources are sometimes used with PIV systems, most systems use lasers because they provide collimated, high intensity beams of light at short pulse durations. This allows for high spatial and temporal resolution measurements over a wide dynamic range (Abbott (1994)). Double-pulsed Nd: YAG and continuously pulsed Cu-Vapor lasers, in conjunction with one or more appropriate lenses, are most often used because of their ability to produce high power, short pulse durations and pulse separations on the order of a few microseconds to 10's of microseconds (Adrian (1991)). Ruby lasers are rarely used since they require a relatively long time (~ 20-30 sec.) to re-energize between double-pulses, increasing alignment difficulties and negating the possibility of time-series measurements. Furthermore, the red wavelength of the Ruby laser is generally highly attenuated when used in a medium other than air.

Because of their availability, continuous beam Argon-ion lasers are used in combination with beam choppers, rotating mirrors or scanning mirrors to produce a pulsed light source for PIV. When using a continuous beam laser with a beam chopper, the light sheet is created by passing the beam through a cylindrical lens while the pulsing is created by the chopper periodically blocking the beam. In this way, pulse separation is controlled by varying the chopper rotational velocity and the chopper geometry. An example of a PIV system based on an Argon-Ion laser, beam chopper and CCD camera for recording particle images, as used by Willert and Gharib (1991), is shown in Figure 2.2.
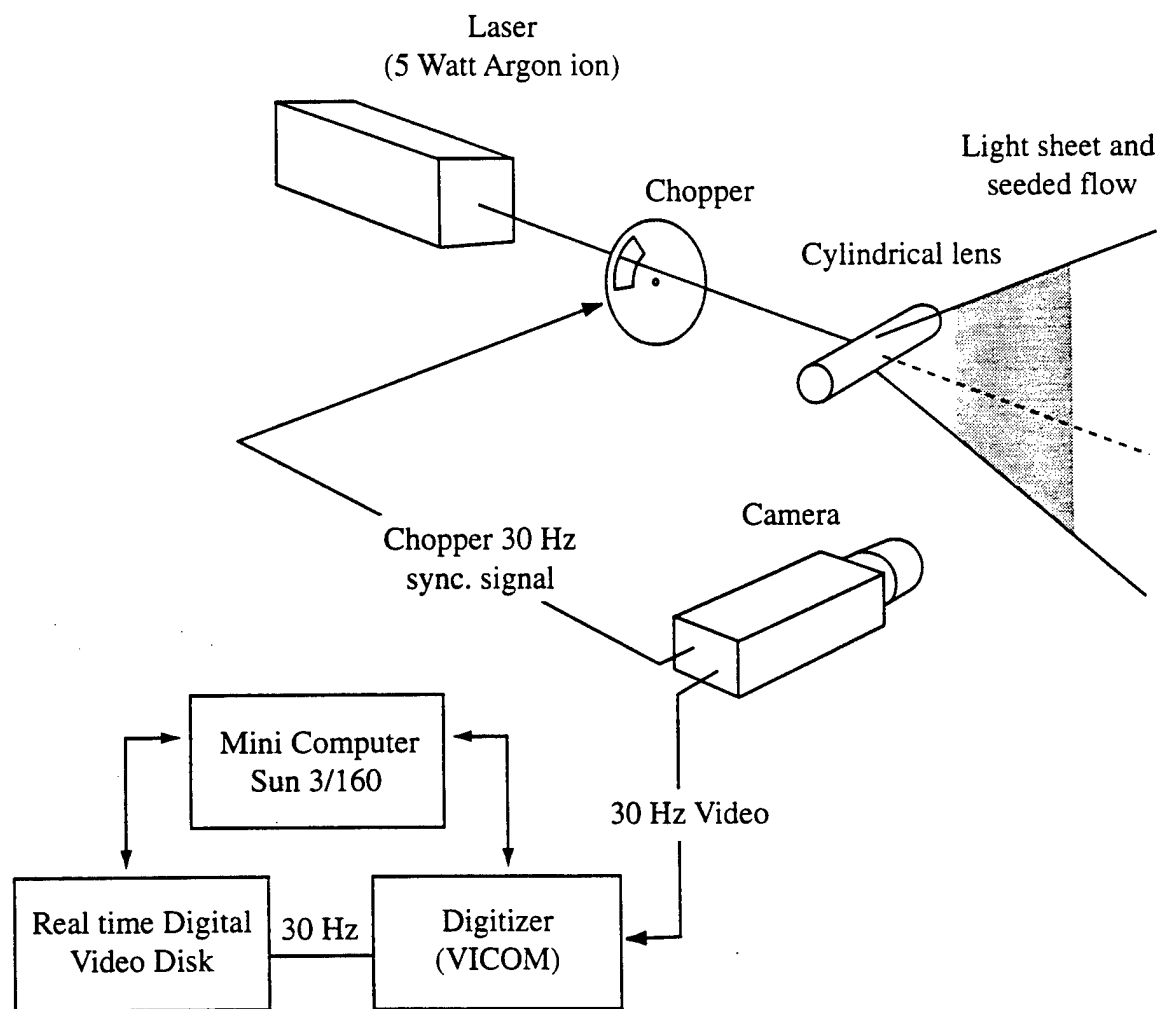
Figure 2.2 Experimental schematic from Willert and Gharib (1991)

When used with rotating or scanning mirrors (Rockwell et al. (1993)), the continuous beam is traversed over the desired field of view through a rotating multi-faceted mirror or single facet oscillating mirror system. If the beam is traversed quickly enough, a pulsing effect results, analogous to a pulsing light sheet. Kawahashi and Hosoi (1991) used the above multi-faceted technique with 2 rotating beams. This offers greater seed illumination intensities over single beam techniques in which the faceted mirror rotates much faster in order to move the illumination beam twice through the area of interest, i.e, the time of exposure for a given particle and beam intensity is less for single beam techniques. This particle illumination technique is often termed *laser scanning*, but recent developments in 3-D PIV using "laser scanning" light sheets to obtain three-dimensional velocity information are in the literature. Therefore, to eliminate possible confusion, Dual-Beam Sweep PIV (DBS-PIV) as termed by Kawahashi and Hosoi (1991) is used throughout the rest of this text in referencing sweeping beam light sheets. An example of a dual-beam sweep system is shown in Figure 2.3.

2.2.2   Particle Image Recording

Figure 2.4 displays a PIV optical schematic as given by Keane and Adrian (1990) and shows the image recording process which models virtually all basic PIV acquisition systems. M is the magnification, d_I the diameter or length scale of the interrogation region and Δz_0 the thickness of the light sheet. Image recording is typically accomplished using either a photographic or digital camera with the image plane of the camera corresponding to the measurement plane of the laser light sheet.

Photographic camera formats from 35 mm to 8x10 have been used for image acquisition. Photographic media is often preferred over electronic cameras because of
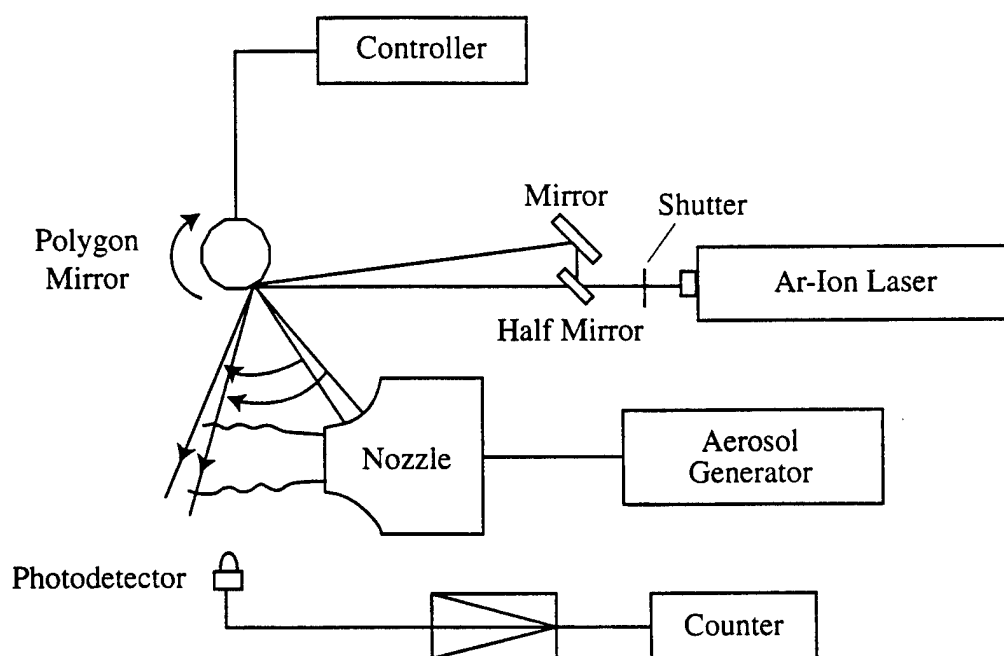
Figure 2.3 Experimental schematic for dual-beam-sweep speckle velocimetry
from Kawahashi and Hasoi (1991)
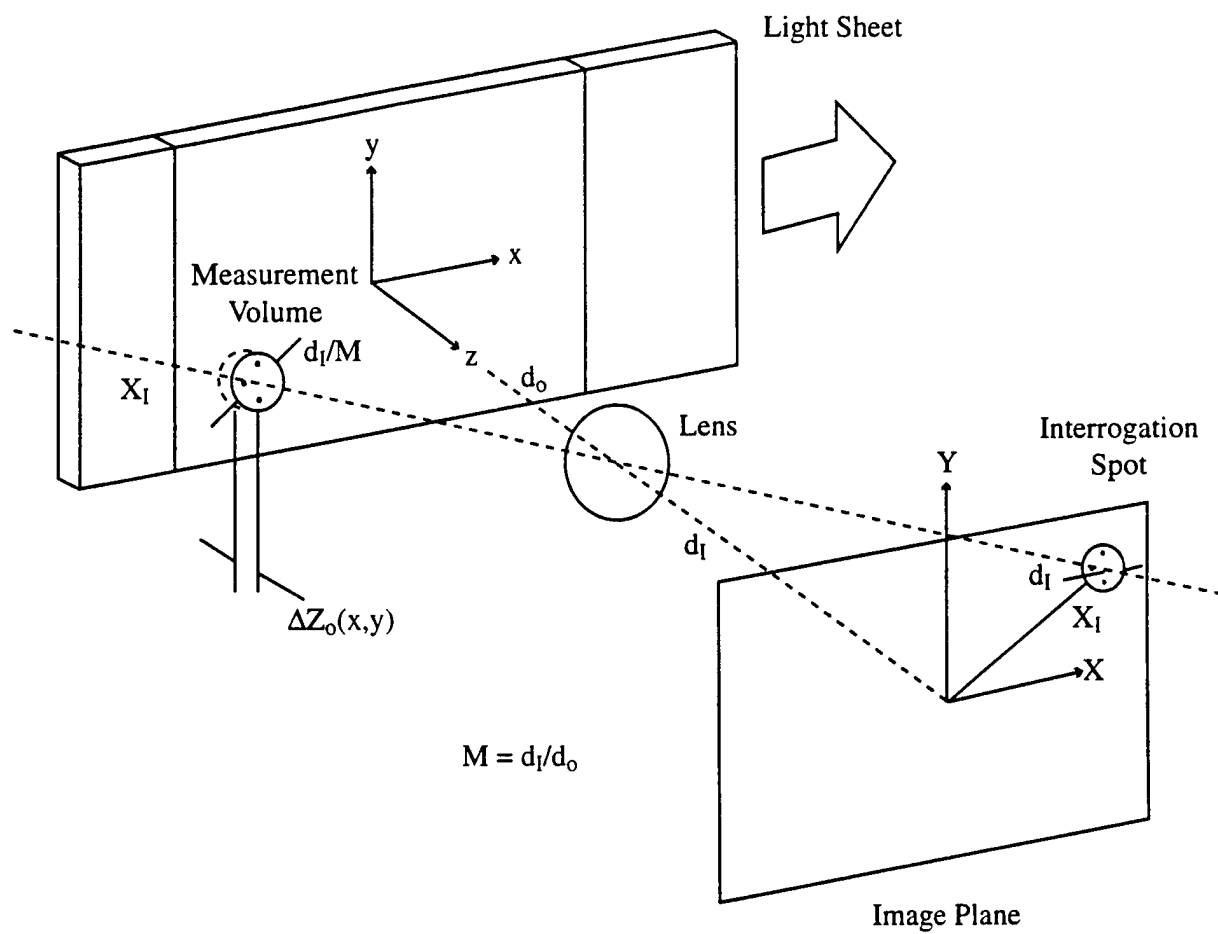
Figure 2.4 Experimental schematic from Keane & Adrian (1990)

the superior spatial resolution; 100-300 line pairs/mm compared to 50 line pairs/mm for higher resolution electronic cameras. Formats of film are larger than array sizes available with digital cameras, giving larger possible fields of view per image acquisition and allowing further standoff distances from the flow field while retaining magnification. Photographic spatial resolution is generally high enough to resolve very small particles at high seed density while maintaining a significant field of view. Lourenco and Krothapalli (1987) detail the role and performance of photographic parameters for PIV.

The spatial resolution of typical electronic cameras is on the order of 500 to 600 pixels square. Solid-state digital cameras with photodetector arrays as large as 4096 x 4096 are available however. These high resolution digital cameras match the resolution of some types of photographic film with similar sensitivities, but generally have low sync rates.

When a digital camera is used, the time separation between the laser pulses can be smaller than the sync rate of the camera in which multiple exposures of moving particles are recorded on the same image frame. The time separation may also match the sync rate of the camera, or be smaller than the sync rate when frame "straddling" is used, recording each laser pulse on separate image frames. The sync rate of standard digital cameras is $1/30^{th}$ of a second but cameras with sync rates greater than 40 KHz are currently available; however, the latter are generally prohibitively expensive and have low resolution. With photographic techniques, the minimum pulse separation is limited only by the light source itself and the sensitivity of the film.

An advantage of recording on electronic media is that overall processing time is reduced since no film development or subsequent digitization is necessary. Furthermore, recent developments in PIV have realized near real-time processing and displaying of velocity fields using electronic recording media. Willert and Gharib

(1991) as well as Fincham, Blackwelder and Spedding (1991) detail the characteristics and general performance of a digital PIV system.

2.2.3   Directional Ambiguity

PIV methods may suffer from a 180° directional ambiguity if the order in which particle images are recorded in a double-pulsed system is not readily discernible with standard image analysis. This ambiguity arises from the inability of statistical methods to distinguish images which were recorded from the first laser pulse from images recorded from the second or additional pulses. The directional ambiguity does not exist for consecutive image frame acquisition techniques since the first exposure images are separated physically from the second exposure images.

Image shifting as first termed by Adrian (1986) is a technique whereby the second image of an image pair is artificially displaced by a known direction and distance. By properly choosing the shift value, Figure 2.5, it is possible to ensure that, within the field of interest, the second particle image is shifted to a displacement position which lies on the positive side of the first image. Once a preferred direction is defined as positive, in either one or two dimensions, the detected image displacements are always in a positive direction. The false displacement vector is later subtracted off disclosing the correct vector direction. In this way, any directional ambiguity is overcome using standard image analysis. Image shifting is analogous to frequency shifting in LDV and is the only developed technique which does not prescribe limitations on the maximum positive and negative measurable velocities.

A number of image shifting methods exist with the most popular developed by Adrian (1986). He uses a rotating mirror between the laser light sheet and the

IMAGE SHIFTING
(Image Plane of Camera)

ΔY

First Image

2nd Image with Shift

ΔX

X_S = Shift Vector

ΔX

2nd Image no shift
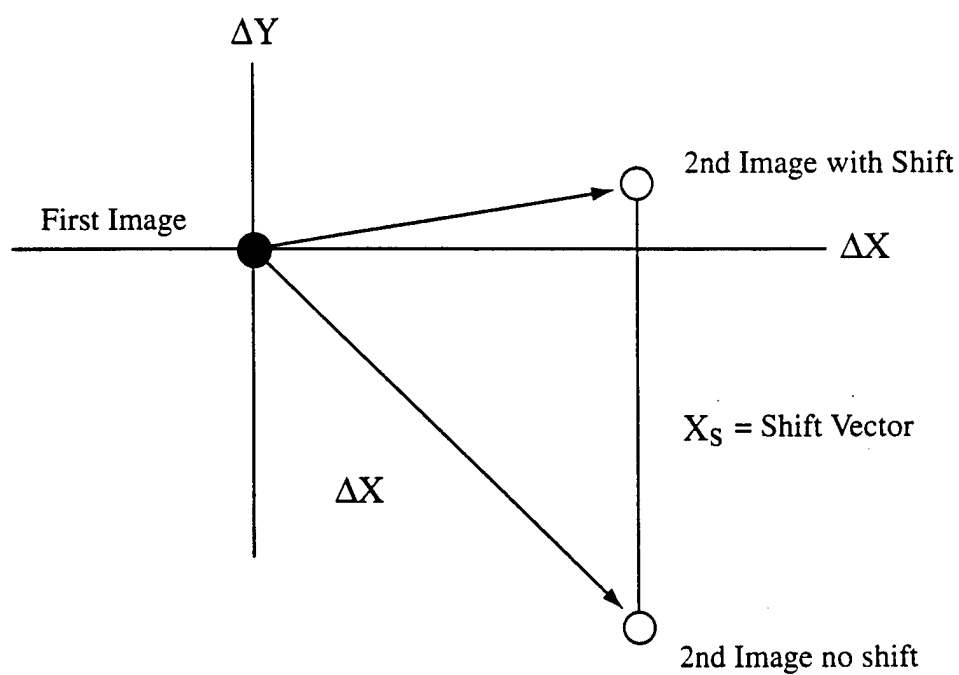
Figure 2.5   Vector plot of false velocity (image shift) imposed on velocity field

recording optics. The slight change in mirror angle between images of the same image pair shifts the perspective of the recording optics relative to the laser light sheet. This perspective change imposes an artificial vector displacement or image shift on the film plane. Rotating and scanning mirrors have been used for this purpose and are well suited for image shifting for all but the highest velocity fields. Due to the elevated dynamic loads induced by high rates of revolution, an all electronic image shifting system is required with higher velocity flows.

Birefringent electro-optical crystals , usually calcite crystal, have been employed for high velocity image shifting (Landareth and Adrian (1988)). The crystal passes light which is polarized along its principal axis without a spatial shift. Light polarized 90° from the principal axis of the crystal is spatially shifted by some amount directly dependent upon the length of the crystal. Laser illumination beam(s) polarity must be alternately switched between pulses with either a Pockels cell within the optical path of a single double pulsed laser or two synchronized lasers with orthogonal states of polarization. The resulting image shift is effectively the same as the shift produced by the above rotating mirror system. Electro-optical image shifting, though relatively simple and powerful, is dependent upon crystal length and hence, a number of different crystals are needed to possess any image shifting flexibility.

Another technique of determining particle displacement direction includes pixel translation within a charged coupled device (Abbott (1994)). Array lines within a CCD camera are shifted out of line to produce a false displacement in pixel space. This procedure usually requires line shifts of four lines or more to ensure velocity ambiguity resolution. The more lines that need to be shifted, the lower the allowable velocity range.

Willert and Gharib (1991) use a technique which negates the directional ambiguity by recording particle images on separate frames with a digital camera with

a frequency equal to the camera framing rate. In this way, a spatial cross-correlation is carried out to determine particle displacements between frames. No directional ambiguity exists because images from the first frame are known to exist before images on the second frame and so on. Commercial systems presently exist which use either "frame straddling" CCD cameras that can buffer two exposures onto separate frames with time separations as small as 2 μs or CCD cameras which have a frame store buffer on the CCD chip to store the first frame allowing the CCD to quickly, on the order of 1 μs, capture a second frame.

Other means of image shifting include pulse tagging and color tagging in which the second image is marked in some optical fashion (Grant and Lui (1990)) or with color coding (Post et al. (1994)) to differentiate from the first image.

2.3   PIV Image Interrogation Techniques

2.3.1   Data Preparation

Statistical interrogation techniques are designed to determine average particle image displacements over some region of interest within the flow field. Because of the relatively large fields of view and particle densities in PIV, and therefore the amount of data to be processed, an automated interrogation method is a necessity.

As stated by Adrian (1986), an interrogation region can contain between 64^2 to 512^2 pixels, depending on the interrogation procedure used, that contain particle image information which must be analyzed numerically. Each photograph may contain more than 10^4 interrogation regions generating over 10^9 pixels of information. In light of this, an acquisition system must be computationally efficient and fast.

PIV image analysis requires digitizing image information at some point. Even

techniques which use virtually pure optical means to extract velocities require digitization of optical information at the last stage of the process with some subsequent digital analysis to determine the velocity vector. These methods are expensive and difficult to implement and generally lack the resolution of their numerical counterparts (Buchhave (1992)). Common 2-D autocorrelation, 2-D spatial cross-correlation or a "hybrid" (Adrian (1986), Buchhave (1992)) technique using optical Young's fringes and a 2-D FFT to determine the spatial spectral content of the image information all require digitization of image information at different times during processing.

PC-based digital frame grabber boards are generally used in combination with a CCD camera to digitize particle displacement information either directly from the flow field, in which case no further digitization is required before processing, or from a photograph. If recording from a photograph, other high resolution scanning equipment, which may prove to be quicker and more flexible, exist such as the Nikon "Coolscan" which is designed to digitize photographic negatives, positives or prints with a 2592 x 3888 pixel resolution or the Nikon LS3510AF which digitizes large numbers of photographs automatically with resolution as high as 5000 x 5000 pixels per frame.

2.3.2   Image Processing

Preprocessing of the digitized image field is generally carried out prior to statistical image analysis to enhance contrast between individual particle images as well as between particle images and the background. Though image processing is not always needed, optimizing image to background contrast can significantly improve velocity data integrity and accuracy as pointed out by Guezennec and Kiritsis (1990).

They show that correctly thresholding image grey levels to increase image to background noise contrast can be the most important step in obtaining accurate velocity data. This is founded on the fact that making accurate image displacement measurements is dependent on accurately determining image centroids. Guezennic and Kiritsis (1990) also found background image noise to be a factor. The more background noise, noise referring to exposed pixels which are not part of a real particle image, the greater the error in measured displacement and higher the number of spurious displacements. Image processing also reduces nonuniform background illumination which may increase the number of spurious displacements and increase the number of "dropouts" where no valid displacements are detected.

Throughout the literature, image processing techniques used on particle images generally utilize at least two procedures, pixel grey level thresholding and some form of filtering. Filtering is typically a convolution of the image field with an N x N mask or filter intended to reduce background noise. The specific convolution must be tailored for the image field of interest and often incorporates morphological operations. Small values of N, around 3 to 5, tend to reduce noise associated with individual of small groupings of pixels (Guezennec and Kiritsis (1990)) and improve image edge detection through a smoothing process. Thresholding is simply choosing a grey level value between 0 and 255 such that pixels with grey levels above or below the threshold value are considered either valid particle images or background. Histograming of pixel grey level values is often used throughout the literature to systematically optimize threshold values on a frame by frame basis.

2.3.3   Statistical Analysis of Particle Images

The following sections are a basic overview and description of the most relevant statistical techniques for determining particle image displacements. These techniques are the Young's fringe optical technique, the 2-D FFT autocorrelation technique used with multiple-exposure single frame image data and the spatial cross-correlation technique which is also used with multiple exposure single frame image data or image data recorded on separate yet consecutive frames using electronic cameras. All of these techniques effectively measure the average spatial frequency of the particle image separations within an interrogation region and directly correlate the measured spatial frequency with a characteristic displacement. This displacement is proportional to the velocity within the specified region.

2.3.3.1   Young's Fringe Optical Interrogation

A theoretical analysis and comparison of both Young's fringe and 2-D FFT derived autocorrelation methods is detailed in Adrian (1988). With the Young's fringe method, a coherent light source is used to illuminate a small region on a film positive. The resulting sinusoidal interference pattern (Young's fringes), shown in Figure 2.6, found in the Fourier plane of the lens contains velocity information. The velocity is normal to the fringe direction while velocity magnitude is given by

$u = \dfrac{\lambda}{M \cdot \Delta t \cdot \sin(\alpha)}$, the velocity being inversely proportional to the diffraction angle α

relative to the first fringe maximum. Here, λ is the laser wavelength and M the magnification. The Young's interference fringes are digitized and a 2-D Fourier transform is used to extract the fringe spacing and orientation from the resulting
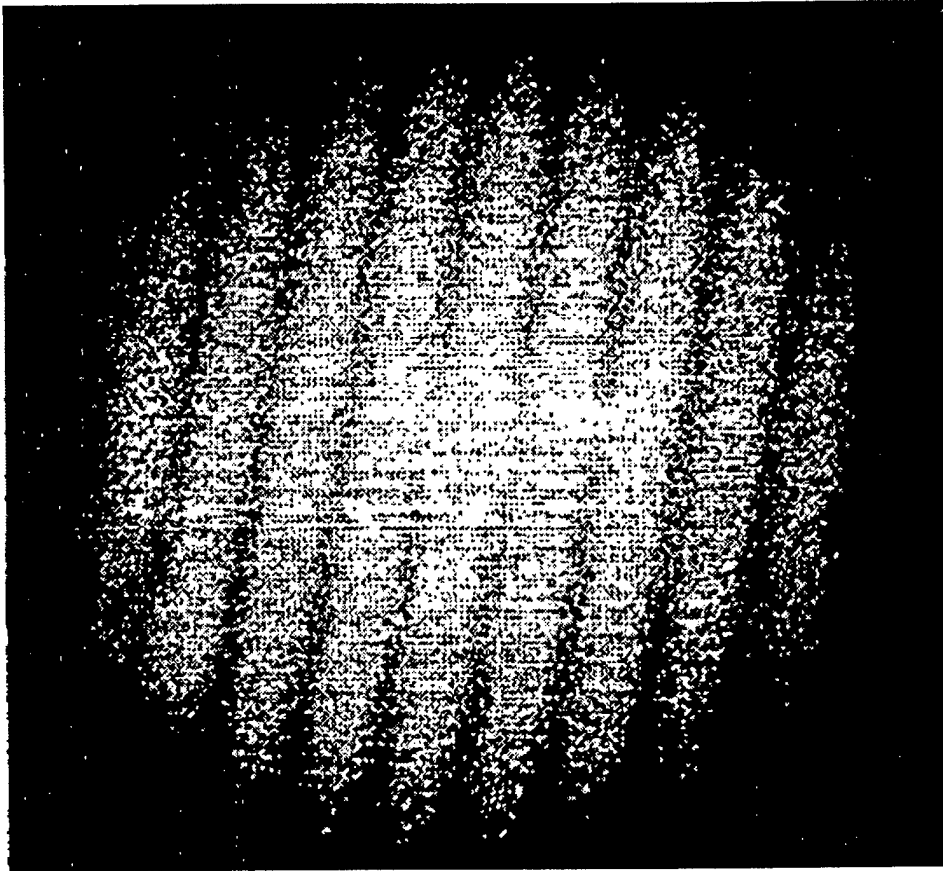
Figure 2.6 Illustration of Young's Fringes

(a)

(b)
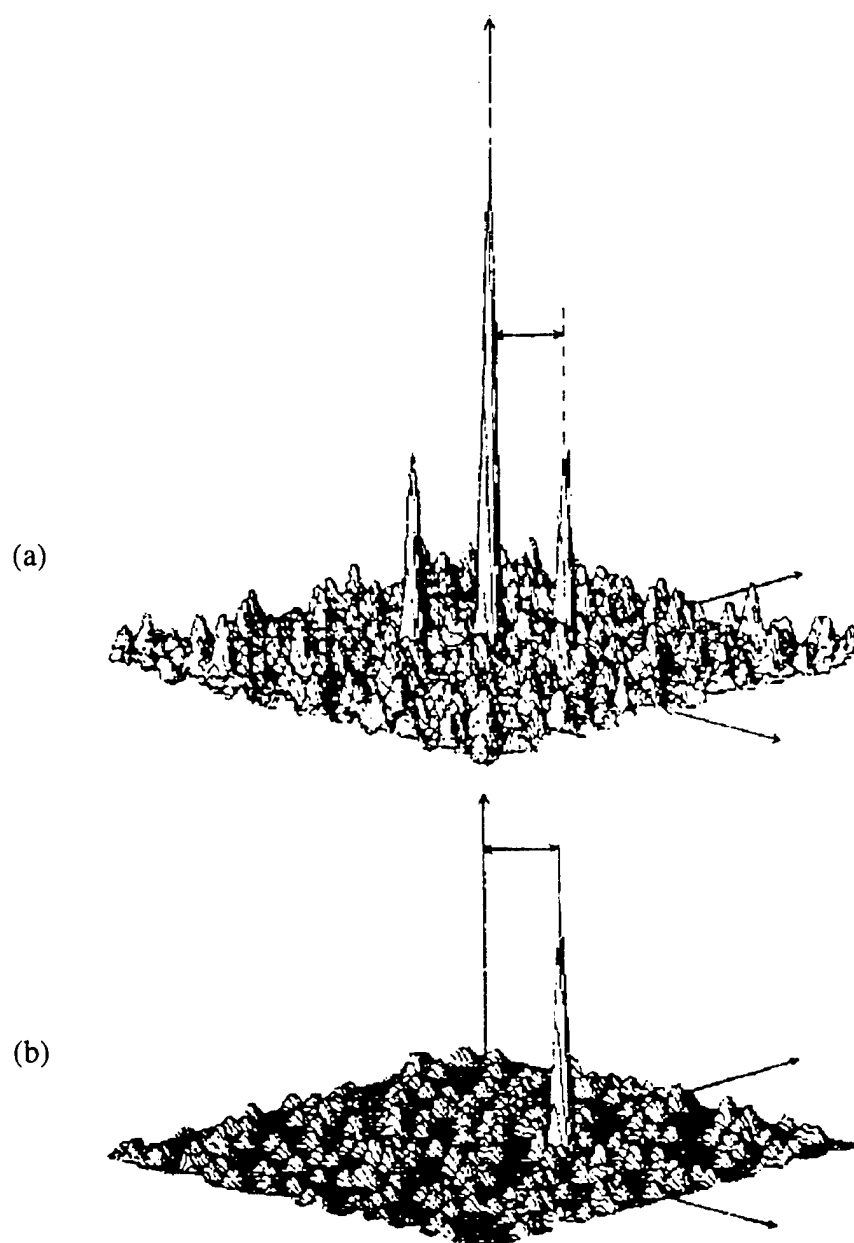
Figure 2.7   (a) Typical autocorrelation function using Young's fringes and autocorrelation
             (b) Typical correlation function using spatial cross-correlation
             (Keane & Adrian, 1991)

autocorrelation. The autocorrelation contains the zero displacement self image correlation and two symmetric correlation peaks due to the particle group displacement within the interrogation region. A typical plot of the resulting autocorrelation, or zeroeth order peak, and displacement peaks are displayed in Figure 2.7(a). Huntley (1989) gives an overview of algorithms used with the Young's fringe approach.

2.3.3.2   2-D FFT Autocorrelation

It is possible to bypass the optical transform and digitally transform the particle image displacements by using two 2-D FFT's. Using an FFT, rather than an optical Young's fringe, for the first transformation allows for greater variability in the process methodology because of its all digital nature while sacrificing very little processing time. For example, with the Young's fringe method a low power laser with a set beam diameter, typically 1 mm, defines the interrogation spot size. Though optical magnification can be varied during data acquisition, there is no capability to easily define a variable interrogation region relative to the actual flow field or relative to the digitizing array's pixel parameters. This is significant due to the importance of particle image density and diameter relative to pixel and interrogation region sizes (Keane and Adrian (1990), Adrian (1991)) described in section 2.4.4. Numerically calculating the first 2-D FFT adds the possibility of actively filtering and further processing image information.

2.3.3.3   Spatial Cross-correlation

The spatial cross-correlation approach to computing the average particle displacement in the interrogation region is basically a histogram method. It is most often implemented using consecutive image frame image data (Willert and Gharib (1991), Hassan and Canaan (1991) and Keane and Adrian (1991)), but is also used with multiple-exposure single frame image data (Sridhar et al. (1991), Dong et al. (1992)). When used with the latter, the spatial cross-correlation is analogous to the 2-D FFT autocorrelation approach.

An interrogation region is defined where the velocity is to be determined. The pixels in this interrogation region are compared, using a cross-correlation, to a search region defined over the region of pixel space where the corresponding displaced particle images are expected. Typically, the spatial cross-correlation function is defined as the statistical expected value C_{fg} (m, n) = E[f(m,n) g(m, n)] of the particle image distribution functions f and g (Willert and Gharib (1991)). In discretized form, the correlation is:

$$C_{fg}(m, n) \ = \ \frac{\sum_{i=-\infty}^{\infty} \sum_{j=-\infty}^{\infty} f(i, j) g(i+m, j+n)}{\sum_{i=-\infty}^{\infty} \sum_{j=-\infty}^{\infty} f(i,j) \ \sum_{i=-\infty}^{\infty} \sum_{j=-\infty}^{\infty} g(i,j)} \qquad\qquad 2.1$$

where (m, n) is the relative pixel displacement of the search region from the interrogation region while f(i, j) and g(i, j) are the pixel grey scale levels for the interrogation region and the search region, respectively. When applying the correlation function, the indices (i , j) are limited by the dimensions of the interrogation region and the search region. The cross-correlation function may be used with either 8-bit pixel grey scale values from 0 to 255 or with a pixel binary

scale, 0 or 1. The correlation results are normalized so that the correlation itself may be tested for validity (correlation peak validity is discussed further in section 2.4.4).

An example of the resulting spatial cross-correlation function and peak for consecutive image frame data is given in Figure 2.7(b) for comparison to the equivalent single frame autocorrelation function in Figure 2.7(a). Notice that the consecutive image frame correlation function has only one signal peak which can have a maximum theoretical value of 1; generally the value is less than one due to background noise, particles entering and leaving the image plane between exposures and images existing on the edges of the interrogation and search regions. Any smaller peaks are due to individual particle images matching up with other particle images. The position of the single peak, in Figure 2.7(b), with respect to the center of the correlation function denotes the end point and beginning point, respectively, of the most frequently occurring particle image displacement vector within the interrogation pixel space. Note that the direction of the vector is fully defined with no ambiguity.

There is no zeroeth order peak in the cross-correlation because images on separate image frames never correlate with themselves, unless the velocity is zero and no image shift is used. Furthermore, the number of background peaks is approximately half the number which exist for the autocorrelation technique. This is because only pixels from separate image frames may contribute to the correlation process, thereby reducing the potential for arbitrary pixel pairings, reducing overall background noise. Keane and Adrian (1991) give a detailed theoretical review of the consecutive image frame spatial cross-correlation and make some comparisons with the 2-D FFT autocorrelation method. They show that the consecutive image cross-correlation provides an approximate two-times increase in the signal-to-noise ratio measured by the ratio between the magnitude of the largest nonzeroeth order correlation peak and the average background level.

The spatial cross-correlation computed over a multiple exposure, single image

frame represents a correlation function of the image with itself as a function of displacement and is, therefore, an autocorrelation. The range of displacements for which this correlation is computed defines the search region used to locate the correlation peak. Dependent upon the placement and size of the search region, the autocorrelation function can have either 1 signal peak or 3 signal peaks. When the interrogation and search regions have the same center pixel position (Dong et al. (1992)), 3 signal peaks exist with the resulting autocorrelation function described by Figure 2.7(a). In the example given by Dong et al. (1992), the search region effectively encompasses the interrogation region. A zeroeth order autocorrelation peak exists as do 2 signal peaks symmetrically positioned about the zeroeth order peak, analogous to the 2-D FFT derived autocorrelation function. Except for an existing zeroeth order peak, the maximum theoretical correlation value for double exposure, single frame image data is 0.5 since half of the pixels are presumed from the first exposure and the other half of the pixels from the second exposure. The average image displacement vector is generally measured as the distance between the signal peak in the direction of image shift and the zeroeth order peak. This selection of signal peaks allows for easy subtraction of the superimposed image shift vector.

If the search region is defined such that the interrogation region and search regions do not significantly overlap (Sridhar et al. (1991)), then one signal peak will exist and the autocorrelation function is analogous to the cross-correlation function shown in Figure 2.7(b). In this case, the position of the single peak in the search region relative to the specified origin of the displacement space of the search region defines of the most frequently occurring particle image displacement vector. Any image shift vector can be simply subtracted off.

In the cross-correlation techniques described above, all pixels within the interrogation windows are utilized to construct the correlation function itself. It is possible to reduce the number of numerical operations using a cross-correlation

method if only the exposed pixels which represent particle images are used for the correlation process. Furthermore, specific boundaries of the area of interest need not be rigidly defined. This physical and computational characteristic can be used advantageously in reducing errors associated with large particle displacements and with increasing the effective particle image density per interrogation spot when compared to conventional 2-D FFT derived autocorrelation techniques or Young's fringe techniques. Such an algorithm, based on double exposed single frame image data, called an extended search region cross-correlation is detailed in chapter 3 and is incorporated in the present study. There are a number of limitations and errors which must be accounted for when using any of the above mentioned PIV analysis techniques. These are described in the following sections.

2.4   Errors and Limitations Associated with PIV

2.4.1   Introduction

Adrian (1988), Keane and Adrian (1990), Adrian (1991), Willert and Gharib (1991), and Huang, Fiedler and Wang (1993), among others, discuss major limitations and sources of errors for a generalized PIV system. With associated errors minimized, using the most recent levels of development in existing hardware and software matched to the proper application, PIV can determine velocities to an accuracy of 1%, but errors can be as high as 10% (Buchhave (1992)). This section is a general overview of errors associated with a typical PIV system and their observed effects. Keane and Adrian (1990) have asserted that errors associated with PIV are legitimately and conditionally associated with other multi-point measurement techniques, e.g., Laser Speckle Velocimetry.

The overview will provide a better understanding of the limitations of PIV, thereby allowing a better understanding of the data presented in chapter 5 and of PIV velocity data in general. Many of the errors are related and can be minimized using similar methods during PIV data and image processing. However, for generality, errors are placed in two categories; those originating from the image acquisition process, and those from the image interrogation process. A more detailed characterization of each type of error may be found in the above references.

2.4.2   Image Acquisition Errors

A basic assumption in PIV or any similar velocimetry technique is that the seed particles accurately follow the flow field down to the relevant flow scales. If the particles are small and nearly neutrally buoyant within the desired flow medium, this is a good assumption (Merzkirch (1987)). Specific experimental parameters to achieve particle-flow tracking fidelity are described in section 3.2.1. If seed particles are dense relative to the carrier fluid, the particle inertia will overcome drag forces created by the surrounding fluid and, if less dense, buoyancy forces may offset the acting fluid forces. The particle seed should match the specific gravity of the fluid medium as closely as possible and have a diameter as small as possible. This will minimize the inertial lag effects (Agui and Jemenez (1987)), gradient lifting effects (Rubinow and Keller (1961)) and buoyancy forces acting on the particle.

Another basic assumption is that particles move in only a slightly curvilinear fashion (Agui and Jemenez (1987)). Since particle displacements are assumed to be along straight paths in the time separation between exposures, any undetected curvature represents a potential error in the determined displacement that decreases in proportion to the average radius of curvature. Hence, the distance between particle

images should be small to avoid these effects. For multiple-exposure, single frame image data, if the distance between particle images is too small, the correlation peak from the displacement will begin to merge with the zero separation self-correlation peak, rendering the displacement peak unobtainable. If, however, all the relevant scales in the flow are obtainable with a given system, the assumption of linear particle motion is a good one.

Along with low particle density relative to the volume of the flow facility, one of the largest sources of error in PIV and similar methods is the loss of seeding particle images between successive exposures within the field of view. This error may effect all aspects of PIV since the technique is dependent upon properly determining displacements of the seeding images within the recorded flow field. Reasons for particle losses, or in the extreme case of particle field "sparseness", are large out-of-plane particle displacements, large in-plane particle displacements and possible illumination light attenuation producing a shadowing affect on various regions of the flow field. All of these errors except for the light attenuation effect can be minimized using the seven dimensionless parameters of Keane and Adrian (1990); these parameters are described in detail in section 2.4.4. Large out-of-plane displacements can be reduced if the time separation between light pulses is kept small enough or if the light sheet is thickened. Neither of these actions is necessarily desirable in all cases. In addition, as reported by Sinha (1988), out-of-plane motions in conjunction with a large field-of-view can cause over predictions of in-plane displacements due to optical parallax error. This error increases with increased light sheet thickness.

Large in-plane motions, relative to the interrogation region size, due to large velocities or a small interrogation region may cause one of the particles of a particle pair to overshoot the boundary of the specified interrogation region. Typically, the maximum particle displacement should be approximately 1/4 of the interrogation size

or less to minimize this affect. The maximum particle displacement does increase slightly over 1/4 of the interrogation size for an increase in the number of image pairs per interrogation region, N_i. Keeping the relative displacement appropriately small has been found to greatly reduce errors in determining correlation peak positions from the second particle exiting the interrogation region (Keane and Adrain (1990) and Grant (1993)). For example, if the particle displacements were 1/2 of the interrogation size, approximately 50% of the possible particles making up a pair would lie outside the interrogation region. This percentage of lost image pairs increases to 100% as the displacement increases to the interrogation region size. Both out-of-plane and in-plane motions leading to particle image pair loss may cause either extraneous displacement values or displacement vector dropout. The extended search region correlation method employed in the present study reduces the loss of image pairs due to in-plane motion taking the Ip_2 or second image out of the interrogation region as long as the length and time scales separating image pairs is not too large relative to flow structures.

Lourenco and Krothapalli (1987) recommend a particle density (N_i) of at least four particle pairs per interrogation region to extract a good statistical average. This represents the minimum particle density as determined for the Young's fringe interrogation method described in section 2.3.3.1. Keane and Adrian (1990) report this number is valid only for multi-pulse systems using more that two exposures and particle density should be at least 10 particle pairs per interrogation region to minimize unacceptable particle density fluctuations.

It is possible for particle density to be too large. If too much seeding is introduced into the flow field, the possibility arises of changing the single phase flow to a two-phase flow. Aside from this extreme case, image overlap predominates when seeding density is high and, if seeding is high enough, speckle patterns begin to appear, transitioning PIV to LSV. Guezennec and Kiritsis (1990) have shown that

although more particles per interrogation region improves velocity accuracy, more spurious particle matchings occur overall due to the overlap of particles when determining image displacements using a standard cross-correlation algorithm for PIV. They also state this problem increases when the particle images are larger.

Results from Prasad (1992) suggest these findings to be true. They define a "mean bias" error which arises from inadequate pixel resolution as well as from the algorithm used in finding the centroid of the correlation peak. Also defined is a "random" error which depends on the interrogation technique, the correlation peak location method, irregular image shapes, film grain and electronic noise incurred during image acquisition. Mean bias error is related to the velocity accuracy and was found to significantly increase for values of the ratio of the mean particle image size to the average space between particle pairs of less than 4. However, Prasad also found that the random error begins to significantly increase when the size to spacing ratio exceeds a value of 4 and accuracy decreases. This implies some optimum value of mean particle image size to spacing exists, as suggested by Guezennec and Kiritsis. Prasad found a value of four or slightly higher to be optimal and this is used during the present study.

Distortion of particle images due to particle reflective or transmittive inhomogeneities causing particle image blooming and eccentricity increases the difficulty in determining particle and hence correlation peak centroids. This problem is more pronounced with a larger image diameter relative to image pair spacing. If blooming occurs, errors are introduced in finding the edges of a particle relative to the background, thereby smearing the correlation peak and/or reducing its magnitude.

Moreover, particle images may be distorted due to imperfections in the transparent media through which the imaging optics record particle images. Errors may also be introduced by material curvature through which imaging optics must record through shallow angles near a small radius of curvature. This is the case near

the walls of curved transparent pipes. Also, contact points between two pieces of glass or acrylic may cause internal reflections near the boundary, distorting parts of the field of view and decreasing illumination intensity. Additionally, if the indices of refraction of the fluid media and the walls of the test boundaries are different, distortions in the images and relative distances between image pairs may be recorded incorrectly. This is especially true if images are recorded at large angles relative to the test boundary normal. These errors may be compensated for if the dimensions and distances of the test boundaries are known relative to the flow field of view. Procedures to minimize errors related to image quality for the present experimental setup are qualitatively and quantitatively addressed in chapter 3.

2.4.3   Image Interrogation Errors

Errors associated with the interrogation process are often functions of interrogation region size, the search region size and the spatial resolution. If the interrogation region size is too small for the available particle density, extraneous displacement vectors often result because the number of particle pairs is inadequate to determine the correlation peak. For example, if only two particle image pairs exist within the interrogation region, the cross-correlation between the 4 particle images gives a peak for the correct velocity. However, another correlation peak of equivalent magnitude also exists and two other large peaks are possible. No one peak stands out and hence the chance of obtaining an extraneous peak is high. This can be corrected by increasing the size of the interrogation region, decreasing the size of the search region, when applicable, or increasing the seeding density. The extended search region used for the present study is in general able to minimize extraneous peak detection such as these for a given interrogation region size when combined with peak

thresholding and variable search region sizes, see section 3.4.3.

Increasing the interrogation region size may bias velocity values. A "gradient bias" is defined by Keane and Adrian (1990) where the interrogation region is large relative to areas over which strong velocity gradients act. This gradient smears the correlation peak. The higher velocities are spatially averaged with the lower velocities, thereby causing the individual correlation values to be distributed over some area instead of summing to one narrow peak during the correlation process. The end result is a biasing of the velocity value towards the smaller velocities because larger numbers of image pairs are lost due to in-plane motion at higher velocity, on average. Keane and Adrian (1990) describe a nondimensional gradient bias parameter and velocity gradient parameters used to minimize effects due to gradient bias, see section 2.4.4.

Keane and Adrian (1990) also define a "detection bias" which is closely related to the gradient bias and is also caused by a large interrogation region. Because the velocity gradient affects the summing process of the individual correlation values by spatially distributing them, and because the correlation peak magnitude is dependent upon the number of correlation values which correspond to the displacement value, the correlation peak magnitude is reduced. Correct peak determination is therefore more difficult. If the interrogation region size is reduced, improving spatial resolution, the gradient effects are also reduced. An increase in the image density facilitates reductions in biasing of the velocity field by enabling the use of smaller interrogation regions and higher spatial resolutions.

Errors in detecting particles images against background illumination may also occur. In some cases, particle images are readily discernible from the background. In many cases however, there is a need to manipulate the image field to produce improved images relative to the background of the recorded field of view. Guezennec and Kiritsis (1990) found the inability to distinguish particle images from the

background was a main source of velocity error. They show as the contrast between what is an actual particle image and what is background noise decreases, velocity errors significantly increase. Pixel values corresponding to background noise, which are uncorrelated with other pixel values, extraneously add to the displacement correlation. Of particular importance is the need for uniform background illumination. Variations in background illumination cause difficulty in increasing contrast between background pixels relative to particle image pixels for all but the most customized image processing algorithms.

2.4.4   Optimization of Double Pulsed PIV

Most errors effecting PIV results are related to aspects of particle seeding and particle motions. Two of the major sources of error are insufficient particle concentrations and loss of particle images from the interrogation region. The loss of particle images from the interrogation region occurs when image displacements between times t_1 and t_2 are approximately the order of the interrogation region size in any of its three dimensions. It is therefore important to properly determine acquisition and interrogation parameters to optimize measurement accuracy and robustness by minimizing these and the other above mentioned error sources. This section briefly describes parameters, accepted throughout the literature, for optimizing velocity measurements for a given PIV system.

Keane and Adrian (1990) detail a procedure for quantifying a series of seven dimensionless optimization parameters and give their experimentally determined values for autocorrelation based double-pulsed PIV results. All relate characteristics of the particle image field to a few characteristic statistical interrogation parameters. These results were determined for an autocorrelation interrogation technique, but are

valid for spatial cross correlation techniques as well. The dimensionless parameters and recommended values are as follows:

1) The number of particle image pairs, N_i. For a circular interrogation region this is $N_i = \dfrac{C\pi d_I^2}{4M^2} \cdot \Delta z_o \geq 15$ where M is optical magnification

2) The nondimensional out-of-plane displacement, $\dfrac{w \cdot \Delta t}{\Delta z_o} \leq 0.25$

3) The ratio of the average particle image size to the interrogation region size, $\dfrac{d_\tau}{d_I} \approx 0.05$

4) The nondimensional gradient bias parameter, $\dfrac{M \cdot \Delta u \cdot \Delta t}{d_I} \leq 0.05$, where $\Delta u = \left(\dfrac{\partial u}{\partial y}\right)_{x_I} \cdot \dfrac{d_I}{2M}$

5) The ratio of maximum particle image displacement to interrogation region size, $\dfrac{M \cdot \Delta x}{d_I} \leq 0.25$

6) The nondimensional velocity gradient, $\dfrac{\Delta u}{u_I} \leq 4 \cdot \dfrac{d_\tau}{d_I}$

7) Detectability, D_o, of correlation peak, $D_o = 1.2 - 1.5$,

where C is the particle number density, w is the out-of-plane velocity, Δt is the time separation between light sheet pulses, d_τ is the average particle image diameter, u_I the local mean velocity, Δu is the maximum variation in u across d_I and x_I a marker representing the ith interrogation region. The nondimensional particle pair concentration value was determined experimentally and has a direct effect upon the ability of statistical interrogation procedures to discern valid velocity information. Nondimensional out of plane motion is the measure of how "thick" the light sheet should be to account for the three-dimensionality in the flow field before loss of particles, or loss of pairs as denoted by Keane and Adrian (1990), becomes a major source of error. The square of the ratio d_τ / d_I is of the order of the error in the measured particle displacements due to the correlation arithmetic process and should be kept below order 0.1. Gradient bias is a linear function of the maximum gradient

within an interrogation region nondimensionalized by the interrogation region size and time between exposures. It is a measure of correlation peak smear, described above in section 2.4.3, and hence a measure of the error in the measured particle displacements due to gradient bias. Related to the gradient bias parameter is the nondimensional velocity gradient which is an estimate of the maximum velocity difference across the interrogation region which can exist within a given interrogation region size and yield a better than 92% chance of detecting a valid velocity vector. In conjunction with the nondimensional gradient is the need to maintain the ratio of particle image displacements below 25% of the interrogation size. Finally, the detectability is the ratio of the highest correlation peak, which is not a self-correlation peak, to the next highest peak and is a measure of signal-to-noise of the correlation process.

A signal-to-noise ratio is used to determine if the correlation peak is a good displacement peak or a noise peak. Noise peaks may be detected falsely if the true displacement peak is only slightly larger than the background noise. Keane and Adrian (1990) also describe two other methods to discern good correlation peaks over noise peaks: First, confine the search for the displacement peak to only the region were the peak is expected to be. Second, define some threshold value which the peak magnitude must be greater than to be considered valid. The threshold value is used to delineate background noise from valid signal peaks. Except for detectability, the above nondimensional parameters and correlation peak validation techniques are used in the present study for optimizing PIV velocity data. Comparisons are made later in this manuscript between the above parameter values and the values used in the present study.

2.4.5   Post-Processing Error Detection

Though correlation peak validation is used during the interrogation process to minimize measurement errors, there are also procedures which search for "bad" vector estimates during the post-processing stage. These procedures do not guarantee good velocity measurements since vector validations are determined through relative comparisons of magnitudes. In general, these procedures find velocity vectors which are grossly different from neighboring values.

Landreth and Adrian (1989) examine the 8 neighboring velocity vectors to validate the results. If large disparities in magnitudes are found, the vector in error is replaced with an average of the surrounding vectors. They also mention using the next highest correlation peak in conjunction with the comparison process in order to find the correct vector if the first vector is erroneous. The new velocity vector is checked against the surrounding values to determine its validity. This process may be carried on to as many correlation peaks as the user desires to save per velocity location and to as many peaks as are definable.

Interactive validation procedures are also described by Willert and Gharib (1991). Willert and Gharib step through 3 x 3 groups of vectors and interactively determined whether the center vector is valid in light of its surrounding velocity vector values. Like Landreth and Adrian, they replace the vector in error with an average of the surrounding vectors. The entire velocity field is then processed, or more precisely convoluted in 2 dimensions (speed and direction), with the average of the 3 x 3 kernel used to replace the middle value. This has the effect of removing the high frequency noise associated with the varying location calculations of the correlation peak, so that Willert and Gharib describe it as a low pass filter.

An approach used by Chakrabarti (1992) is to use both the local average and a defined local standard deviation (LSD), in the u and v components of velocity, of the

surrounding 3 x 3 vectors to "provide a criterion for a tolerable level of inconsistency." The local standard deviation is multiplied by a standard deviation factor which allows for flexibility in the invalid vector criterion selection process. The average and LSD criterion sort the selected vectors according to severity of deviation from defined standards. In order of sorting, each vector is replaced by an average of the surrounding vectors. The "worst" vectors are corrected first, which minimizes any contamination of the other vectors.

For any of the above techniques, if several of the surrounding vectors are invalid, then the methods revert to an interactive inspection of the velocity field. The definition of a new "valid" vector becomes increasingly arbitrary. Post-processing methods may be useful with the PIV system described in this work, but have not been implemented. The results given in chapter 5 are presented as determined directly by the correlation analysis.

2.5   The DBS-PIV System

The DBS-PIV method used in the present study was developed in an attempt to construct a working PIV system using existing components within the Laboratory. A rotating mirror was utilized rather than a multi-faceted scanning mirror like that of Kawahashi and Hasoi (1991) described in section 2.2.1. Using a rotating mirror not only allows two beams to be used in parallel, but also permits much lower rotation rates than allowed with oscillating or multi-faceted mirrors. A rotating mirror scheme also produces no returning secondary images (Rockwell et al. (1993)). Because parallel beams may be used, the number of corrections made on the measured velocity field due to the angular motion of the beams is less. Particle images were recorded on photographic film using a 6 x 7 cm format camera.

After the particle images were digitized and processed to increase particle image to background contrast, a cross-correlation method employing the extended search region algorithm is used to interrogate the particle image field for the autocorrelation function describing the average image displacements. The algorithm uses only binary pixel values of 1 within the interrogation region to correlate with pixel values within the search regions to increase processing speed. The use of grey level values however could be easily implemented. Using an extended search region algorithm, which allows the search region to exist outside of the interrogation region, increases the effective particle concentration and significantly reduces the loss-of-pairs effect due to in-plane motion relative to traditional cross-correlation and autocorrelation techniques employed throughout the literature. The present DBS-PIV system along with the extended search region algorithm are fully described in the next chapter.

Chapter 3
THE DBS-PIV SYSTEM

3.1 Introduction

This chapter presents details of the present DBS-PIV system. The chapter is divided into three major sections, particle image acquisition, determining and optimizing the effective time between beam sweeps, and errors associated with the present DBS-PIV system. First, the image acquisition system is defined and illustrated. Then the optimization parameters introduced in section 2.4.4 are considered as applied to the present study. Finally, aspects of the errors and limitations of PIV as presented in Chapter 2 are further examined with respect to the present DBS-PIV system.

Within each section, the role of the PIV optimization parameters, presented in section 2.4.4, with respect to the present PIV system are discussed along with other considerations for optimizing the present PIV results.

3.2 The Image Acquisition System

3.2.1 Schematic of the Image Acquisition Hardware

Shown in Figure 3.1 is the PIV image acquisition hardware. The light source consisted of two parallel laser beams directed into the glycerin tunnel test section by a rotating mirror with the rotation plane lying on and parallel with the streamwise axis as shown in Figure 3.2. Images of illuminated particles were recorded with a

Image Shift
Rotating
Mirror

Camera

Acrylic Test
Section Box

Flow Direction

Beam
Direction

Laser

Laser

Mirrors

L_B

Laser
Beams

Motor
Control

ω

Mirror
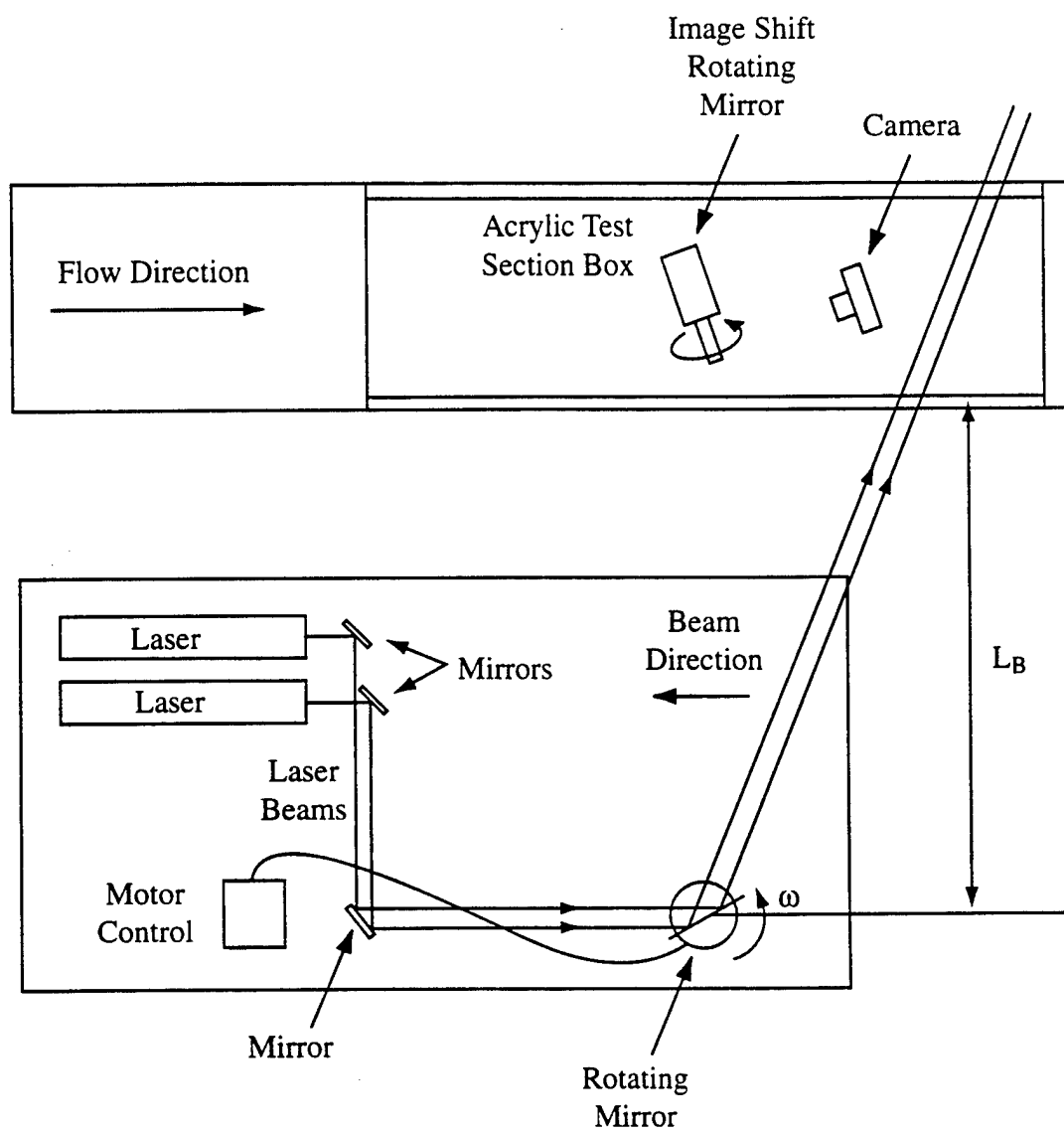
Rotating
Mirror

Figure 3.1 Image acquisition set-up
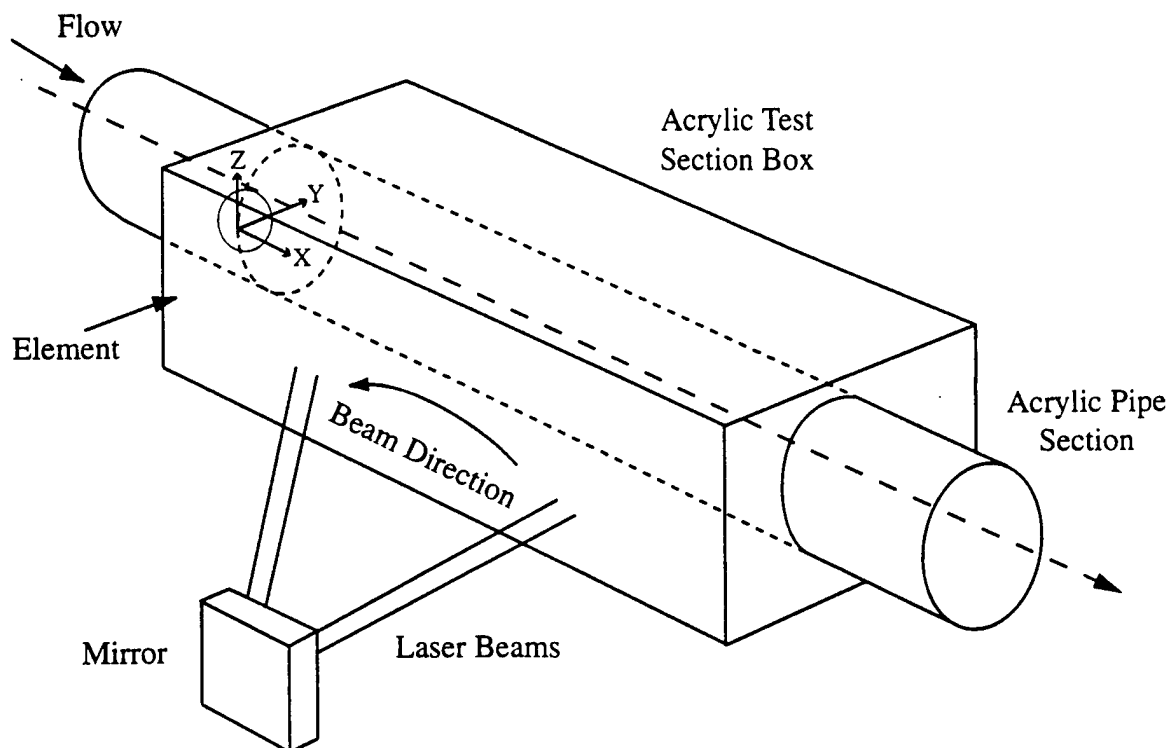
Figure 3.2 Orientation of rotating laser beams through test section

medium format camera. A second rotating mirror directed light into the camera and was used for image shifting. Both the camera and the rotating image shift mirror were positioned on top of the test section of the flow facility directly above the plane of the rotating parallel laser beams. The direction of rotation of the laser beams is counter-clockwise as viewed in Figure 3.1 while the rotation of the image shift mirror is counter-clockwise as viewed from the figure caption. Both the camera and image shifting equipment as well as the laser table were traversable in three-dimensions for access to any part of the test section. The motor controllers of the dual beam rotating mirror assembly and the image shifting mirror assembly were linked electronically to synchronize the particle illumination and recording process. The camera was operated manually.

3.2.2 Light Source and Associated Optics

Two continuous five watt Spectra-Physics argon-ion lasers were used to produce the dual laser beams. Pulsed light sources such as solid state Nd:YAG lasers or ruby lasers were not available. Both argon lasers were operated in the multi-line mode, one having an estimated beam diameter of 1.23 mm and the other 1.49 mm, measured to an approximate e^{-2} intensity level. The beam diameters and spacing were estimated using the voltage output of a small aperture, light sensitive meter connected to a micrometer traversing stage.

An approximate 14.0 mm beam spacing, d_B, between the two parallel argon-ion laser beams was used to optimize the balance between errors, spatial resolution and illumination intensity. Larger beam separations reduce the relative error associated with locating the centroids of particle images with respect to particle image separations, as described in section 2.4.2, because the uncertainty in centroid location

is small relative to the overall displacement between successive images. The mirror rotation rate must be increased however to maintain the same time between beam passages. This decreases the amount of light energy per particle because the beam is incident on a particle for a smaller time.

The size of the rotating mirror used to sweep the laser beams is limited by the need to minimize the rotational moment of inertia to maintain synchronization with other rotating hardware. However, the mirror size must allow acceptably large spacing between the laser beams. The rotational speed, ω, was 10 rps. An M106-178 Compumotor rotating stepper motor was used to rotate the mirror at a constant rate, ω, for a given image. The mirror used is 5.08 cm in diameter with a flatness of $1/5\lambda$ wavelength. The mirror rotational axis is positioned at $L_B = 1.523$ m from the inside wall of the test section, see Figure 3.1. The rotating beam velocity located at the inside wall of the test section is given by $V_B = 2\omega L_B$ at the location where the beams are normal to the test section wall. Corrections to this beam sweep velocity are needed at locations inside the test section due to changing beam length and index of refraction changes.

The beam sweep velocity for a mirror rotational velocity of 10 revolutions per second is 193.1 m/sec at $y^+ = 30$. When compared to the largest flow velocity expected at this location, 8.3 m/sec for the mean velocity plus the largest expected positive velocity fluctuation, the beam sweep velocity to maximum fluid velocity ratio is approximately 23:1. Due to the large relative velocity of the sweeping laser beams with respect to the flow field velocity, the beam sweeping motion approximates an instantaneous light sheet as seen from the camera. This is a good assumption if the time for the laser beams to sweep the field of view of one picture frame is less than the smallest time scales characteristic of the flow field, in this case the Kolmogorov temporal microscale. It takes approximately 0.892 msec for the beams to sweep across the 17.07 cm field of view representative of the field-of-view

of one picture frame. For the given flow parameters, the Kolmogorov temporal microscale is $\tau \approx 3.5$ msec, approximately four times greater than the time for the beams to cross the field-of-view. Hence, the assumption of an instantaneous light sheet is a good approximation.

3.2.3   Particle Seeding

The tunnel was seeded with 8-12 μm hollow glass balloons. The glass balloons have a specific gravity, sg = 1.1, which is close to the specific gravity of the glycerin, sg = 1.232. This helps ensure that recorded flow path errors due to inertial effects are minimized when combined with the small size of the particles. As a check, an approximation for the slip velocity over the flow velocity, $\Delta u_s/u_f$, between a sphere in a fluid medium as given by Agui and Jimenez (1987) and the time constant, $\tau_{p,}$ for a spherical particle in a fluid medium to respond to the drag force exerted on it by the surrounding fluid found in Taylor (1992) were determined for the present flow conditions and particle characteristics. Both the slip velocity and delay time are given as follows:

$$\left(\frac{\Delta u_s}{u_f} \right)^2 \approx \left(\frac{\Delta \rho}{\rho} \right)^2 \frac{d_p^2 \cdot f}{10 v} \qquad\qquad 3.1$$

$$\tau_p \approx \frac{d_p^2}{18 v} \left(\frac{\rho_p}{\rho} \right) + \frac{d_p^2}{36 v} \qquad\qquad 3.2$$

where $\Delta \rho$ is the density difference between particle (ρ_p) and fluid (ρ), f the characteristic viscous frequency of the flow field and d_p the average particle diameter.

These equations are valid if the flow around the particle, based upon the relative slip velocity, is Stoke's flow (i.e., Re $\leq$ 1). Since the highest flow turbulence intensity levels exist near the Gaussian protrusion, introduced in chapter 1 and discussed in detail in chapter 5, the flow field near the protrusion is used as a worst case scenario to analyze possible particle to flow path differences. Using $\Delta u_s = 0.00389$ m/s, found using the equation for slip velocity above with the flow characteristics found at the height of the Gaussian protrusion at approximately $y^+ = 16.5$, the Reynolds number is Re ≈ 0.0011, which is much less than one. The slip velocity of the particle is roughly 0.08% of the fluid axial velocity at the top of the Gaussian protrusion. The ratio of delay time (τ_p) for the particle to react to fluid accelerations over the Kolmogorov time scale is of the order 10^{-5}.

Particle images are larger than the particles themselves when compared in real space due to lens aberrations as well as finite film grain size and a number of other possible effects. The resulting particle image to interrogation region ratio $d_r/d_I \approx$ 0.062, is very close to Keane and Adrian's (1990) suggested ratio of 0.05. Good particle images were recorded near the test section wall, but farther from the wall, the light sheet is attenuated by the glass balloons, air bubbles and other particulate preexisting in the glycerin. This attenuation reduced the image quality away from the wall. The maximum size of any air bubbles is smaller than 50 μm as determined by Chevrin (1988). Although larger than the glass balloons, very few bubbles were discernable, hence, they did not play a significant role in the image interrogation process.

Particle seeding densities were guided by practical experience with test images and from the findings of Keane and Adrian (1990) that indicate at least 10 particle pairs per interrogation region are required for good image correlation. Too many particles in the flow cause severe light attenuation as the beams penetrate into the flow field. This attenuation results in insufficient particle illumination away from the

test section wall. The number of particle pairs used in the present experiment, on average, is N_i = 15 - 20 within an image interrogation region size of 6.25^+ x 6.25^+ wall units.

3.2.4   Recording Optics and Photographic Parameters

3.2.4.1   Image Shifting

A rotating mirror was placed between the object plane in the test section and the image plane in the camera to project a false object displacement in a predetermined direction to the image plane. This eliminates the 180° directional ambiguity associated with the particle image pairs in the image plane. Image shifting also decreases the infinite dynamic range associated with the no-slip condition, at the test section wall, compared to the finite displacements away from the wall.

Particle images were recorded through a rotating mirror assembly positioned directly above the test section, reflecting the images at a 90° angle into the camera. A 10 x 10 cm mirror with $1/4\lambda$ flatness was rotated by a Compumotor M83-93 stepper motor. Mirror size was chosen to accommodate a large camera lens and to maximize the field-of-view in the object plane.

The rotating mirror assembly was positioned at a 15° angle to the streamwise flow direction. An offset angle of 15° was originally used to account for large negative velocity fluctuations in the y-direction, v-component of velocity, but later found unnecessary. Image shifting is needed in only one dimension, generally shifted in the preferred flow direction such as downstream in a pipe flow. The image shift in the x-direction was calculated so as to shift second exposure particle images with the highest negative velocity to the positive side of the first exposure particle images.

The flow field of interest had a small Gaussian shaped protrusion at the wall that created a separated flow with negative velocities. The largest negative u-velocity fluctuations are approximately 3 m/sec (Fountaine (1993)), corresponding to a displacement of 0.362 mm between beam sweeps. Landreth and Adrian (1988) give an expression for the image shift as $\Delta x = 2M\omega(s_o - s_m)\Delta t$. Here, M is the overall magnification of the image capturing and interrogation hardware, ω is the rotational velocity of the image shift mirror, s_o and s_m are the distances from the image plane to the object plane and the distance from the image shift mirror to the camera primary lens, respectively, and Δt is the calculated time between laser pulses/particle exposures. With the geometry of the configuration used for the image shifting in the present study and with an image shift mirror rotation velocity of 1 rps, the resulting image shift displacements were approximately 0.371 mm in x and 0.097 mm in y. Image shift values are not uniform over the entire field-of-view, varying up to 3% and 17%, with respect to largest average displacement, in the x and y-components, respectively, due to curvature effects near the test section wall.

There are further considerations which need to be addressed when using an image shift device with dual beam sweep PIV; these considerations are a consequence of the PIV system itself and are discussed in detail in section 3.4.2.

3.2.4.2   Image Recording

Particle images were recorded using a Pentax 6x7 format SLR with a 135 mm focal length macro lens attached by a No# 1 Pentax extension tube. A macro lens is used to better approximate a flat field-of-focus, thereby decreasing errors due to focusing inaccuracies near the edges of the field-of-view. The camera lens magnification factor was 0.41, providing the desired working distance required by the

large format camera. A photographic film camera was used because it exists in medium formats and because it offers superior spatial resolution over standard digital video cameras. A medium format camera allowed for a practical working distance from the test section while granting a larger field-of-view than is available with smaller format cameras such as a 35 mm SLR. Kodak TMAX 400 film was used with the camera for its good resolution, approximately 100 lines per mm, its good sensitivity and its ease of processing. The lens aperture was set at f/8, three stops up from the fastest setting, corresponding to the experientially determined optimum balance between light intensity and image quality (e.g. sharpness). The camera shutter speed was set at 1/15 second.

The greatest obstacle in photographing through an image shifting mirror is system synchronization. As the dual laser beams pass over the region of interest in the flow field, the image shifting mirror must be in position to transmit illuminated particle images to the camera which must have an open shutter. Additionally, background light must be eliminated to increase contrast between particle images and the background. The latter is accomplished by enclosing the image acquisition hardware and glycerin tunnel test section within an opaque tent made of black plastic to keep out all light except that present from the lasers. System synchronization is accomplished by electronically connecting the laser beam rotation system with the image shift rotation system. First, the laser beam rotating mirror is positioned such that the beams are normal to the test section wall and placed at a known position within the flow field which is easily located later on the exposed film negative. The image shift mirror is then positioned at an approximate 45° angle to the test section such that the desired field-of-view within the flow field and the dual laser beams are observed through the camera view finder. The acceleration settings of both stepping motor drivers were set to the same values. The settings were kept low so rotational inertia differences between the mirrors did not affect the indicated acceleration

values. Synchronization is possible when the laser beam sweep mirror is rotating at some integer multiple of the image shift mirror rotational rate. Keeping the acceleration values for both mirrors equal preserves the phase match needed to ensure the mirrors repeatedly matched their initial locations simultaneously at the difference frequency between their rotation rates. Both acceleration and rotational velocity on the motor drivers are controllable to better than three decimal places and the accuracy of the rotational velocities are 0.02%. System reliability is easily accounted for by observing the synchronization of both mirrors through the camera view finder. The synchronization electronics start the compumotors at the same time with an electronic input pulse, initiated by a push of a button by the operator, thereby initializing the periodic phase relationship between the two mirrors.

Camera operation is controlled manually by the operator. With the image shift mirror rotating at 1 rps, the operator can see when to shutter the camera. Using the 1/15 of a second shutter speed allows enough time lapse to capture the synchronized illumination-image shift process every time without electronic assistance. The camera and image shift system are connected rigidly on a rail system to assure colinearity as this apparatus is traversed along the axis of the test section. Traversing is necessary to obtain particle images both upstream and downstream of the Gaussian protrusion in the range previously used in the glycerin tunnel (Fountaine (1993)).

The film was processed using the standard Kodak D-76 developer for black and white film, indicator stop bath, rapid fixer, permawash and rinse cycle. Standard fixing times were modified however to push the processing two f-stops. Greater image intensity is attained as well as a greater depth-of-field, without inducing greater lens aberrations associated with larger aperture openings, by increasing film sensitivity through modified film developing and by using a smaller aperature than would otherwise be needed. Pushing the film processing increases the effective film

sensitivity to ASA 1600. Depending on the processing, film grain structure can be better with pushed 400 ASA film over standard 1600 ASA film.

3.3   Image Digitization

The photographic double exposure particle images were digitized using the setup shown in Figure 3.3. Film negatives were placed in Klinger 2-D traversing stages for digitization of any region of the film negative. A diffuse, 75 W, white, back lighting source was used to illuminate the film negatives. A Questar QM1 long range microscope was coupled to a monochrome Cohu CCD camera at the opposite end of the optical tube bench which supports all of the apparatus. The CCD camera consists of a 512 x 480 array of square pixels. A Data Translation DT2862 frame grabber board was used to acquire and store the digitized images from the CCD camera. Images were acquired in an array of 512 columns by 480 rows with 8-bits per pixel intensity resolution resulting in grey level values ranging from 0 to 255.

Image acquisition begins with visually focusing the imaging system on the film negative at some desired initial position. It was useful to have preexisting markers within the photographic image to determine exact locations within the flow field once the interrogation process began. This is especially true when multiple images are taken to obtain data over larger regions than the field-of-view of the camera used to photograph the dual beam sweep particle images. Location markers were recorded on the film negatives by placing line markers, spaced 2.54 cm apart, on the outside of the test section wall. One marker is axially located at the position of the Gaussian protrusion. As the laser beams pass by, each marker leaves a very thin shadow within the flowfield which is easily discernable on the digitized image.

In order to quantify all translations in pixel space as particle translations in the

PIV (PARTICLE IMAGE VELOCIMETRY)
[IMAGE INTERROGATION]

Illumination
Source

Support Beam

Long-range
Microscope

CCD
Camera

2-D Traversing Stages

PC with Data
Translation
Frame Board

Klinger
2-D Stepper
Motor Controller
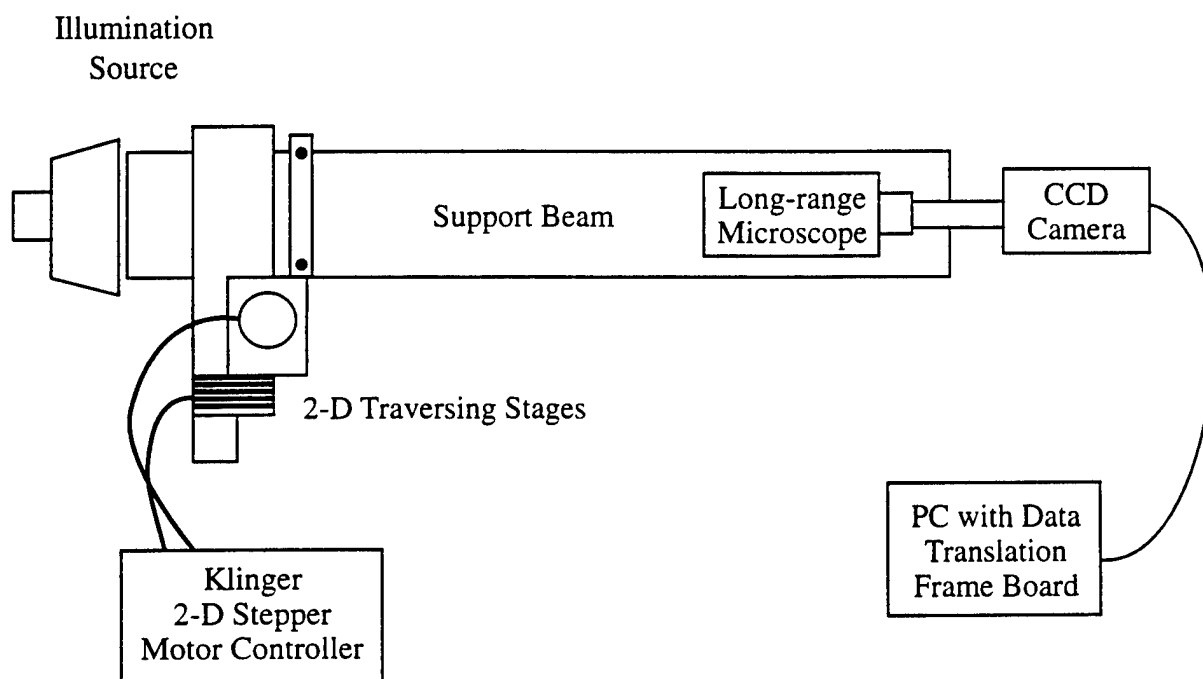
Computer uses a Data Translation Frame Grabber Board
and DT-IRIS Image Processing Software

Figure 3.3 Image interrogation set-up

flow field in real space, the total image magnification of the system must be determined. The total magnification is the combined magnification of the film camera and the long range microscope / CCD camera combination and equals 0.36. Of the 480 rows in pixel space, the protrusion is approximately 212 pixels in the vertical direction with the total magnification used. The protrusion height is approximately 0.764 cm and the dimension corresponding to a pixel is 36.0 μm in real space. From this information, pixel lengths are translated into Klinger translation stage equivalent lengths so, as the film negative is digitized piece by piece, each translation stage position readout gives the position within the flow field. All acquisition parameters, such as x and y translation increment sizes, pixel origin location in image space as well as the number and the spatial pattern of the digitized 512 x 480 pixel images to be acquired from a single film negative are inputs to the software used to control the digitization of the film images.

During film traversing and image digitization, positions were referenced to a local origin in the upper left hand corner of the image. The frame grabber board used for digitizing produced a vertically inverted image. Therefore, the x-direction or streamwise direction is positive to the right and the y-direction is positive downward. Each local origin within a digitized image frame was referenced to a global origin located at the center and base of the Gaussian protrusion.

For the extended search region algorithm used for the present study, a pixel buffer around the boundary of each 512 x 480 pixel image frame was allocated to facilitate the extended search region at the boundary of the single frame, double-pulsed image field. The amount of buffer allocated was based on an initial guess displacement, the specified size of the extended search region, the maximum expected velocities and the position in the flow field combined with the position in pixel space and the total magnification. The initial guess displacement is an estimate of what the image displacements are expected to be. Buffer sizes for this experiment were 8 and

32 pixels on the top and left boundaries, respectively, 128 pixels on the right boundary and 96 on the bottom boundary. As the location of the interrogation regions being considered were moved through pixel space, no new interrogations were conducted in either x or y unless the sum of step size, interrogation region size, initial guess displacement and search region size were contained within the remaining pixel space. The above dimensions assume a square or rectangular interrogation region and search region in pixel space. Buffer sizes were specified before image interrogation.

Because of the buffer regions, each 512 x 480 image frame must overlap the previous image frame digitized from the same film negative. Overlapping of consecutive image frames digitized from the same film negative allow for the interrogation of regions in the flow field which were missed in the previous image frame due to the combination of pixel boundaries, step sizes and/or large displacements. The objective is to maintain a constant grid interval for the interrogation region positions as they move from one image frame to another over the entire image field digitized from a film negative. The first position in the next image frame corresponds to the next step that would have been taken in the previous image frame if the previous image frame would have been larger, assuming all parameters equal. For the buffer sizes given above, image frames overlap approximately 27% and 20% respectively in x and y.

Each film negative was divided into small image frames, measuring 512 x 480 pixels, during digitization so as to increase magnification and spatial resolution. Approximately 12 regions were used to divide the film negative in the x direction, which are 18.45 x 17.30 mm in the actual flow field, and only one region in the y direction. Only one region is used in the y direction due to the strong light attenuation of the laser beams as they travel into the test section center, making it difficult to accurately measure particle image displacements at larger distances from

the wall. This restriction was acceptable because, as with Fontaine (1993), the region of interest was near the wall. Each image frame is separately interrogated for the displacement field and stored for post-processing. In order to reconstruct the displacement field of the entire film negative, the resulting 12 displacement files were merged into one working file referenced to the global flow field, for the present case relative to the center of the Gaussian protrusion. Sixty-five images were taken at each flow field position for averaging purposes. Sixty-five was chosen as a balance between velocity average accuracy and experiment time as well as film and development costs.

3.4   The Effective Time (Δt) Between Beam Sweeps

3.4.1   The Optimized Time Interval

Determining an appropriate time separation Δt between beam sweeps is dependent on the desired spatial resolution, which is established by the interrogation region size, out-of-plane velocity magnitudes and velocity gradients within any given interrogation region position within the flow field.

When determining Δt, the maximum allowable particle pair separation condition, $\frac{M \cdot \Delta x}{d_i} \leq 0.25$, is important as is the maximum out-of-plane displacement condition, $\frac{w \cdot \Delta t}{\Delta z_o} \leq 0.25$, which must be met for accurate velocity estimates. At $y^+ =$ 30 where the maximum velocities are expected, using a mirror rotation rate of 10 rps and a beam separation of approximately 14.0 mm, the maximum nondimensional particle pair separation is $\frac{M \cdot \Delta x}{d_i} \approx 0.29$. Though this value is slightly higher than Keane and Adrian's recommended value, the parameter is not as critical when using the extended search region algorithm as will be shown in section 3.3. Using data

from Fontaine (1993) for the out-of-plane velocity w at $y^+ = 30$ as well as the given

beam separation d_B and beam thickness Δz_o, $\dfrac{w \cdot \Delta t}{\Delta z_o} \approx 0.165$.

Both, $\dfrac{M \cdot \Delta u \cdot \Delta t}{d_I} \leq 0.05$, the optimal gradient bias limit, and the gradient

parameter given by Keane and Adrian (1990), $\dfrac{\Delta u}{u_I} \leq 4 \cdot \dfrac{d_\tau}{d_I}$ minimizing the

"detection bias" errors must also be met. For the present study, using velocity values

from Fontaine (1993) near $y^+ = 10$, the gradient bias value is approximately 0.029,

while the left hand term of the gradient parameter is 23% lower than the right hand

term.

3.4.2   Correcting the Time Interval

As a consequence of the relative motion of the sweeping beams with respect

to the fluid when using DBS-PIV, the time interval between the first and second

particle image exposures, Δt, is dependent upon the particle velocity. This effect can

be accounted for when computing the velocity. Also, corrections must be made to the

time interval used to compute the velocity because the time interval is a function of

rotating laser beam angular position relative to the test section. These corrections are

in-part due to the index of refraction change between the outside medium, air, and the

test medium, glycerin.

Figure 3.4 depicts the effects of particle motion on the time interval Δt. As

beam 1 and 2 sweep from right to left, a particle moves downstream. This particle is

assumed to move in a straight line at some angle θ relative to streamwise direction.

Beam 1 and then Δt later beam 2 sweep over the particle. It is easily seen that the

faster the particle is moving in the streamwise direction, the smaller Δt will be for that

particle compared to slower moving or nonmoving particles. Therefore, the time

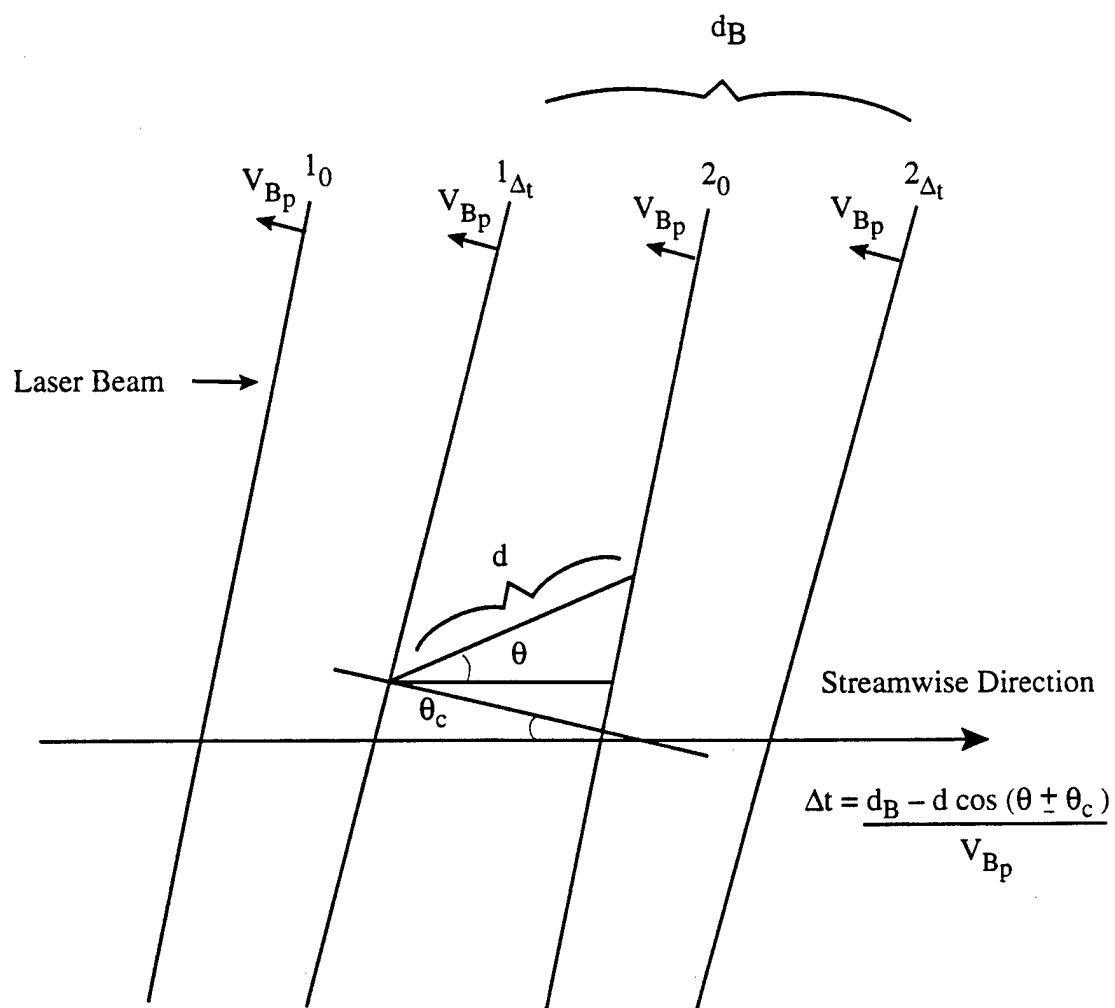interval between the passage of the first beam over a moving particle and the passage

Figure 3.4   Incidence angle of laser beams relative to particle velocity

of the second beam must be corrected as a function of velocity. The form of the time interval corrected for particle motion is

$$\Delta t = \frac{d_B \mp d \cdot \cos(\theta \pm \theta_c)}{V_B} \qquad 3.3$$

where, as shown in Figure 3.3, d is the line segment path of the particle between beam passages, $V_B = 2\omega R$ is the beam sweep velocity at the measurement point and θ_c is the angle between the sweeping beams and the streamwise flow direction. The beam incidence angle is zero at the predetermined origin and θ_c is added or subtracted in equation 3.3 depending on the location, relative to the origin, of the measurement point. The $d \cdot \cos(\theta \pm \theta_c)$ term is added or subtracted depending upon the direction of particle motion.

The image shift and any variations in the image shift, discussed in section 3.2.4.1, are accounted for by taking an ensemble average of calibration images with no flow velocity in the test section. Ensemble averaged image shift displacements, one *per* interrogation point, are estimated over the entire field-of-view and subtracted from the corresponding measured displacement, d . This is not entirely correct, however, since the image shift and the time between beam sweeps are both dependent upon individual particle velocities. A closed-form solution for determining Δt and the image shift Δx exists if equation 3.1 and the image shift equation introduced in section 3.2.4.1 are solved simultaneously. This, although, would not account for variations in image shift values for reasons such as strong test section wall curvature. Though the image shifts from the calibration file are not exactly correct, a correction, Δx_c, to the average image shift, Δx, exists in the form $\Delta x_c \approx \Delta x \left(\frac{\Delta t}{\Delta t_0}\right)$. Δt_0 is the time interval between the sweeping beams at zero fluid velocity and Δt is the time interval, calculated from equation 3.3, at the location of interest in the flow field. This correction is applied once the displacement, d, is estimated from the initial image shift

Δx and the initial Δt is calculated from equation 3.3. A corrected displacement is then found as a function of Δx$_c$ and consequently a corrected Δt is found. Applying one iteration produced a 2.7%, 2.6% and 2.9% change in the average streamwise component of velocity at y$^+$ positions of 30, 10 and 2.5, respectively. Applying a second iteration produces only a 0.057% change in the corrected streamwise velocity at y$^+$ = 30 and hence, is unnecessary. This correction, however, was not incorporated during this study; the effects of not using the correction on the velocity data taken during this study are discussed in section 5.2.

The time between beam passages at y$^+$ = 30 is Δt = 70.0 μsec using the mean velocity at this position. The resulting particle displacement is 0.420 mm in real space. A particle with no velocity at the wall would have a corresponding time between pulses of Δt = 72.8 μsec. Not correcting for the particle displacement term, d, when determining a corrected time interval causes an approximate 2.2% error in the mean velocity at y$^+$ = 30.

There are a number of further complicating factors which need to be accounted for with DBS-PIV which are not present when using a pulsed laser configuration. Because of the acrylic test section wall construction, depicted in Figure 3.5, small index of refraction differences between air, glycerin and acrylic require corrections to be made to the angle of the rotating beam paths relative to the particle paths as well as to the dual beam separation d$_B$ as functions of streamwise position. A large beam incidence angle is shown in Figure 3.5 for purposes of illustration. Furthermore, beam sweep velocities change with angle θ relative to the test section wall since the beam length L$_B$ changes with angle θ and this must be accounted for.

The complication arising from different refractive index values is simplified by using parallel beams rather than using converging beams to illuminate particles as done by Kawahashi and Hosoi (1991). Using Snell's Law, $n_1 \sin\theta_1 = n_2 \sin\theta_2$, where n_i
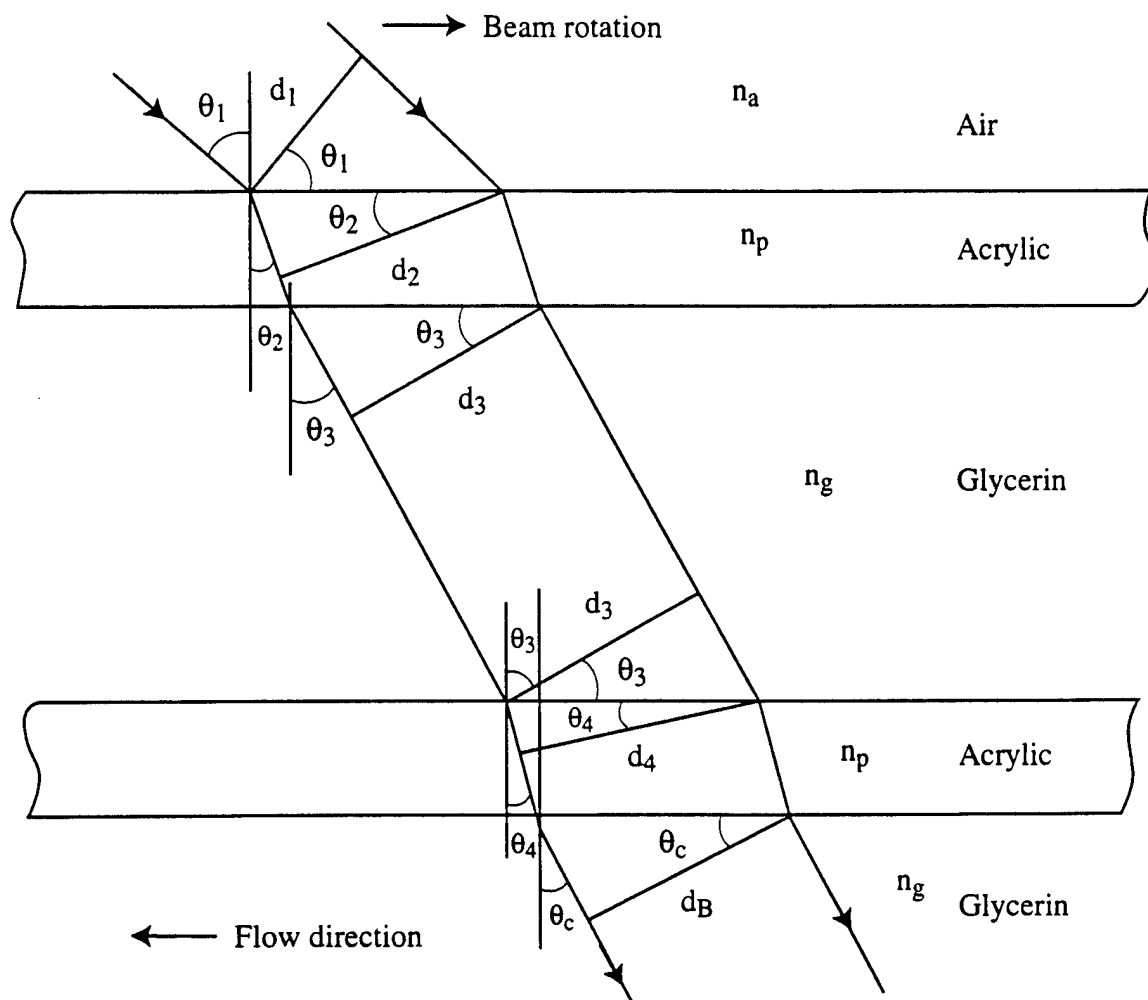
Figure 3.5 Laser beam refraction at the test section walls

is the index of refraction of the ith medium through which the laser beams must pass and θ_i the corresponding beam angle of incidence, it is found the beams remain parallel after passage through the test section wall. The beam separation distance, however, increases with increasing beam to test section incidence angle. The beam separation d_B is measured perpendicular to both beams. Letting θ_1 be the angle between the laser beams and the normal to the test section, the corrected angle of the laser beams, θ_c, and the corrected beam separation, d_c, after passing through both layers of plexiglas and glycerin are:

$$\theta_c = \arcsin(\frac{\sin[\ \theta\ ]}{1.465}) \qquad d_B = d_1 \cdot \frac{\cos\theta_c}{\cos\theta} \qquad\qquad 3.4$$

where $n_g = 1.465$ is the index of refraction of glycerin. For a beam incidence angle of around 8.5°, which is possible for positions in the flow which are far downstream relative to the rotating mirror, the mismatch in refractive index values between the acrylic and the glycerin produces an approximate 0.6% relative change in d_B.

The change in beam velocities as a function of distance from the test section wall is accounted for by using the distance from the point of interest in the flow field to the beam sweep mirror rotational axis. When the sweeping beams are normal to the testsection wall, an approximate error of 1% results for a determined mean velocity at $y^+ = 30$ if this distance is not changed from L_B. Conversely, not correcting for the change in incidence angle θ_c using the above equation as a function of streamwise position represents a relative error in Δt of less than one tenth of one percent. The correction for the change in θ_c was used, however, for completeness.

3.5   <u>DBS-PIV Specific Errors</u>

Dual Beam Sweep PIV has three possible error sources which are unique. First, if the ratio of laser beam diameter to beam separation distance becomes large, the duration of the particle exposure becomes a significant fraction of the time between exposures. This poor relative temporal resolution smears out the correlation peak leading to increased uncertainty in the estimated displacement. This is true independent of the correlation technique used (see section 2.3.3) to determine particle image displacements. If the laser beam diameter is large enough, particle images may become elliptical or streaked, further exaggerating the errors.

The laser beam diameter may be minimized by using a beam expander and collimating lens such that the position of the smallest diameter length of the beam, or beam waist, is designed to sweep through the image recording field-of-view. One way to minimize the ratio of beam diameter to beam separation is to use a large beam separation. This however may increase the effects of particle path curvature on displacement results as well as increase random errors discussed by Prasad (1992) if there are no other changes to the beam sweep system to maintain the same time between beam passages. This can be achieved by increasing the rotational velocity of the beam sweep mirror or by increasing the distance between the beam sweep mirror and the test section.

The second possible error source is a result of the finite amount of time required to sweep the beams across the field-of-view. Velocities determined upstream in the field-of-view are not temporally coincident with velocities downstream in the field-of-view. If the beam sweep speed is not high enough, the evolution of the flow field during the beam sweep period results in a distorted representation of the flow. This distortion may be compensated for by increasing beam sweep velocity and increasing the image shift mirror rotation rate. This error is

not significant unless estimating spatial correlations with no time lag is desired or accurately capturing large scale structures, relative to the field-of-view, is desired.

Finally, estimated velocity values are incorrectly increased or decreased since the time separation between beams passing over a particle is dependent upon the particle velocity relative to the beams. If a particle is moving toward the beams, the time separation is less than $\Delta t = d_B / V_B$ and if a particle is moving away from the beams, the time separation is greater than $\Delta t = d_B / V_B$. The correct velocities are determined using the procedure described in section 3.4.2.

Chapter 4

IMAGE ANALYSIS METHOD

4.1   Introduction

This chapter presents details of the present particle image analysis method. The chapter is divided into three major sections, particle image pre-processing, particle image interrogation and velocity field post-processing. First, the image processing technique used to prepare recorded particle image fields for velocity interrogation is illustrated and discussed. Next, aspects of the image interrogation procedure are described while the extended search region algorithm is detailed. Finally, the methods of computing velocity field statistics are presented.

Within each section, the role of the PIV optimization parameters, presented in section 2.4.4, with respect to the present PIV system are discussed along with other considerations for optimizing the present PIV results.

4.2   Image Pre-processing

Once digitized, the particle images required enhancement for good results. The illuminating laser beams are attenuated substantially in the flow as the beams penetrate into the test section and the attenuation dims the particle images with increasing distance from the wall. This is due to the light being scattered by the seed particles, glycerin contaminates and bubbles. The end result is reduced particle image contrast relative to the background. Other factors such as particle size and shape variability, focusing errors, film grain, diffraction limitations of the lens (Goodman (1968)) as well as intensity variations due to particles which are on the edge of the

sweeping beams, therefore unevenly illuminated, also tend to reduce particle image contrast with the background. Consequently, the potential for extraneous vectors is increased by these factors degrading the image quality. The effect of the image quality on the correlation computed by the extended search or related methods is a reduced correlation peak level relative to the background noise in the correlation. Image processing methods can improve the images and reduce the number of extraneous bad vectors.

Because particle illumination decreased nonuniformly with increasing distance from the test section wall, the use of any one image processing operation or any sequence of operations which acted globally to produce uniform images across the entire field-of-view, was not possible. Therefore, the field-of-view was broken into three areas, called regions of interest or ROI's, which are independently processed. Figure 4.1(a) shows an original image, considered a worst case scenario image, digitized from a film negative. The right edge of the image is approximately 15 mm upstream of the protrusion with the shadow on the left hand side created by the Gaussian protrusion. Large variations in image and background light intensities exist within the image. Image blooming, the bleeding of one image into another or the background, is apparent.

The image processing began with a closing operation using a 3 x 3 kernel on the entire image. Closing is a morphological operation of a grey scale dilation and erosion, in that order (Gonzales and Woods (1992)). The results are shown in Figure 4.1(b). The effect is to increase the size of the inner, brighter region of a particle, thereby increasing the discreetness of each particle image relative to the background. Contrast is somewhat decreased. The next step starts with the region of interest closest to the test section wall where particle images are brightest. Within the ROI, the output lookup table (LUT), which is the transfer function defining the relationship between original frozen pixel values and modified pixel values, is modified from a
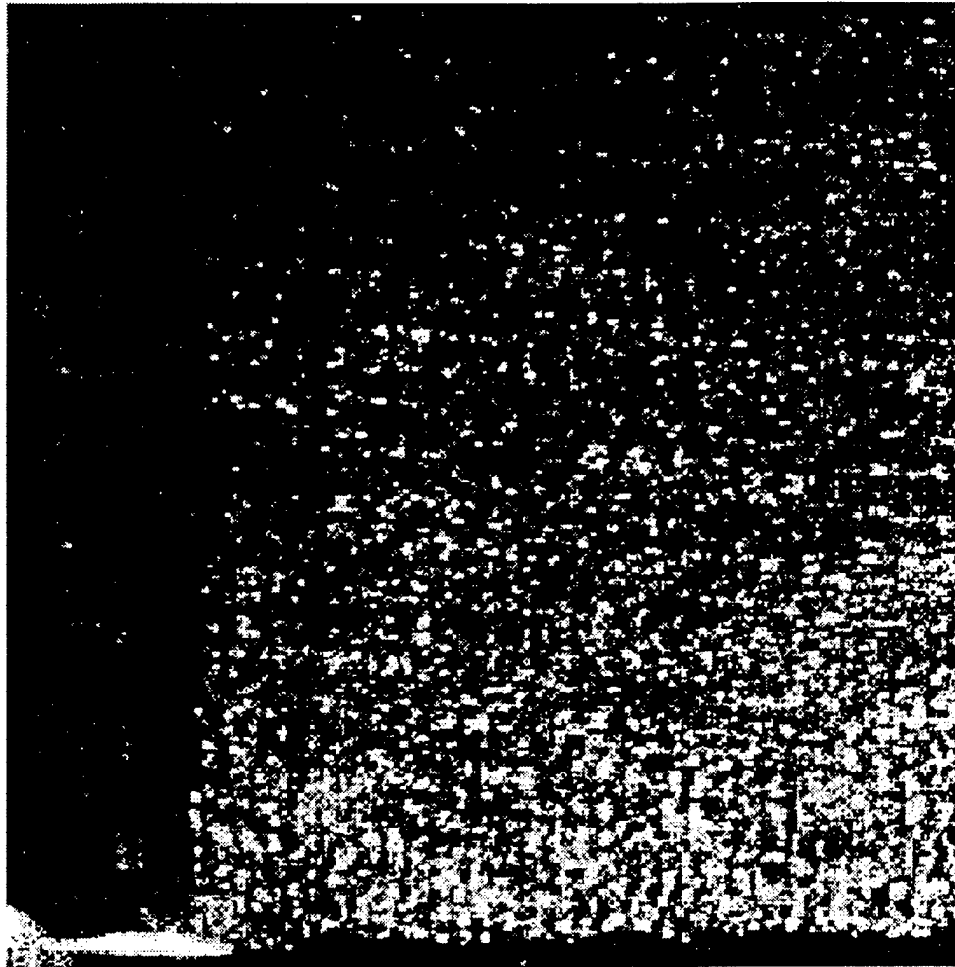
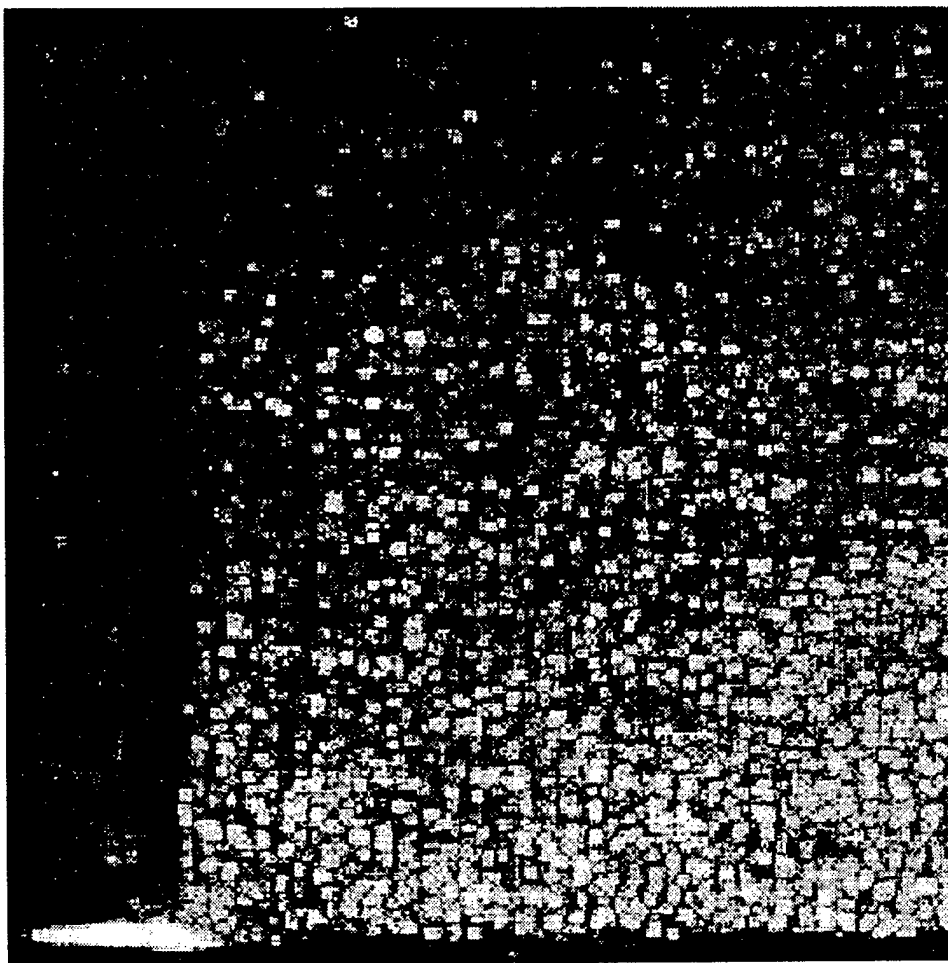Figure 4.1(a) Original image near the protrusion

Figure 4.1(b) Original image with 3 x 3 closing.

linear relation between input and output intensity values to a cubed relation. It was found that using a nonlinear output LUT allows for a more uniform contrast enhancement between areas of high particle concentration and low particle concentration. The ROI is then binarized using a pixel intensity threshold value of 90 to 100; any pixel intensity values below this threshold were set to 0 (black) and any pixel intensity values above the threshold were set to 255 (white). Figures 4.2(a)-(c) show the boundaries of each ROI and the results of the cubing contrast enhancement with subsequent binarization of the results. Progressing from top to bottom, each ROI output LUT remained the same except for an overall offsetting of the cubed function to higher pixel values. This upward offset corresponds to the lower grey level image values found in ROI's further from the test section wall. Threshold values remained approximately the same for all three ROI's, with a slightly lower threshold value of 90 for the ROI nearest to the wall. The final operation, shown in Figure 4.2(d), is a global 3 x 3 erosion which acts as a low pass filter breaking small connections between images which induce displacement correlation smear. Figures 4.2(e) and (f), figure 3.7(e) being of relatively good original image quality, are examples of before image processing and after image processing digitized files of the position used to obtain the velocity data analyzed in chapter 5.

The contrast enhancement and thresholding relations were optimized through an iterative procedure which produces the best contrast between particles and background. This optimization procedure was determined by interactive inspection of grey level histograms, produced by various processing techniques, and by visual inspection of results from randomly selected test cases. The grey level histograms were inspected for discrete peaks representing background grey levels and particle image grey levels. Particular contrast enhancement and thresholding techniques which produced histograms with the most discernable peaks between particle images and the background were chosen. Images were then inspected visually for contrast

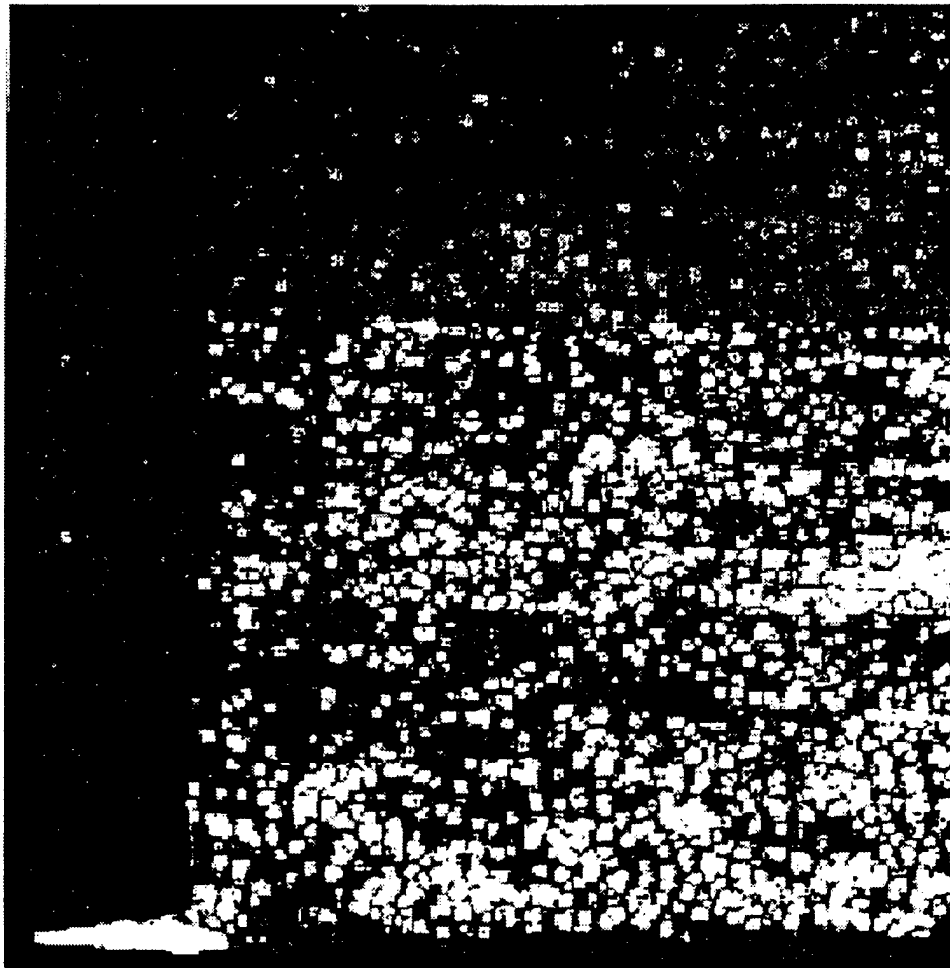Figure 4.2(a) Hypercube LUT and threshold at 90.

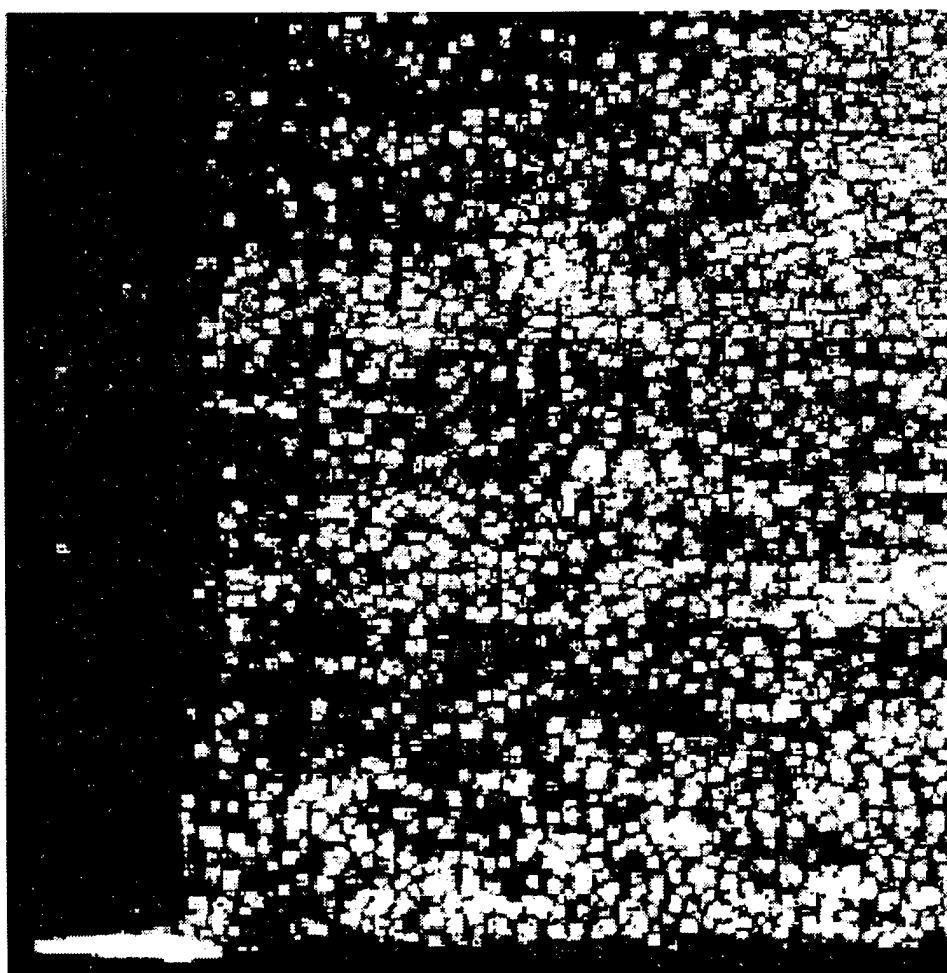Figure 4.2(b) Hypercube LUT and threshold at 90.

Figure 4.2(c) Hypercube LUT and threshold at 100.

Figure 4.2(d) Erosion (3 x 3)
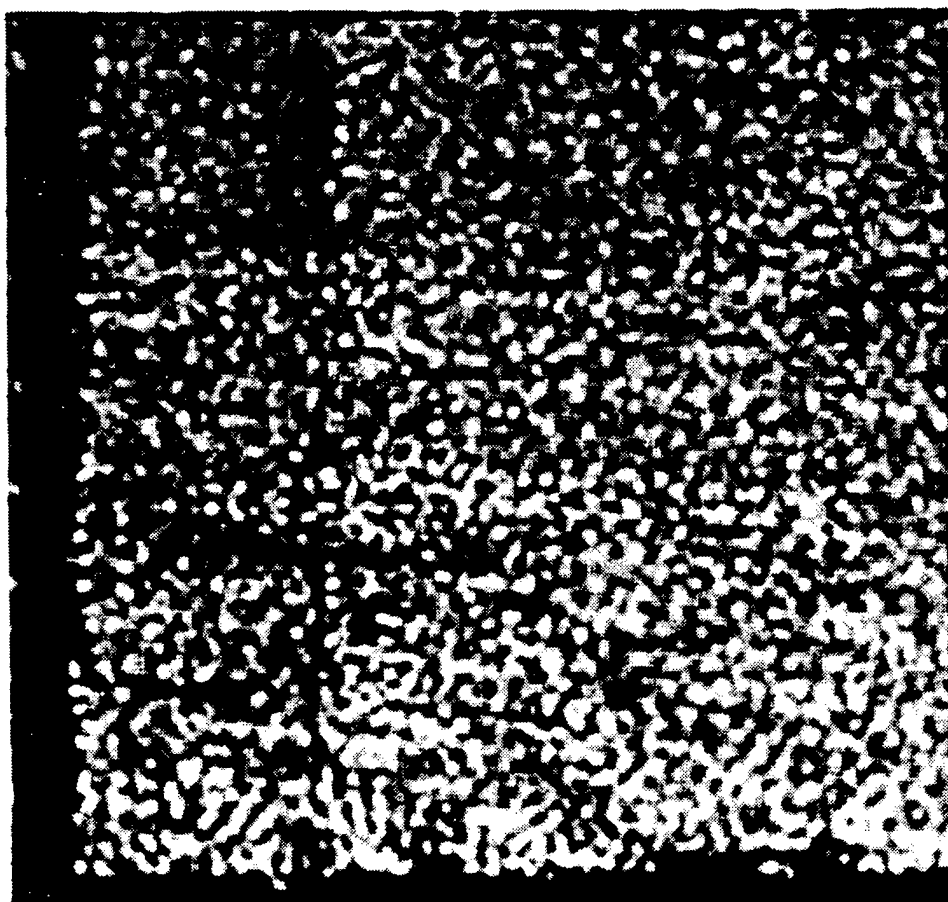
Figure 4.2(e) Original image 7.62 cm in front of the protrusion
(from data presented in Chapter 5).
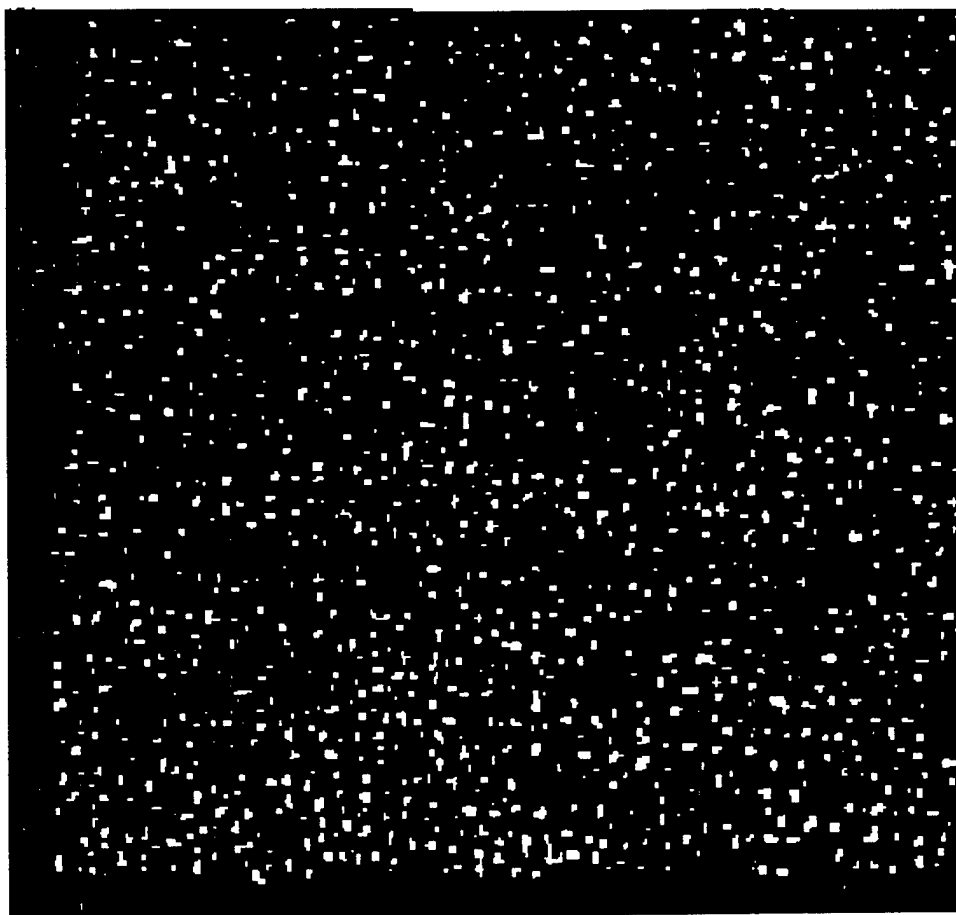
Figure 4.2(f) Finalized image from Figure 4.2(e)

and particle discreetness as compared to background. Thereafter an interactive 2-D FFT algorithm was used over random interrogation regions within the image. The first FFT produced Young's fringes and a second FFT the autocorrelation. This provided spot checks of displacement estimates for the purposes of evaluating the procedures. The combination of optimized processing methods was then used to enhance all raw particle images without user intervention.

4.3.   Statistical Analysis of Particle Images

4.3.1   Introduction

This section describes the statistical procedure used to analyze particle images. The analysis determines an average particle image displacement within a given interrogation region of a double exposured particle image frame. After a brief review of the basic principles underlying particle image displacement estimates (see section 2.1), the statistical procedure emphasizing an extended search region autocorrelation algorithm is described in its entirety while unique features and advantages of the process are given. A practical example of the extended search algorithm is then illustrated and an algebraic model given for completeness. Finally, specific parameters utilized for detecting correlation peaks as well as detecting the corresponding center or highest value position of the "valid" peak, with subpixel accuracy, are discussed and the procedure for determining the displacement values addressed. The extended search region procedure is similar to a technique used by Sridhar et al. (1991) with some refinements.

Though described here as an autocorrelation technique for analyzing double exposure, single frame image data, the extended search region correlation technique

can be applied to single exposure, multiple image frame data as a cross-correlation technique. If used with single exposure, multiple image frame data, the extended search region algorithm is similar to the one employed by Hassan and Canaan (1991).

4.3.2 A Brief Review

Recall from section 2.1 that PIV particle velocities are estimated from calculating the most frequently occurring particle image displacements within a defined window in pixel space called an interrogation region. The fundamental means of finding the most frequently occurring particle image displacement is to accurately match corresponding first exposure and second exposure images within the region. Matching of image pairs is made possible on the supposition introduced in section 2.1 that a unique grouping of particle images exists within each interrogation region which only correlates well with itself at future times. Though some statistical techniques match individual images (Hassan and Canaan (1991)) in order to determine image displacements, and hence are not PIV, this is usually only possible with multiple frame, single exposure image data. PIV algorithms avoid the difficulties and restrictions of trying to track individual particles by statistically analyzing the group of particle images contained within an interrogation region without regard to the positions or displacements of individual particles within the group.

For double exposure, single image frame data, the average displacement is typically found through a spatial autocorrelation process utilizing all pixels defined within the interrogation region. The position of the highest non-zeroeth order correlation peak affords the calculation of the average image displacement. The displacement is the distance in correlation space between the zeroeth order peak and

the highest correlation peak. As will be shown, the extended search region technique differs considerably from the aforementioned traditional autocorrelation techniques (see section 2.3.3).

It is possible to reduce the number of numerical operations when using the extended search correlation method if only the exposed pixels of a binarized image file are used for the correlation process. Furthermore, specific boundaries of the area of interest need not be rigidly defined. This physical and computational characteristic, can be used advantageously in reducing errors associated with large particle displacements and increases the effective particle image density per interrogation spot compared to conventional correlation techniques.

4.3.3 Extended Search Region Autocorrelation

4.3.3.1 The Algorithm

The procedure for analyzing the image begins with partitioning the image field into interrogation regions at specific locations corresponding to a cartesian coordinate system. To obtain individual velocity vectors, the image is sequentially analyzed one interrogation region at a time. The extended search region algorithm is used to build a correlation map, C_{fg}, for the present interrogation region centered at (f, g) in Figure 4.3(a) which portrays a portion of a 512 x 512 pixel space containing example double-exposed image data for the purposes of illustration. Within the example interrogation region, there are images which correspond to the first image of the image pair, designated Ip_1 and black, and there are the displaced images designated Ip_2 and cross-hatched for the purpose of example. The purpose of the correlation map is to show how well the double exposed images correlate with
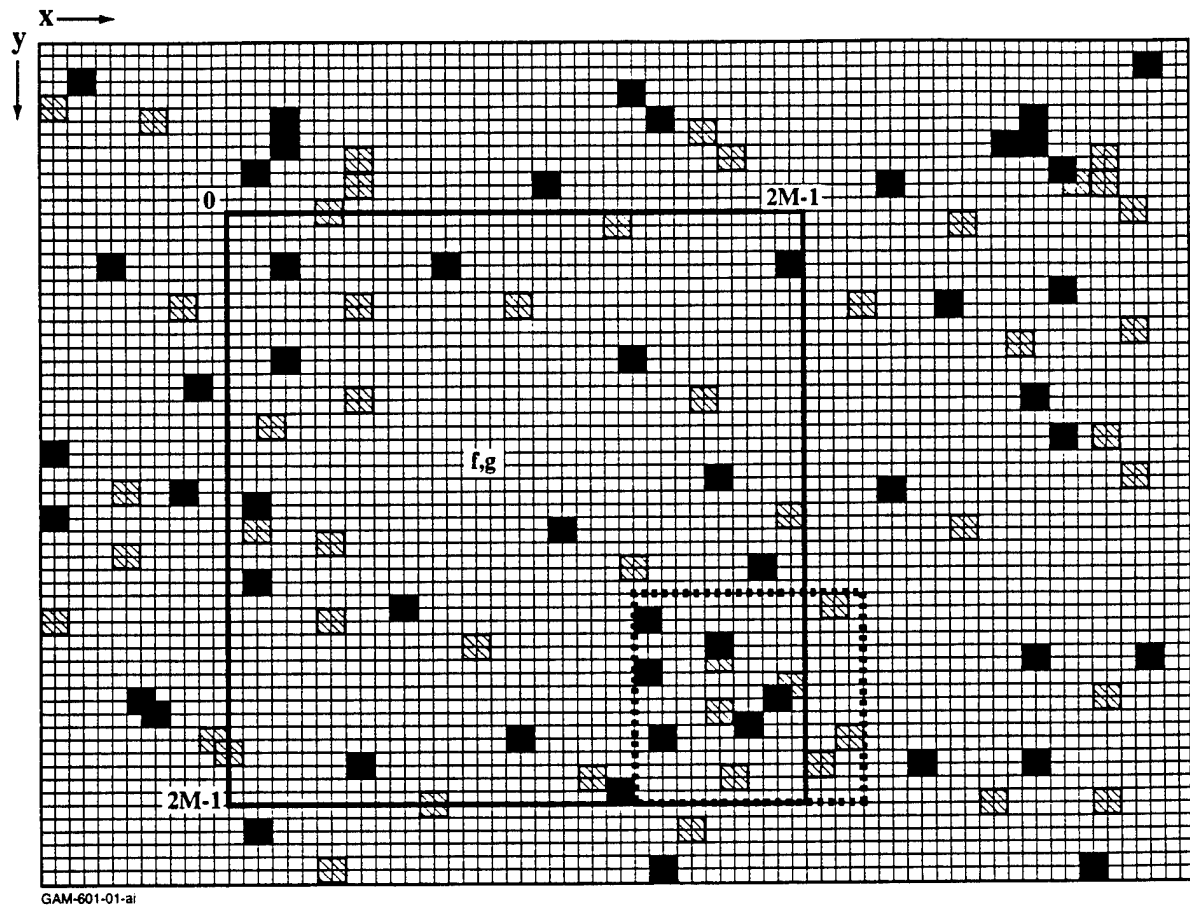
Figure 4.3(a): Example Particle Image field. Displacements are to the right 5 pixels and down 3

I_{p1} pixel - ■ I_{p2} pixel - ◨
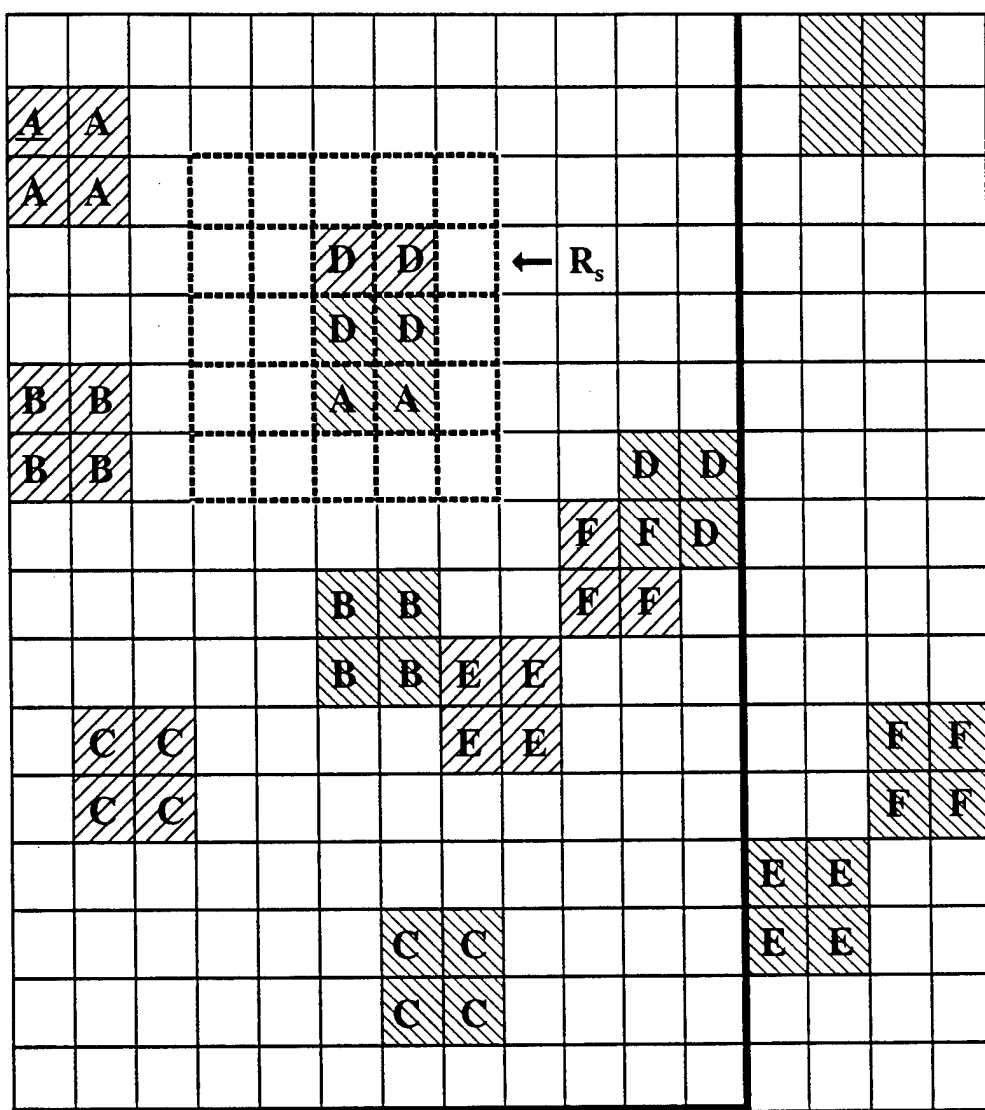
Figure 4.3(b): Subregion of 40x40 Interrogation Region from Figure 4.3(a) showing Ip₁ and Ip₂ pixels

———— Dark solid line marks edge of interrogation region

▪▪▪▪▪▪▪▪ Dashed line marks 5x5 roaming search region with center moved a "predicted" 5x3 pixels over from the top left Ip₁ pixel "A"

Ip₁ pixel - ▨ Ip₂ pixel - ▨

themselves with a displacement. The displacement which produces the highest correlation corresponds to the average displacement within the interrogation region provided the correlation meets criteria intended to reject noise.

After the particle image field is image processed to increase particle to background contrast (see section 4.2), all pixel values are converted into a binary format in which pixels defining particle images have values of one (1) and background pixels are assigned a value of zero (0). This significantly reduces the total number of algebraic operations carried out during the correlation process.

The range of displacements considered for a given exposed pixel in the interrogation region in building the correlation map covers a small search region R_s, of the image called the search region. Referencing Figure 4.3(b), which is the 16 x 16 pixel shaded section enclosed in the dashed lines in Figure 4.3(a), a *roaming* 5 x 5 pixels square search region, R_s, is defined in dashed lines. The center of the search region is positioned relative to an exposed source pixel $\underline{A}$ within the interrogation region. Only exposed pixels within the interrogation region are considered as source pixels since only exposed pixels can contribute to the correlation. Generally, this eliminates approximately 90% of the pixels within the interrogation region as source pixels resulting in a significantly reduced time to calculate the correlation map. A correlation is computed for each displacement between the source pixel $\underline{A}$ and a pixel position within the search region R_s. The correlation is computed as 0 if the pixel within the search region is unexposed and 1 if the corresponding pixel in the correlation map is exposed. For each position within the search region, which in this case is 5 x 5 pixels square, the corresponding correlation value is added to the same position within a 5 x 5 array making up a correlation map. Since the outcome of the correlation computation for a pixel in the search region is equal to the search region pixel's value, 0 or 1, the process is reduced to adding the contents of the search region array to the corresponding location of the correlation array for each exposed pixel.

The search region is then moved with the same relative displacement to the next exposed source pixel within the interrogation region and the process is repeated. Once this process has been completed for each exposed source pixel within the interrogation region, the resulting correlation map in displacement space is examined for the highest correlation peak and whether or not this peak is valid displacement peak. Section 4.3.4 describes the peak detection criterion. The next few paragraphs describe the mechanics of the correlation algorithm.

The interrogation region for the extended search region correlation technique need only contain pixels belonging to first exposure or Ip_1 particle images. Pixels defining second exposure or Ip_2 images need not lie within the interrogation region. The position (i, j) of all exposed pixel positions within the image frame are stored in a two-dimensional array IPA(i, j) for the entire 512 x 512 pixel space. Exposed pixel locations within the chosen interrogation region, for example, a 40 x 40 pixel region in Figure 4.3(a) centered on pixel (f, g), are identified and stored in a two-dimensional array, IPB(l, d). Index l numbers the exposed pixels within the interrogation region while index d, with values of either 1 or 2, indicates whether the array IPB holds a column value j or a row value i, respectively.

The roaming search region, R_s, is then defined and typically has an odd number of rows and columns. R_s is square with sides $2N+1 = 5$ for this example and is initially located at a "predicted" displacement, in pixel space, from the first exposed pixel position given by array IPB(l, d) within the interrogation region. The local origin, pixel $(0, 0)$, is located at the upper left pixel of the interrogation region. However, for the purpose of example, the origin $(0, 0)$ is considered as the top left pixel of the 16 x 16 pixel image in Figure 4.3(b).

The "predicted" displacement, given by (dx, dy) in the x and y directions respectively, is determined from taking the average displacement, in x and y, of four previously estimated displacement vectors on the interrogation region row directly

above the current interrogation position and the two preceding displacement vectors on the same row. If one of the preceding vectors does not exist (i.e., a dropout) then it is not used in the averaging calculation. Furthermore, if a number of the preceding vectors do not exist then the preceding vector average is used for the guess displacement. When the interrogation procedure is started, an approximate displacement profile guess is made to initiate the averaging process; in the near-wall pipe flow studied here, a linear gradient is used.

A unique aspect of the extended search algorithm is that the search region need not fall within the interrogation region during the correlation process. This has a number of advantages over standard techniques which use only pixels within the interrogation region for the correlation process. Allowing R_s to *extend* outside the interrogation region reduces the loss of pairs effect, within the plane of measurement, as well as gradient bias discussed in section 2.4.3. Even though Ip_2 particles may leave the interrogation region because they are near the edge of the interrogation region or they have large displacements relative to the interrogation region size, the effective image pair density, N_i, remains essentially the same as if image displacement were much smaller than the interrogation size. The end effect is the ability to use smaller interrogation regions relative to the displacement size for a particular flow field. Though it could be argued that the effective size of the interrogation region is determined by the original interrogation region plus the search pixels outside the interrogation region, this is not entirely correct since the uniqueness of the extended search is that the search region is not restricted to the interrogation region itself. Furthermore, gradient bias is reduced since larger particle image displacements within a gradient are obtainable, no longer biasing displacement estimates toward smaller values. However, the detection bias, or correlation peak smearing, described in section 2.4.3 remains.

Another advantage with the extended search region over traditional techniques

is that the search region size may be varied from interrogation region to interrogation region. This enables optimization of the algorithm for computation time and/or displacement peak detectability based on local conditions. The smaller the search region, the smaller the correlation computation time, but the larger the search region, the greater probability of finding a correlation peak with the search region. Though not incorporated in the present study, the size of the search region could be based on confidence estimates for the initial guess displacements by which the position of the search region is placed relative to each exposed source pixel. The higher the confidence interval on the guess displacement, the smaller the search region size. Though small search region sizes are desirable, large search regions are helpful when interrogating image data from nonhomogeneous turbulent flow fields with relatively large turbulence intensities. If the search region is too large, the probability of calculating invalid correlation peaks or noise peaks increases.

4.3.3.2   A Practical Example

Consider Figure 4.3(b) as well as Figure 4.4 for an example of the correlation process using the shaded 16 x 16 pixel section of the interrogation region in Figure 4.3(a). The tables in Figure 4.4 show the contribution to the 5 x 5 correlation map from each group of exposed pixels, A through F, on the section of the interrogation region shown in Figure 4.3(b). Subscripts 1 and 2 are used to denote when the initial exposure, Ip_1, or the second exposure, Ip_2, is being considered. If images overlap, such as D_1 with A_2 on Figure 4.3(b), the correlation process is not affected since the method is not concerned with whether image overlap occurs. Second exposure particle images, such as B_2 on Figure 4.3(b), are treated as if they were a first exposure Ip_1 image in the correlation computation process.

(A)

	1	2	1	
	2	4	2	
	2	4	2	
	1	2	1	

(B1)

	1	2	1	
	2	4	3	2
	1	2	3	4
			1	2

(C)

	1	2	1	
	2	4	2	
	1	2	1	

(D)

	1	2	1	
1	3	4	2	
2	5	5	2	
3	4	3	1	
3	2	1		

(B2)

2				
1				
			1	2
			2	3
			1	1

(E)

			2	3
	1	2	2	2
	2	4	2	
	1	2	1	

(F)

	1	2	1	
1	3	4	2	
4	5	3	1	
5	4	1		

(R_s)

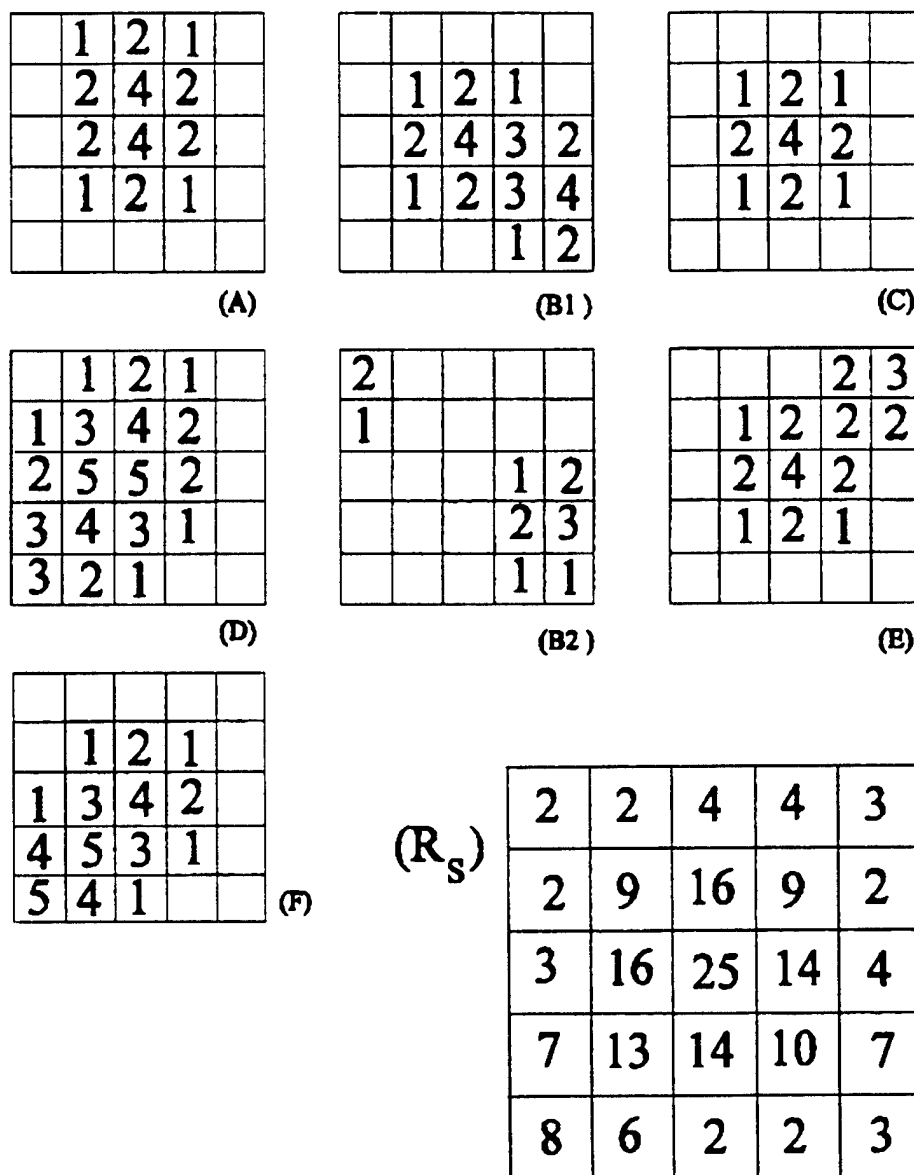| 2	2	4	4	3
2	9	16	9	2
3	16	25	14	4
7	13	14	10	7
8	6	2	2	3

Figure 4.4 Correlation map of subregion and tabulated values

Initially, all exposed pixels within the interrogation region are considered Ip_1 pixels and the exposed pixels over which the search region lies are considered *candidate* Ip_2 pixels. Here, candidate is used since the possibility exists that the pixels may be part of an Ip_1 image. Though incorrect matchings of Ip_2 pixels occur and incorrectly add to the correlation map, they are uncorrelated and add only to general background noise level. Furthermore, if enough particle pairs are present (Adrian (1991) and Loeurenco (1987)) within the interrogation region, the background noise from uncorrelated pixel matchings will be sufficiently below the correlation peak, making up a "good" correlation, for valid peak detection.

Also, notice that the search is extended outside the interrogation region. For example, in Figure 4.3(b), displaced Ip_2 particle images E_2 and F_2 lie outside the interrogation region yet are used in the correlation process when the position of R_s is defined by Ip_1 particles E_1 and F_1. The end result is a correct detection of the dx = 5, dy = -3 particle image displacements within the 16 x 16 pixel region of the interrogation region considered in this example.

4.3.3.3   An Algebraic Model

This section presents an algebraic model of the extended search region algorithm. When modeling the extended search region algorithm, it is useful to consider the search region R_s as essentially an image processing *mask* used to build a two-dimensional histogram which is analogous to the correlation coefficients of Hassan and Canaan (1991) as well as Keane and Adrian (1991). This is because the image is binary so that the correlation itself is never really computed. Only the occurrence of pixel values of 1 are recorded as functions of relative position to other pixels of value 1.

If a value of 1 exists in one of the pixel positions defined within the mask, a value of 1 is added to the corresponding two-dimensional position within the histogram, i.e. correlation map $C_{fg}(m, n)$. The correlation model is as follows:

$$C_{fg}(m, n) = \frac{\sum_{l=1}^{S} \left[\sum_{m=0}^{2N} \sum_{n=0}^{2N} IPA \left(IPB \ (l, \ 1)+dx-N+m, \ IPB \ (l, \ 2)+dy-N+n \right) \right]}{S + \sum_{p} \sum_{q} \left(IPA(p, \ q)\big|_{(p, \ q) \ \epsilon \ IPB} \right)}$$

4.1

$$\text{where:} \quad \begin{array}{c} m \ , \ n \ \epsilon \ [1,2N+1] \\ i \ , \ j \ \epsilon \ [1,2M] \\ f-M+dx-N+1 \ \leq \ p \ \leq \ f+M+dx+N \\ g-M+dy-N+1 \ \leq \ q \ \leq \ g+M+dy+N \end{array}$$

Here, S is the number of exposed pixels within the interrogation region, while p and q are indices which mark minimum and maximum pixel positions over which the search region roams in x and y respectively. Notice indices (p, q) from the above correlation equation need not match the boundaries of the interrogation region and in general do not. The numerator represents the summation, as a function of position (m,n), of the binary product between each Ip_l pixel value, whose positions given in array IPB define the positions of R_s, and each pixel value from array IPA whose pixel position is overlaid by respective positions in R_s.

The correlation values are normalized with the exposed pixel count to facilitate setting criterian, discussed in section 4.3.4, to determine if a correlation peak is a single or plural candidate for the displacement vector or should be rejected as noise. The denominator represents the number of exposed pixels contained within the interrogation region plus the number of exposed pixels outside the interrogation region used during the correlation process. Ideally, the highest correlation value is 0.5. Correlation values may be greater than 0.5 however due to image overlap, large

out-of-plane displacements and incorrect matching of Ip_2 pixels with other Ip_2 pixels.

When applied to double exposure, single image frame data, the extended search algorithm is similar to the algorithm used by Sridhar et al. (1991), but the present extended search algorithm uses only exposed pixels within the interrogation region, reducing the extended search algorithm to an easier to implement histogramming method. The major advantage is the significant reduction in the overall number of numerical operations, and hence computation time per interrogation region for all other parameters equal, as compared to the method employed by Sridhar et al. (1991).

4.3.4 Correlation Peak Detection Parameters

To be classified as a peak, a correlation map position must have a correlation value which is first, above a predetermined threshold and second, equal or greater in magnitude than any if its neighboring correlation values. Though more than one correlation peak may exist within the correlation map, typically, one correlation peak has a larger value than all the rest. It is necessary to determine if the maximum correlation within the correlation map represents a valid displacement or noise. As mentioned in section 2.4.4, noise peaks may be detected if the displacement peak is comparable to the background noise level. Keane and Adrian (1990) give three methods to discern good correlation peaks over noise peaks: First, confine the search for the displacement peak to only the region were the peak is expected. Second, define some threshold value which the peak magnitude must be greater than to be considered valid. Lastly, Keane and Adrian suggest using the previously discussed "detectability", D_o, being the ratio of the first largest peak to the second largest peak (see section 2.4.4). Except for detectability, these techniques are used in the present

study for discerning valid peaks.

For the peak determination carried out here, a normalized threshold value of 0.2 was used. This value was determined through interrogating test images randomly chosen from the image data taken from the turbulent pipe flow in the glycerin tunnel. A graphical interface was developed to help this evaluation. As shown in Figure 4.5, the interrogation region and search region boundaries are graphically displayed alongside a color coded representation, which is grey scale in this copy, of the correlation map. Next to the correlation map are the numerical values of the highest and next highest peaks and their ratios to each other as well as their ratios to the average background correlation level. The average background correlation level is defined by taking all correlation values which have not been classified as peaks and averaging their values. By graphically comparing the actual pixels within both the interrogation and search regions next to the computed correlation map, it was possible to study the effects of variables such as the threshold level, the interrogation region size and the search region size on the correlation map.

Though detectability is a suggested method for validating true displacement peaks, the numbers recommended by Keane and Adrian did not work for the correlation maps from images produced during this study, nor could detectability values be found which could in and of themselves accurately identify valid displacement peaks for the images tested. This is not surprising considering the varied possibilities for original image quality within any experiment. However, it was found that interrogation region size, search region size and peak threshold level could be defined, for the particular flow field, such that dropouts could be minimized and invalid vector detection maintained. If a bad vector is calculated using the preselected interrogation and search region sizes, the vector is generally rejected because there are too many peaks above the threshold, too many peaks with the same magnitude, the displacement is too small or the displacement is extraneously large. A

lmax:686   Elmax:975   size: 14
intx: 88   inty: 88
ioff: 12   joff: 2
m: 52   n: 36
            File number: 0

pk1a:	2.094	pk1:	212	▇	i1:	6	j1:	9
pk2a:	.000	pk2:	0	▨	i2:	0	j2:	0
pk3a:	.000	pk3:	0	▤	i3:	0	j3:	0
pk4a:	.000	pk4:	0	▥	i4:	0	j4:	0

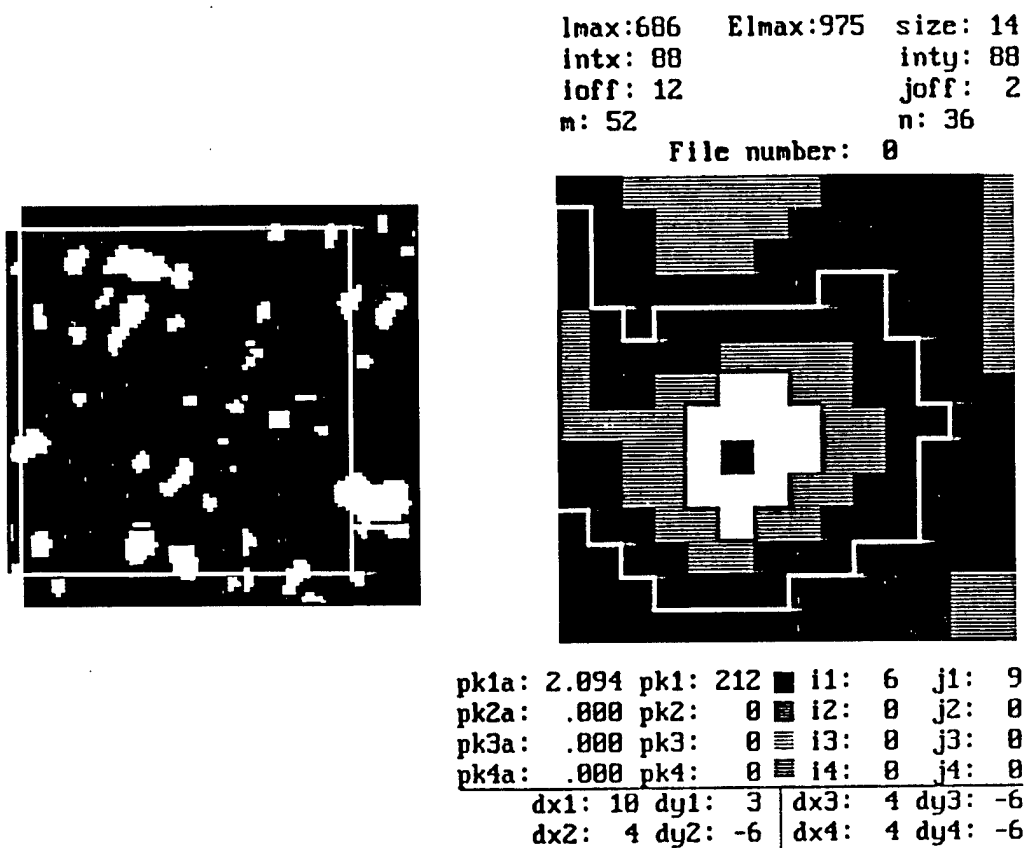| dx1:	10	dy1:	3	dx3:	4	dy3:	-6
dx2:	4	dy2:	-6	dx4:	4	dy4:	-6

Figure 4.5 Graphics of interrogation region, search region limits and correlation map

displacement is defined as too small if the correlation peak is within one average particle image diameter. Extraneously large displacements may occur in regions where image density is sparse.

In this way, the optimum search region size was determined experimentally to be four times an average particle image size plus 1 pixel. The average particle image size was determined by examining a number of particle images and is approximate for estimating purposes. The interrogation region size was set at 80 x 80 pixels giving an interrogation size of 6.25 wall units. This number is somewhat larger than the LDV probe volume size of 1.8 wall units and 0.17 wall units for the major and minor axes, respectively, used by Fontaine (1993) in the same facility. The relatively large interrogation size is a direct result of seeding density problems and laser beam attenuation problems further from the test section wall.

Frequently, there are multiple peaks which are of equal magnitude in the correlation map. This may occur when correlation peaks from a binary image of a particle more than a few pixels in diameter occupy a number of adjacent pixels. Due to this, the five largest peaks are retained in the correlation peak analysis for processing. Five is chosen since the average particle diameter for the present turbulent pipe flow field after image processing with the system magnification used is five pixels. If any of the peaks are equal in magnitude and are more than one pixel away from another peak without being connected together by yet another peak of equal magnitude, the displacement vector is considered a dropout and no further processing is carried out at the location. Equal correlation peaks separated within the correlation map may exist when the particle image field is sparse.

4.3.5   Subpixel Peak Determination

As described in detail above, displacement information is determined by finding the pixel position corresponding to the maximum autocorrelation value. The technique can determine displacement values to the nearest pixel without extensions. The correlation values near the correlation maximum provide information which allows for estimation of the position of the correlation peak to subpixel accuracy. It is possible to approximate the centroid of the correlation peak using a weighted average of the correlation values surrounding the correlation peak. Parabolic and Gaussian curve fits may also be used and have been found to reduce numerical errors approximately by half over a centroid technique (Prasad, Adrian, Landereth, Offutt, (1992)). However, this error reduction occurs only in the case when velocity gradients are negligible. Otherwise, the centroid technique is superior and is used for the present turbulent pipe flow experiment. The averaging used to locate the correlation centroid in the present study is a modified form of that suggested by Kim (1991). Varying forms of centroid techniques are discussed in Adrian (1988), Keane and Adrian (1990) and Adrian (1991). A linear weighted interpolation was used to estimate the location of the centroid of the autocorrelation peak with values of the surrounding displacements in the correlation map:

$$X = \frac{\sum\limits_{i=1}^{m} \sum\limits_{j=1}^{n} i \cdot C(i,j)}{\sum\limits_{i=1}^{m} \sum\limits_{j=1}^{n} C(i,j)} \qquad\qquad Y = \frac{\sum\limits_{i=1}^{m} \sum\limits_{j=1}^{n} j \cdot C(i,j)}{\sum\limits_{i=1}^{m} \sum\limits_{j=1}^{n} C(i,j)} \qquad 3.5$$

Variables (i, j) are the positions of the surrounding autocorrelation values within the correlation map. The interpolation indices are variable and depend on the number of adjacent correlation peaks of equal magnitude and their positions. Beginning and

ending indices give the coordinates which define the smallest boundary, plus one pixel on all sides, which contain all the prescribed peaks. In this way all the peaks and surrounding information are used to determine a displacement vector of subpixel resolution.

4.4   Velocity Field Post-Processing

Post-processing of the 2-D displacement information, resulting from the interrogation process, into velocities vectors and associated statistics is a three step procedure. First, the false image shift displacements were subtracted from each displacement vector. Next, a corrected value for the time between sweeping illumination beams, Δt, was estimated for and applied to each measured displacement vector over all digitized image frames. Finally, the velocity vectors corresponding to each interrogation region position within every digitized image frame were ensemble averaged and second order statistics calculated. In order to decrease the uncertainty of the velocity statistics, all ensemble averaged velocities at vertical positions corresponding to particular y^+ = constant values and upstream of the Gaussian protrusion were line averaged. Line averaging was made possible on the approximation that the flow field is fully-developed and a statistically homogeneous function of downstream position.

Image shift values are experimentally determined using calibration files taken during the image acquisition process. Particle images were acquired for this purpose in the same fashion as described in section 3.4.3, but with no flow in the test section. Individual image shift files were separately interrogated for a displacement vector at each position corresponding to interrogation region positions selected for actual particle image files. The resulting image shift displacement vectors for each

interrogation region position were ensemble averaged using the same process employed for turbulent pipe flow velocity vectors. For all image frames, the averaged image shift displacement was subtracted from each turbulent pipe flow displacement corresponding to the same interrogation region position within the flow field as the image shift displacement. Nine ensembles were used for image shift averages. Nine was chosen as a balance between obtaining accurate velocity averages, film cost, time and developing. Interrogating image shift only image data is seen as a more accurate method of determining image shift displacement than purely theoretical methods since the experimental method takes into account unknown variables such as strong wall curvature and surface deformations in the acrylic test section walls. As discussed in section 3.4.3 however, directly subtracting the image shift from measured displacements is only an approximation since the actual image shift is a function of particle velocity.

Once image shift displacements were subtracted from the pipe flow displacements, the corrected time intervals between beam sweeps were determined for and applied to each displacement vector as described in section 3.4.3. All index of refraction related corrections were applied to each time interval as a function of position within the flow field.

The resulting velocity vectors corresponding to each interrogation region position within each individual image frame were ensemble averaged and the second order statistics calculated. Each position has an associated average velocity, variance and turbulence intensity for both u and v components and an average uv correlation. Due to possible velocity dropouts at each position, the actual number of ensembles which make an average at any particular position can be different. To obtain accurate averages and second order statistics, velocities at each position in the flow field were separately ensemble averaged taking into account the difference in the number of ensembles per interrogation region position.

Because of the fully-developed turbulent condition characterizing the glycerin flow field upstream of the Gaussian protrusion, an additional approximation was utilized to increase the number of ensembles used in calculating the first and second order velocity statistics. Once fully-developed turbulent flow is achieved, the turbulent statistics are theoretically independent of the streamwise position. With this in mind, another group of first and second order statistics was constructed by summing all the velocities along a line of constant y distance from the test section wall in front of the Gaussian protrusion. Many thousands of ensembles are needed for a turbulent flow to obtain velocity accuracies on the order of one percent or better; However, using the line averaging approximation, the number of possible ensembles was increased from 60 to 2340 to reduce statistical uncertainty. The variance, turbulence intensities and average uv cross-correlations were determined for the increased number of ensembles.

Chapter 5

TURBULENT PIPE FLOW EXPERIMENT

AND PIV RESULTS

5.1   The Experiment

5.1.1   Introduction

As stated in chapter 1 and mentioned here for completeness, the motivation behind this study was the need to develop and experimentally qualify a particle image velocimetry system to aid in the interpretation of LDV velocity measurements taken within an existing unsteady turbulent flow field. The flow field is a fully-developed turbulent pipe flow, with glycerin as the fluid medium, with a small Gaussian shaped wall protrusion mounted on the acrylic test-section wall. Fontaine (1993) studied the flow field about the protrusion in order to understand its effects on Reynolds stress production within the buffer region of the pipe flow near wall region. In an attempt to resolve the form of the dominant flow structures downstream of the protrusion, Fontaine (1993) used conditional averaging techniques. A particle image velocimetry system, providing an instantaneous velocity "picture" of the desired flow field, would aid in the interpretation of conditionally averaged LDV data.

In order to validate the current DBS-PIV system measurement accuracy, velocity profile statistics determined with PIV measured velocities within this undisturbed fully-developed turbulent pipe flow are compared to previously measured velocity profile statistics obtained by laser Doppler velocimetry in the glycerin tunnel by Fontaine (1993) at the same operating conditions.

Relevant flow parameters and facility details are discussed below.

5.1.2   The Flow Facility

The Dual-beam PIV was evaluated experimentally using the glycerin tunnel at ARL/Penn State. As shown in Figure 5.1, the flow facility is a closed loop pipe flow which uses a 96% glycerin / 4% water solution and is driven by a 75 KW constant speed centrifugal pump. The upper section is a 7.6 m long cylindrical pipe with a 28.5 cm inside diameter which leads into an optically clear acrylic test section. A nozzle with a 16:1 area contraction connects the settling chamber to the test pipe. A detailed description of the tunnel is given by Chevrin (1988) and Bakewell (1966).

The settling chamber contains a honeycomb section, shown in Figure 5.1, and screens for turbulence management. The honeycomb is made of 15.24 cm thick welded stainless steel with a 0.95 cm cell size. A 0.10 cm serrated trip ring is located just downstream of the nozzle exit so as to fix boundary layer transition at the upper pipe entrance.

The test section, shown in Figure 5.2 and Figure 5.3, is a 50.0 cm long acrylic pipe encased by a glycerin filled acrylic box located 7.1 m from the pipe entrance. The combination of the flat surface of the outer acrylic box with the close index of refraction match between the acrylic, n_a=1.49, and glycerin, n_g=1.46, reduces the lens effect incurred by the curved walls of the test section.

The mean flow Reynolds number is controlled by adjusting the strongly temperature dependent viscosity of the glycerin through the use of a counter-flow heat exchanger. The temperature is maintained by controlling the flow rate of water through the heat exchanger. All PIV measurements are carried out at a glycerin temperature of 34.5°C as measured by a thermistor roughly 0.6 m downstream of the acrylic test section. The 34.5° C operating temperature permits a direct comparison of the present PIV measured velocity data to the LDV measured velocity data of
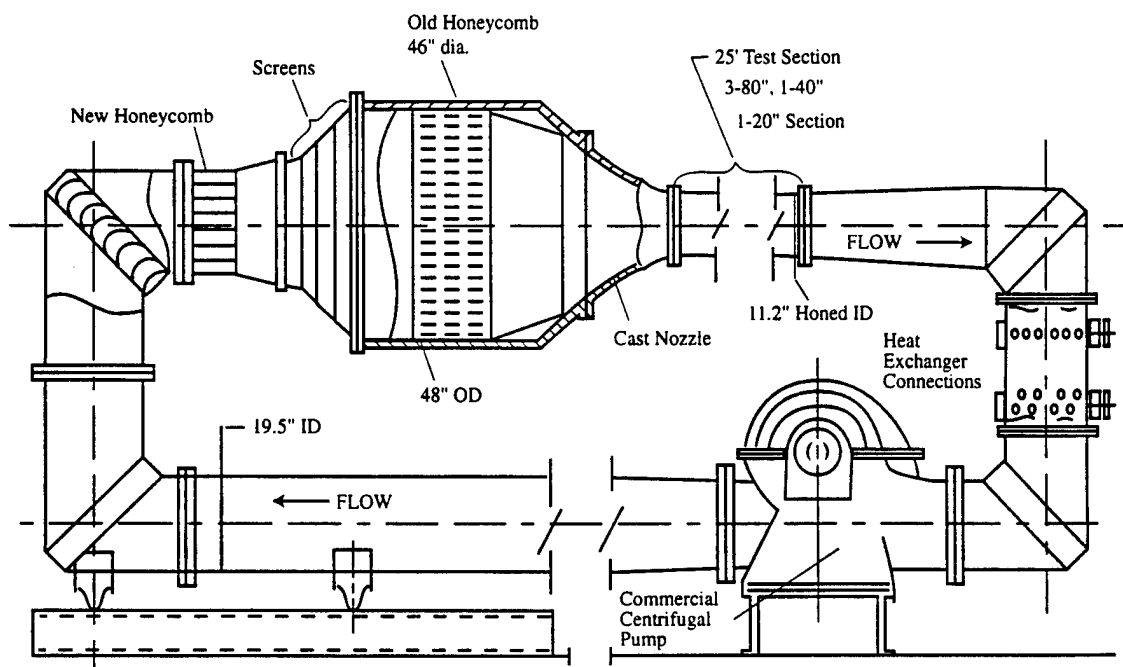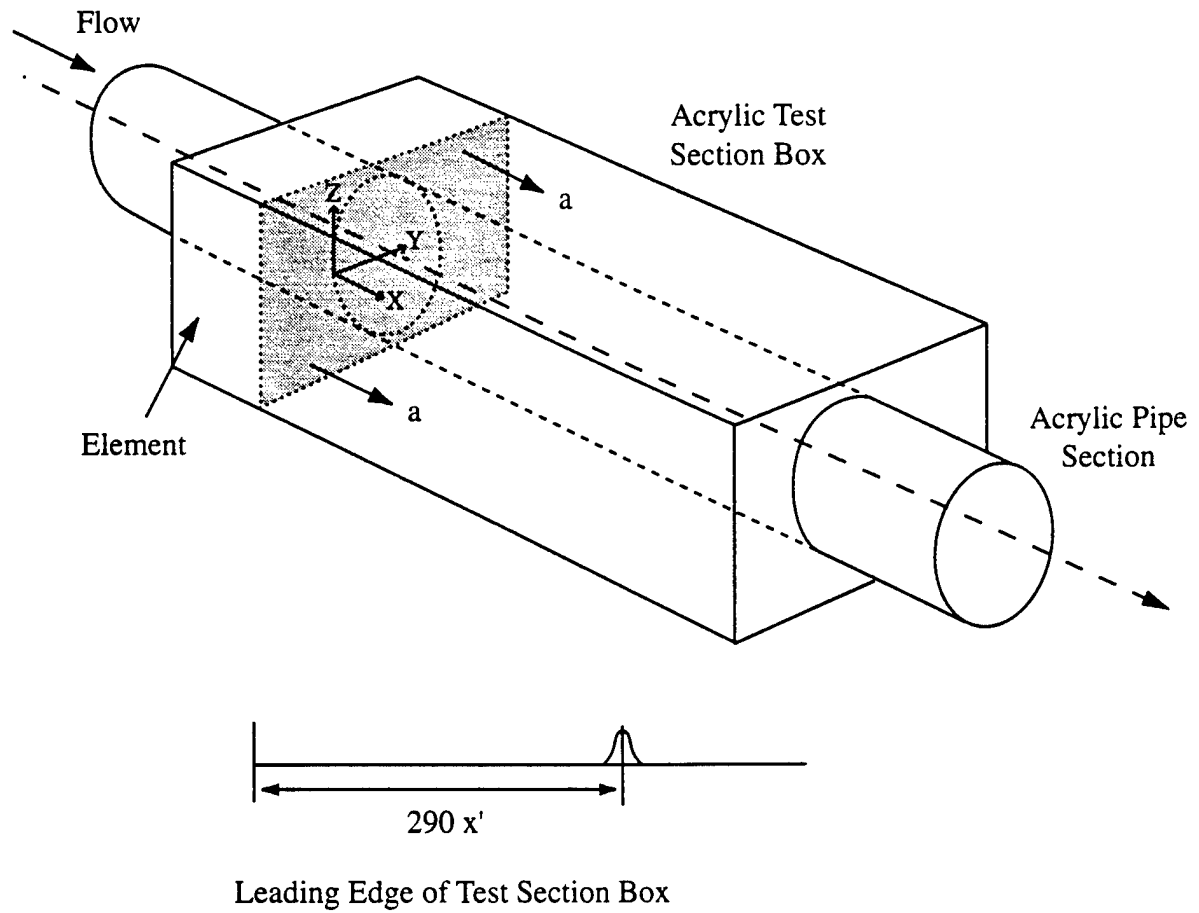
Figure 5.1 Glycerin tunnel facility

Figure 5.2 Illustration of glycerin tunnel test section showing location of bump and measurement coordinate system

a – a Cross–Sectional
View of Test Section

Protuberance

z^+

a $\dfrac{\text{Horizontal}}{\text{Center Plane}}$

y^+

Coord.
System
Origin

Tunnel Wall

a

⊗ Flow Direction into Plane of Paper
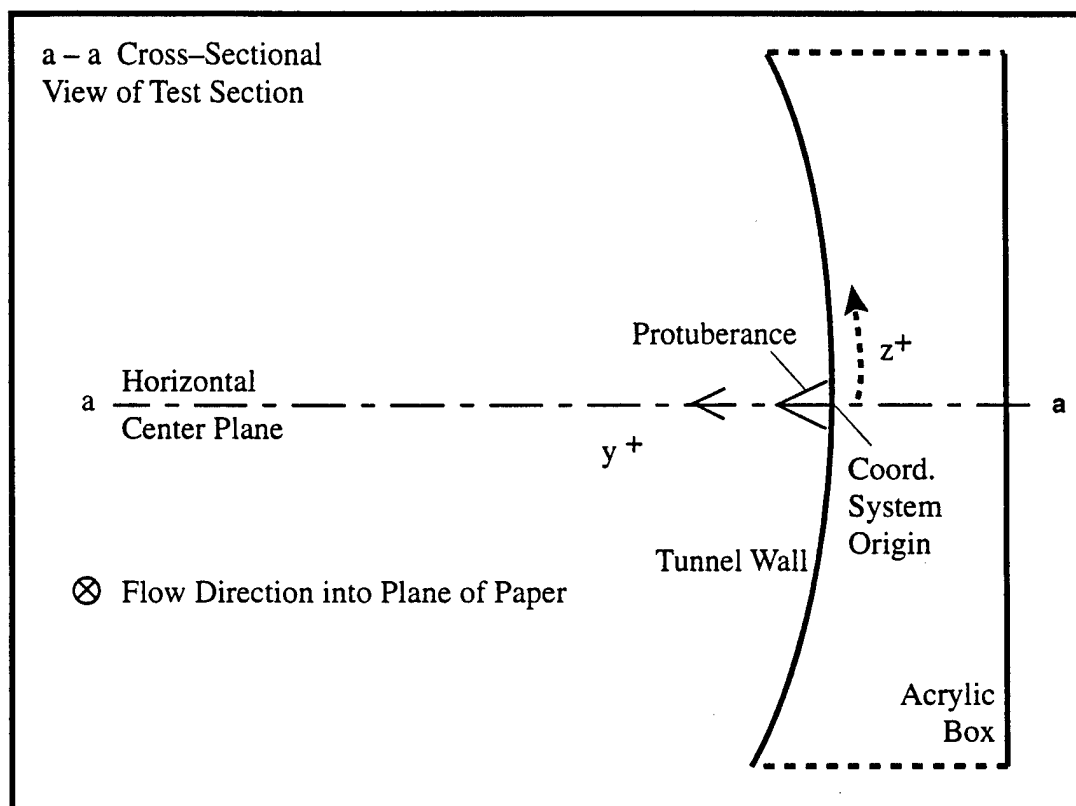
Acrylic
Box

Figure 5.3 b) Cross-sectional view a-a

Fontaine (1993). This temperature setting resulted in a bulk velocity of 6.6 m/s, producing a fully-developed pipe flow at a mean flow Reynolds number, Re_D, of $10{,}110 \pm 500$ as determined by Fontaine (1993). All uncertainties are determined by normal distribution 95% confidence intervals as described in Coleman and Steele (1989) or the student-T test. The glycerin/water mix temperature dependence as measured by the Cannon Instrument Company is shown in Figure 5.4. Pertinent glycerin properties and tunnel operating conditions are given in Table 5.1 for a glycerin temperature of 34.5°C.

Because the viscosity of glycerin is roughly 186 times greater than the viscosity of water, the glycerin tunnel provides a large viscous length scale and a narrow turbulence frequency bandwidth, approximately 0.0465 cm and 860 Hz, respectively, so that excellent spatial and temporal resolution may be obtained.

The smallest flow scales, the Kolmogorov microscales, are determined from a relationship between the kinematic viscosity and the characteristic flow viscous dissipation rate (Tennekes and Lumley (1972)). They are defined as a time scale $\tau = (v / \varepsilon)^{1/2}$, a length scale $\eta = (v / \varepsilon)^{1/4}$ and a velocity scale $\upsilon = (v \varepsilon)^{1/4}$. An empirical relationship for the viscous dissipation $\varepsilon \approx (4u_*^2 U_{avg}) / D$ is used from Bakewell (1966). For the conditions under which PIV data was taken, the Kolmogorov time scale is $\tau \approx 3.48$ msec while the Kolmogorov length and velocity scales are $\eta \approx 0.804$ mm and $\upsilon \approx 0.231$ m/s, respectively.

The PIV data given in section 5.2 were measured within the buffer region and laminar sublayer, $y^+ \le 30$, where the nondimensional velocity profile for fully-developed pipe flow is well documented. Within this region, the measured distance from the test section wall, y, is nondimensionalized by the viscous scale v/u_*, where v is the kinematic viscosity and u_* is the friction velocity. This nondimensional distance is known as a wall unit and defined as $y^+ = y u_*/v$, where $u_*^2 = \tau_w/\rho$ (Tennekes
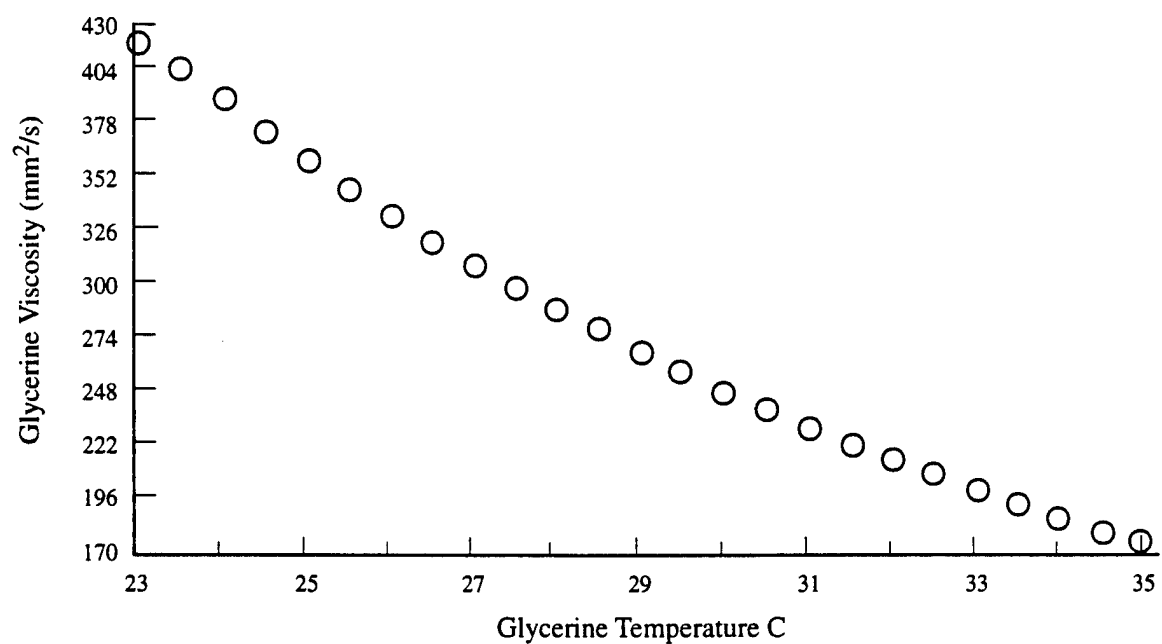
Figure 5.4   Temperature dependence of glycerin kinematic viscosity

Table 5.1   Glycerin Properties and Tunnel Operating Conditions at 34.5°C

ν = 186 E-6 m²/s

n = 1.465

ρ = 1242 kg/m³

Re_D ≈ 10110

Re_θ ≈ 730

Re_* ≈ 613

U_b = 6.6 m/s

u^* = 0.4 m/s

1 y^+ ≈ 0.465 mm

1 f^+ ≈ 860 Hz

and Lumley (1972)). Here, viscous length and wall unit can be used interchangeably. The wall mounted bump or protrusion contour as mounted on the test section wall is illustrated in Figure 5.5. The contour of the bump is a Gaussian distribution with the exact mathematical shape defined in Fontaine (1993). The location of the protrusion in the test section is shown in Figure 5.2 with the darkened section a-a enlarged in Figure 5.3. The protrusion is located 290 wall units (13.5 cm) downstream of the beginning of the box enclosing the test section and has a height and width of 16.43 and 13 wall units respectively. Throughout this report, the undisturbed pipe flow conditions are used for nondimensionalization.

The protrusion diameter decreases with distance from the wall to keep the local Reynolds number below the critical value of 50 as suggested by White (1974) to prevent Strouhol shedding. Strouhol shedding would add undesired complexity to the already complicated flow field. This local Reynolds number is based on the local protrusion diameter and the local mean velocity in the unperturbed flow. The maximum local Reynolds number is $Re_d = 36$ at $y^+ \approx 8$.

A cylindrical coordinate system is used with the origin centered on the base of the protrusion, see Figure 5.3. The axial coordinate, x, is measured in the downstream positive direction along the pipe axis and the azimuthal coordinate z is measured as the circumferential displacement defined by $z = R\theta$. R is the radius of the test section and θ the angle, positive in the counter-clockwise direction looking downstream, made between the center of the test section and some circumferential position along the test section wall. The radial coordinate y is defined as $y = R-r$, where r is the distance from the measurement point to the test section center; y is measured as the displacement from the test section wall.
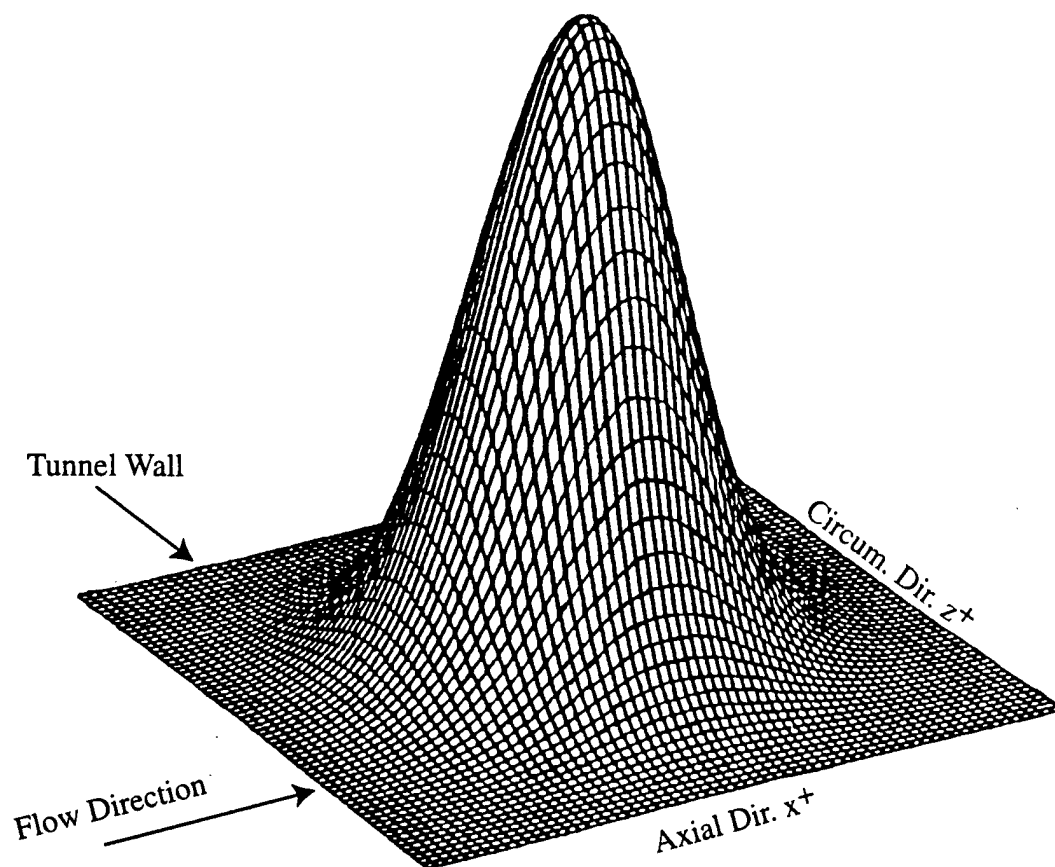
Figure 5.5 Illustration of the wall-mounted bump

5.2   PIV Experimental Data

5.2.1   Introduction

As stated in chapter 1, the usefulness of PIV lies in its ability to resolve multi-point velocities with accuracies approaching that of LDV single-point measurements. In order to evaluate the DBS-PIV approach, a direct comparison is made to single-point LDV measurements of known accuracy taken in the glycerin tunnel. DBS-PIV and LDV near-wall mean velocity profiles and associated second order statistics are compared for values of $y^+ \leq 30$.

Velocity profile measurements of the undisturbed glycerin tunnel turbulent pipe flow were first carried out by Bakewell (1966) and later carried on by Chevrin (1988) and Fontaine (1993). Chevrin (1988) and Fontaine (1993) used a two-component and three-component LDV, respectively, for their measurements of which only two-component data from Fontaine (1993) will be used here for comparison with the DBS-PIV acquired two-component data. Fountaine's (1993) LDV data were taken using a TSI two-component LDV system in combination with a TSI one-component fiber-optic LDV probe. The mean velocity profile and associated statistics of Fontaine (1993) are based on 50,000 samples at each location per channel.

The wall shear stress and the friction velocity were estimated by Fontaine (1993) at a glycerin temperature of 34.5°C using the average axial pressure gradient measured in the first 7.1 m of the glycerin tunnel test section. Figure 5.6 represents the measured pressure gradient averaged for ten independent samples taken over a period of approximately three hours. The asymptotic nature of the curve shows that the glycerin flow field is fully developed well before the downstream acrylic test section entrance. Using the expression for the wall shear stress for a fully-developed
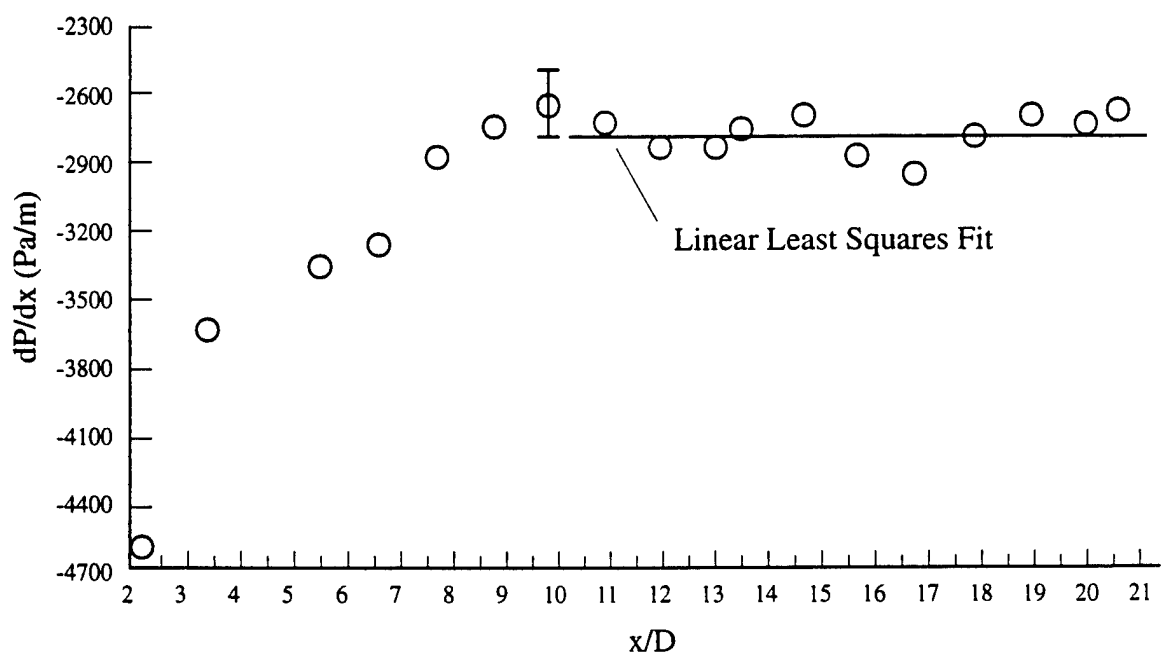
Figure 5.6 Measured axial pressure gradient along the test pipe of the glycerin tunnel

pipe flow, $\tau_w = -\frac{1}{2} R \, dP/dx$, and the definition of friction velocity, u_*, Fontaine (1993) found $u_* = 0.40 \pm 0.01$ m/s. This value is used for the present study.

Two-component PIV velocity measurements were attained nearly coincident in time over a two-dimensional area 1900 wall units (6.8 cm) upstream to 6400 wall units (22.86 cm) downstream of the protrusion by 30 wall units in height. Measurements were taken over this area on the planes corresponding to $z^+ = 0^+$, -5.5^+, -11.0^+ and -17.0^+. For ease of analysis, all data are compared for axial positions within the flow field upstream of the protrusion.

It was desired to determine how close to the wall the present PIV system could resolve velocities. Therefore, PIV velocity estimates were made for $2.5 \le y^+ \le 30.0$. The upper limit of $y^+ = 30$ is a result of the overall system magnification, laser light attenuation and the logistics in handling and interrogating large amounts of data. All velocity data herein are nondimensionalized by the friction velocity, u_*.

5.2.2 Velocity Profile Statistics and Comparison

5.2.2.1 2-D Vector Plot

Figure 5.7 is a vector plot of the average velocity field for x^+ approximately -150^+ to -55^+, 7 cm to 2.5 cm upstream of the protrusion, for $y^+ \le 30$. The averages are based upon a maximum of 65 values; one value is possible for each of the 65 images processed per interrogation spot location. Dropouts and/or bad vectors typically reduced the number of values available from roughly 20 samples to no more than 65 samples, with an average sample size of 50 per interrogated spot. This plot is useful in showing the two-dimensional nature of the data at one instant in time. It
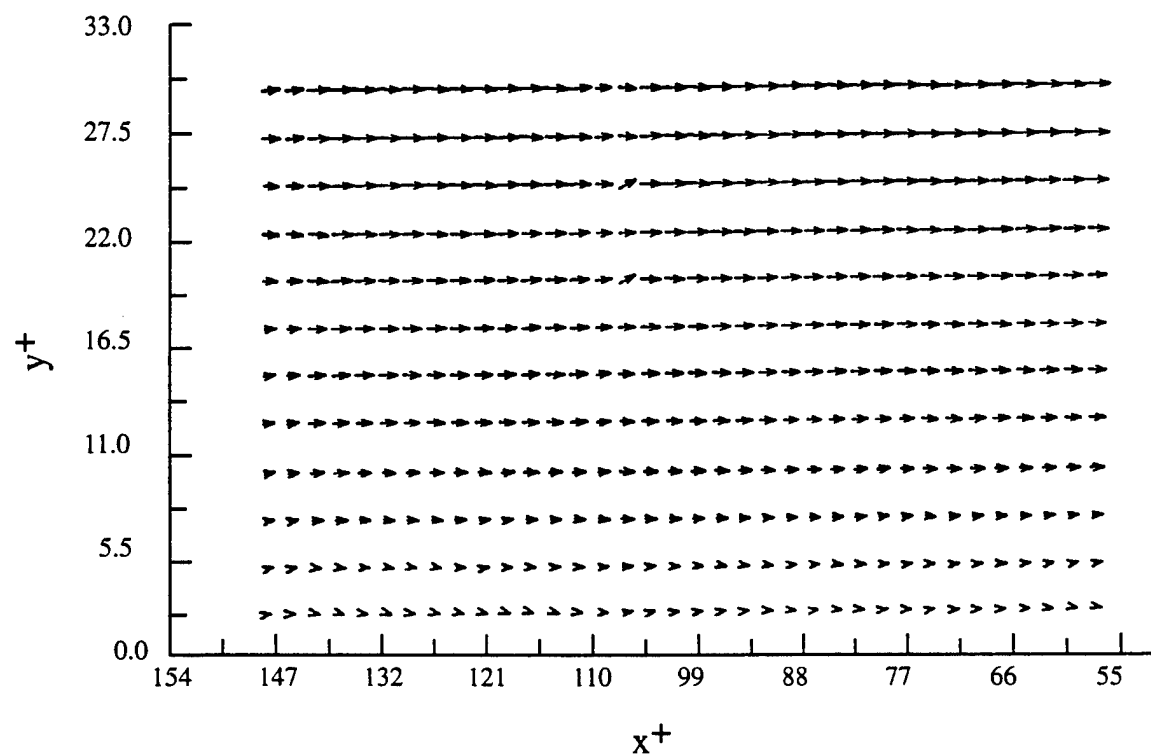
Figure 5.7 Typical vector plot of undisturbed velocity field before protrusion

also exhibits the variation in velocity components from position to position due to a low number of ensembles.

Using typical average rms u' and v' velocity fluctuations for an average ensemble size of 50, the statistical uncertainties of the velocity values in Figure 5.7 found using the standard student t-test are approximately $\pm$ 48% and $\pm$ 16% of the local average velocities for $y^+ = 2.5$ and $y^+ = 30$, respectively. The corresponding statistical uncertainty using the smallest observed ensemble size are $\pm$ 95% and $\pm$ 32% of the local velocities at $y^+ = 2.5$ and $y^+ = 30$, respectively. The bias uncertainties for velocities normalized by wall variables are 18% and 6.5% of the average velocities at $y^+ = 2.5$ and $y^+ = 30$, respectively. Note the two vectors in Figure 5.7 which are most certainly incorrect at $x^+ \approx 100$ and y^+ values of around 20 and 25. These vectors have a low number of ensembles and have a number of bad vectors which have not been filtered out of the correlation process. However, these large perturbations from the surrounding mean values are an exception. The other averages fall within the uncertainty bounds. There is a greater variability in the velocities near the wall relative to velocities further away from the wall. This is due to the higher uncertainties near the wall and the smaller average velocities. Larger sample sizes would in part resolve this uncertainty. Much of the variability is attributed to image distortion very near the test section wall.

5.2.2.2   Velocity Line Averages

For the present PIV data shown in Figure 5.8 through Figure 5.11, computed mean velocities were averaged along lines of constant y^+ in individual photographs in order to decrease the random error associated with a small number of ensembles. This

is justified on the assumption that the flow is fully-developed and statistically homogeneous in the x-direction. The line average from each photo is ensemble averaged with the line average at the same y^+ from the other photographs.

A PIV determined mean U^+ velocity profile is shown in Figure 5.8. The PIV profile is compared with LDV data measured by Fontaine (1993) in the glycerin tunnel and PIV data by Eggels (1994) in a 9.50 cm diameter pipe with air as the fluid medium and a Reynolds number $Re_D = 5450$. Eggles (1994) was able to obtain velocity information from $y^+ = 11$ to the pipe centerline. The viscous sublayer velocity profile and the law of the wall profiles are (Tennekes and Lumley (1972)),

$$U^+ = y^+, \quad when \ y^+ < 5.0$$
$$U^+ = 2.5\ln(\ y^+ \ ) + 5.5, \quad when \ y^+ > 30.0 \qquad 5.1$$

These profiles are included in Figure 5.8 for comparison.

It should be noted that, when line averaging all velocities at a constant y^+, all the ensembles are no longer statistically independent. This is because they are taken at the same instant in time and are close together, roughly a little more than a millimeter separates successive values. Since spatially near ensembles are only separated by a little more that the Kolmogorov length scale, they surely remain correlated. To insure use of only independent samples for line averaging would require knowledge of an integral length scale within the flow field. Then, only velocity ensembles that are separated by at least the integral length scale would be averaged. The effect would significantly reduce the number of ensembles used during the line averaging process.

Grant and Owens (1990) review methods to determine confidence interval estimates for PIV measurements of turbulent flows. Errors are divided into random
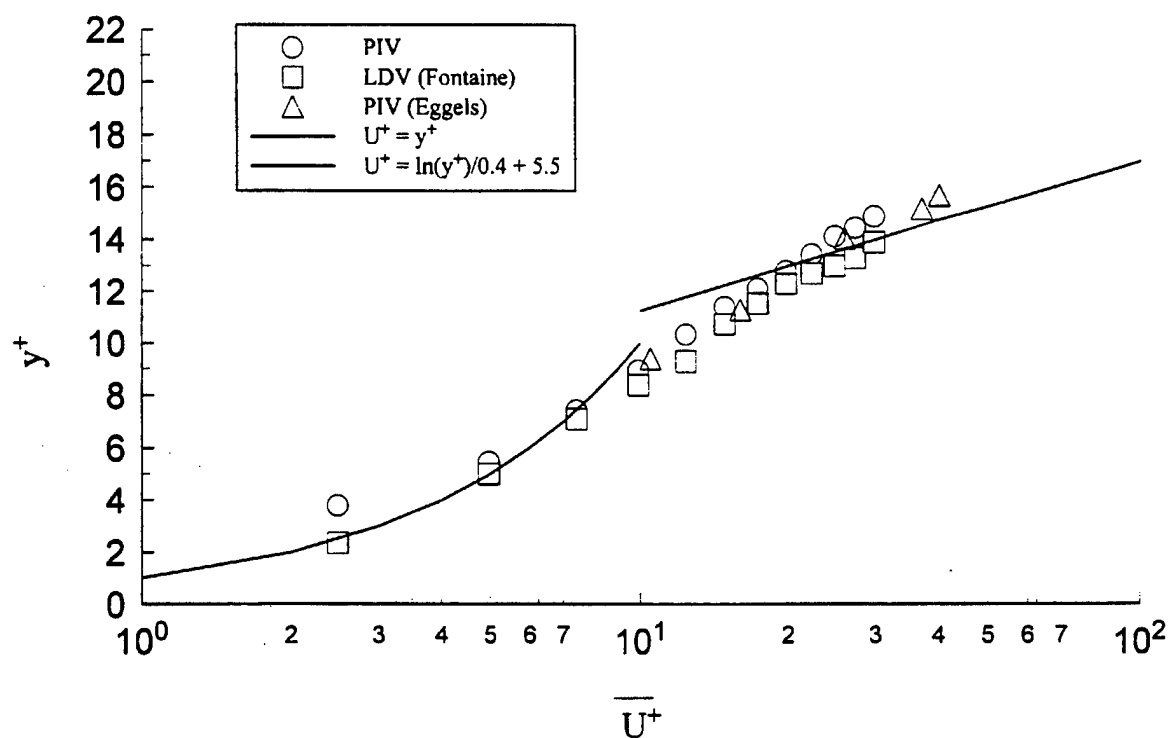
Figure 5.8   Typical streamwise mean velocity profile measured in the undisturbed
glycerin tunnel turbulent boundary layer. Data normalized by
wall variables.

and biased errors or errors associated with statistical uncertainty and with the measurement system, respectively. Using the method detailed by Grant and Owens (1990), the random error associated with the maximum line average sample size of 2340 and a confidence interval of 95% are 1.8% and 0.7% of the average U^+ velocities at $y^+= 2.5$ and $y^+= 30$ respectively. The corresponding V^+ random errors are approximately 1.2% to 0.3%. Bias error due to the measurement system itself are the same as above, approximately 18% and 6.5% of the average U^+ velocities at $y^+ = 2.5$ and 30, respectively, using the generalized method detailed by Coleman and Steele (1989).

The mean streamwise velocity profiles from the present PIV measurements are in good agreement with the law of the wall predictions and with Fontaine (1993) data up to $y^+ = 30$. All values are within the approximate experimental uncertainty of 4.0% of Fontaine's data except for the $y^+ = 2.5$ data point. This value is approximately 25% higher than Fontaine (1993) values. Fontaine (1993) found that at values of y^+ less than 4, curvature effects of the test section wall modified the LDV beam crossover and hence the velocity measurements. He was able to correct for this in the data reduction process for the mean velocity values. PIV calibration files consisting of only predetermined image shift false velocities also show elevated values in this region. PIV values could also be empirically corrected, although this is not attempted here.

It is interesting to note the slightly better agreement of the glycerin tunnel PIV mean streamwise velocity data with the PIV data of Eggels (1994) near the edge of the buffer region and into the logarithmic region. Both the present PIV data and that of Eggels (1994) intersect the law of the wall theoretical curve at a y^+ value of approximately 22 and follow above the law of the wall at a slope of approximately 1/0.4. This slope is inferred for the present PIV data, yet considered a good

approximation if one extrapolates from the general trend between all data sets. The data of Fontaine (1993) intersect the law of the wall theoretical curve at approximately $y^+ = 40$, taking into account uncertainties predicted for the data set. Though not represented in Figure 5.8, Chevrin (1988) gives velocity profile data taken in the glycerin tunnel which also intersect the law of the wall value at $y^+ \approx 22$ to 25. However, the present PIV data is approximately 3% larger than Fontaine's (1993) average U^+ at $y^+ = 30$, within the uncertainty bounds of both data sets. Any differences between the data sets in this region may not be real.

Figure 5.9 is a comparison between the LDV mean normal velocity, V^+, component from Fontaine (1993) and the present PIV results. Since the flow is fully-developed, $V^+ \approx 0$ for all y^+. Differences between the two sets of data are as large as 8% of the friction velocity, the largest differences occurring near y^+ values of 8 and above 25. However, all measured PIV values of V^+ are approximately zero within the described experimental uncertainty.

A one pixel displacement within pixel space corresponds to an approximate 0.268 m/s (0.670^+) change in velocity at $y^+ = 30$ and 0.259 m/s (0.648^+) at $y^+ = 2.5$. No PIV measured normal component averages are greater than 0.066 m/s (0.166^+). Therefore, all values of averaged V^+ within this region of the pipe flow field are more accurate than single pixel accuracy. Velocity values below $y^+ \approx 8$ are known to be affected by the curvature of the test section wall by elevating normal component velocities and possibly the streamwise components also. Above $y^+ \approx 25$ image pairs are known to be more sparse due to beam attenuation and decreased accuracy results (Landreth and Adrian (1990)). These are both factors contributing to differences between the data sets. To date, the author has not found published PIV data detailing the v-component of a turbulent pipe flow by which to compare velocity values.
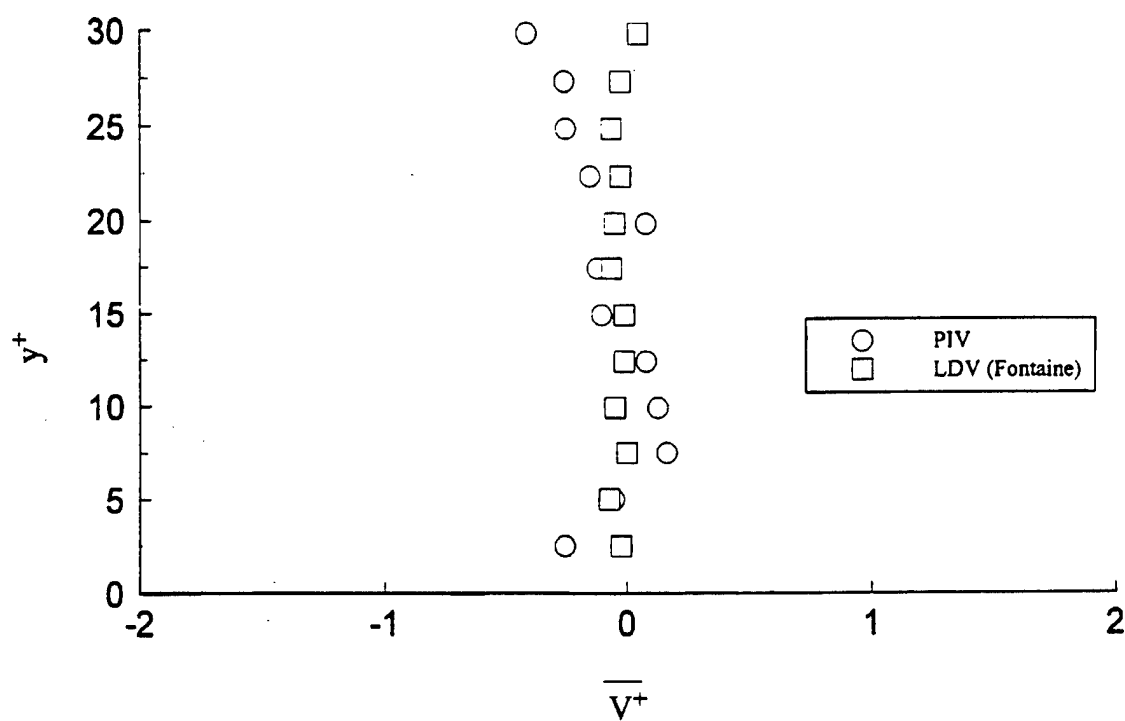
Figure 5.9   Typical vertical mean velocity profile measured in the undisturbed glycerin tunnel turbulent boundary layer. Data normalized by wall variables

It should be noted that the Kolmogorov velocity scale, u ≈ 0.23 m/sec, is approximately the same as the velocity resolution corresponding to one pixel displacement (0.26 m/s). Using the Kolmogorov velocity as a lower bound and the largest measured average velocity of 6 m/s as an upper bound, the dynamic range of the system is found to be approximately 20:1, which is in agreement with predictions made by Adrian (1988).

Profiles of the PIV measured rms velocities, u'^+ and v'^+, are shown in Figure 5.10 and compared to values from Fontaine (1993). Any differences in the rms data are due to differences in measurement systems and uncertainty since the facility and the flow conditions are the same.

PIV values of u'^+ follow the LDV trend well within experimental uncertainty for $5 < y^+ < 25$. Below $y^+ = 5$ the u' data are likely affected by the lens effect of the curved test section wall, producing elevated values. Statistical uncertainties for PIV values of both u'^+ and v'^+ are approximately ± 2.8% of the average value at each y^+ while the bias uncertainties are the same as for the average velocity components. The corresponding total statistical and bias LDV uncertainties in the LDV data are higher, 8.0% of the local average; any differences in the data sets fall with the combinded error bands of both data sets . Above $y^+ > 25$, there are slight deviations between the two u'^+ data sets. Similar deviations are found in PIV measured u'^+ data in Eggles (1994). Deviations may be a function of the relatively low number of ensembles used for the PIV measurements relative to the large sample size, a maximum of 2340 samples versus 50,000 respectively, used for the LDV measurements. The greater PIV random error combined with more prevalent vector dropout near y+ of 30, due to severe laser attenuation, may accentuate the deviations between the LDV and PIV u'^+ data sets. The deviations are, however, within the combined uncertainties of the PIV and LDV data sets.
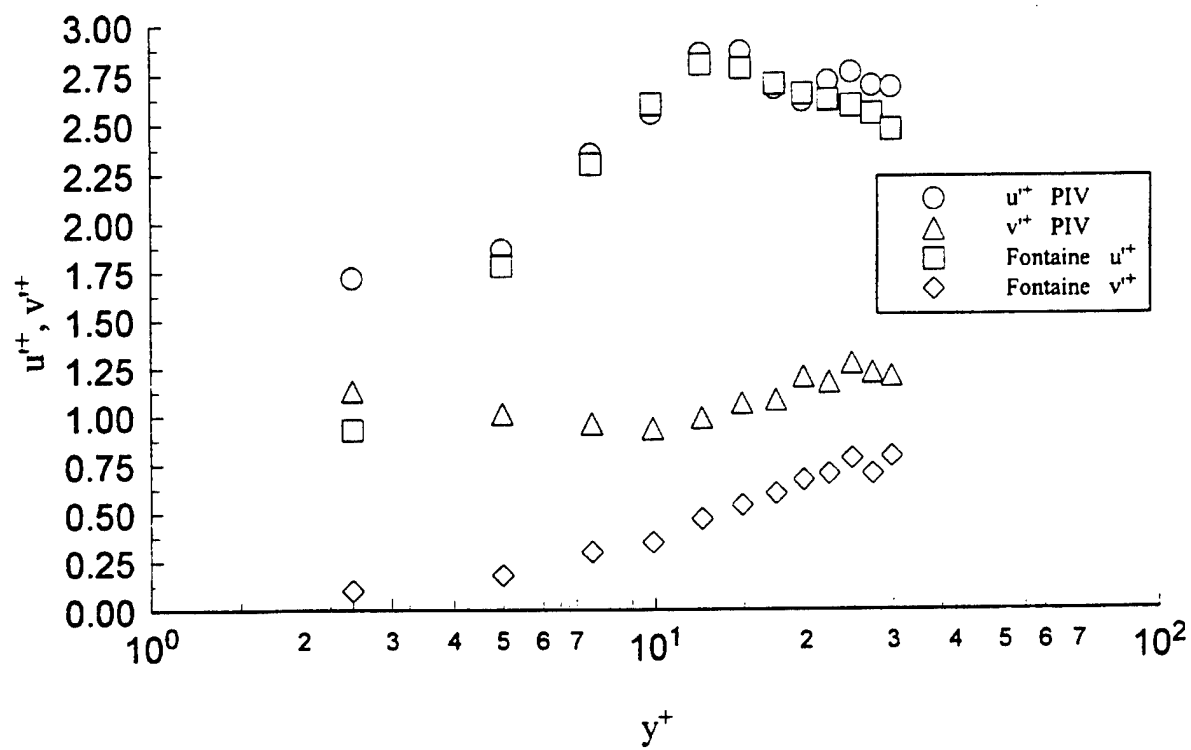
Figure 5.10   Measured rms velocities in the undisturbed glycerin tunnel
turbulent boundary layer. Data normalized by wall variables

All PIV measured values of v'^+ in Figure 5.10 are elevated from those measured with the LDV of Fontaine (1993). Though not shown, v'^+ values from Eggles (1994) are also elevated with respect to corresponding LDV values. For PIV measurements above $y^+ \approx 10$, values of v'^+ are elevated by an approximate constant $\Delta v'^+ \approx 0.5^+$ to 0.6^+. This elevation is believed to be caused by bias errors due to the irregular image shapes and sizes and poor image to background contrast. This elevation is considered a noise floor of the data.

The noise floor was quantitatively found using a "synthetic" particle image field of known particle image diameter, known mean particle image spacing in x and y with prescribed rms levels. When analyzing the synthetic particle image field with particle image densities similar to densities used for actual data, with the current interrogation software, measured mean values in x and y are determined to within 1% of their prescribed values and measured rms levels are typically within 2% of their prescribed values. These results are generally independent of whether the mean synthetic particle image field is prescribed to look like the mean particle image field of actual flow field data or no motion image shift only particle image fields. However, when an actual image shift only particle image field is interrogated, rms levels are approximately 30 times larger in pixel space than the corresponding image shift only synthetic image field rms levels. The rms level increase, created by the irregular image shapes and sizes, translates into an approximate $\Delta v'^+$ of 0.5 to 0.6. This elevation in rms levels also effects the actual flow field rms levels as seen in Figure 5.9. The $\Delta u'^+$ levels are in general not affected since they are above the noise floor.

Values of v'^+ below $y^+ \approx 10$ are also biased toward higher rms levels created by poor image to background contrast, irregular image shapes and optical aberrations associated with the test section wall curvature as noted earlier. Kline and Deutsch

(1992) reported elevated v'^{+} values near the wall but observed correct Reynolds shear stress term values, defined as $-uv/u^{*2}$, with LDV velocity data. They showed that the elevated v'^{+} values occurred due to physical vibrations of their apparatus adding a periodic input to the u'^{+} and v'^{+} velocities. It is possible that this is also the case for the PIV data. The accuracy in resolving the v'^{+} values for the glycerin tunnel flow field with PIV can be improved by using smaller particle sizes, either during acquisition or interrogation, and/or an improved seeding method.

A typical nondimensional Reynolds stress profile, $-\overline{uv}/u^{*2}$, is plotted with LDV measured values from Fontaine (1993) in Figure 5.11. The uncertainty bounds on the LDV data are approximately $\pm$ 9.5 % of the average value at each y^{+}, while the PIV total uncertainty is approximately ±13 %, using a maximum of 2340 ensembles, of the average value at each y^{+}. Except for a few elevated values, the PIV values at y^{+} >8 generally follow the LDV data to within the combined experimental uncertainty of both data sets.

Interestingly, the PIV Reynolds stress profile agreement is not bad even though the v'^{+} values are elevated. For this to occur, any large fluctuations, i.e., large values of u'^{+} and v'^{+}, would have to correlate and control the Reynolds stress. Elevated average v'^{+} levels, as discussed above, result from a more or less "random" bias that does not correlate with u'^{+} and hence does not add to the correlation. Furthermore, the effective number of ensemble averages defining the correlation value is smaller than the recorded number of ensembles as seen in the variability of a number of $-\overline{uv}/u^{*2}$ values close to the combined estimated uncertainty bounds of both data sets.
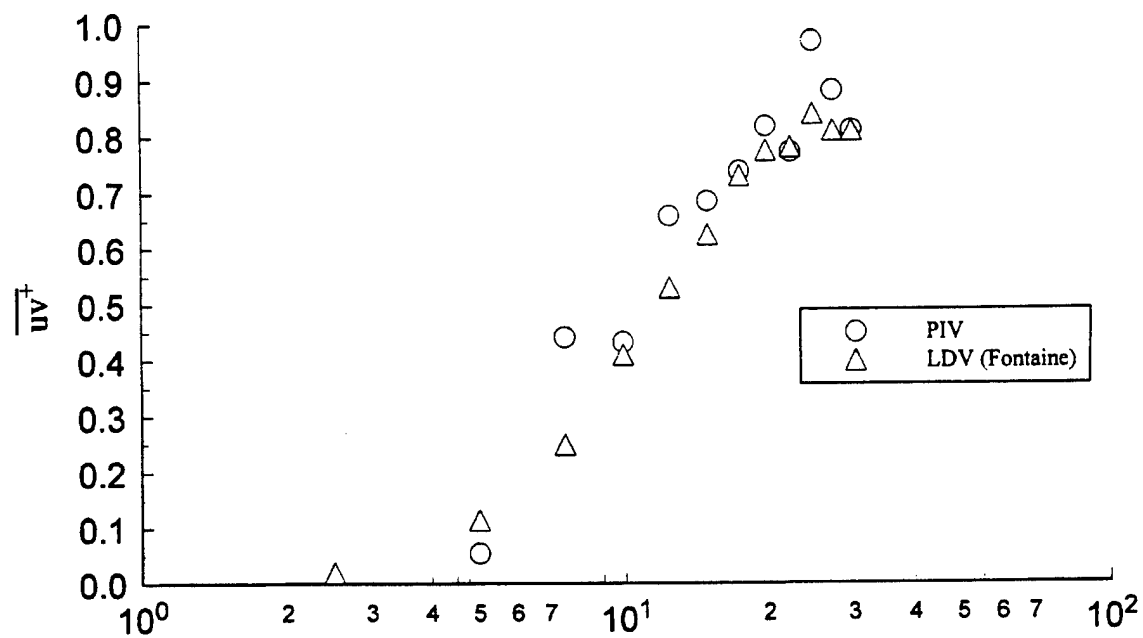
Figure 5.11   Typical $\overline{uv}^+$ Reynolds stress profile measured in the undisturbed glycerin tunnel boundary layer. Data normalized by wall variables

Chapter 6

SUMMARY AND CONCLUSIONS

6.1 Summary

A general PIV system is composed of two parts, the data acquisition system and the data interrogation system. In the present system, the data acquisition process is based upon the rotating beam illumination scheme known as dual beam sweep DBS-PIV. Two continuous laser beams are swept through the area of interest by a rotating mirror effectively creating a laser light sheet. Seed particles which are illuminated by the light sheet are recorded on medium format photographic film for interrogation of their displacements.

Photographic information is digitized using a CCD camera, long range microscope and frame grabber connected to a personal computer. Once digitized, particle images are digitally processed to increase the contrast between real images and background illumination. Image processing reduces the number of occurrences of vector dropout.

The data interrogation process is based upon the method of 2-D spatial cross-correlations to determine the statistically averaged particle displacement per interrogation region. Conventional 2-D spatial cross-correlation techniques generally correlate every pixel within the interrogation region to all other pixels within the region. To reduce the number of pixels considered in the present 2-D spatial cross-correlation, a small extended search region is defined and used during the interrogation process which considers only exposed pixels. Furthermore, because the extended search region is not bound by the interrogation region, the effective image

density is increased over conventional correlation techniques.

All parameters such as interrogation region size, search region size, step size between successive interrogation region locations, and interrogation region overlap are variable so as to optimize the correlation process with respect to a specific flow field, seeding density and image quality. In addition, the interrogation software provides the option for graphical inspection of the particle images and the resulting correlation space defining the average particle displacement. This graphical interfacing was useful for optimizing the interrogation process. A weighted interpolation procedure, allowing for multi-connected correlation peaks, is used to estimate the average particle displacement with subpixel accuracy.

Mean velocity profiles in both the streamwise direction and the normal direction are compared to previously acquired LDV data from Fontaine (1993) within the same facility and for the same conditions. Measurements show that the PIV determined mean streamwise velocity data agree with the LDV data for $5 < y^+ < 20$ and are slightly higher than the LDV data for $y^+ \geq 20$. However, the PIV mean streamwise velocity measurements agree with other PIV pipe flow data given by Eggels (1994). Mean v-component data follow Fontaine's LDV data to within the resolution limit of the current PIV setup as do the average Reynolds shear stress term data. The streamwise rms velocities are found to be in good agreement with LDV rms values for $y^+ \geq 8$, while all normal component rms velocities were higher than the corresponding LDV values. It was found that the normal component rms velocities were biased by uncertainties caused by image to background contrast degradation as well as irregular image shapes and sizes.

All data show elevated PIV mean streamwise and normal velocities below $y^+ = 5$. The most probable source of this error is the strong curvature of the test section wall which causes particle image displacements to have some false

displacement bias. This effect can probably be accounted for empirically for PIV as was done by Fontaine (1993) for LDV data.

6.2   Further Development

6.2.1   Particle Image Velocimetry

There are many ways to further improve the present PIV system. Most of these have the potential of improving accuracy and resolution of the velocity results as well as improving system speed.

Quantification of the subpixel accuracy, inherent to the current system, is envisioned as the next task. In this manner, effects on spatial resolution, induced by other parameters such as seeding technique, seeding density, image processing, gradient effects ...etc., may be ascertained and possibly corrected for.

Using the interactive graphical software revealed digital image processing to be important in the present study for improvement of image quality for cross-correlation processing. This is often the case with PIV because of nonuniform background and particle illumination. Glycerin was found to attenuate the laser beams and produce a blooming effect around particle images producing elevated background illumination levels and image overlap. This makes binary thresholding of particle images more difficult. Further image enhancement is needed to properly isolate real image boundaries from the background levels, created by the blooming effect, as well as to detect image overlap. Increased image isolation from the background would also increase the effective seeding density by decreasing uncorrelated background noise associated with each image. This would further the

possibility of increasing the available spatial resolution and therefore would decrease the effect of other errors associated with velocity gradients. Further work within the Applied Research Laboratory has been carried out with respect to these image processing tasks, especially the development of a more sophisticated edge enhancement and detection process.

Because of the uniqueness of the glycerin tunnel facility for studying boundary layer phenomena, it would be advantageous to determine a better seeding material than the glass microballoons. Air bubbles were used first in the glycerin tunnel, but stable bubble sizes were found to be as large as 50 μm and the seeding density needed for PIV could not be obtained. Particles which are 1-5 μm in diameter that fluoresce at another wavelength may require less laser power as found by Sridhar et al. (1991). These particle characteristics would reduce the blooming effect and may allow better image edge detection. Edge detection could be enhanced due to the different color of the fluorescing particles relative to the background. Metal coated particles which are used for LDV seed are also a possible seeding source yet to be tested.

6.2.2 Velocity Field Processing

It is mentioned by Willert and Gharib (1991) that the shape of the interrogation window could be modified from a square shape to one that is more appropriate for a particular flow field. Advantages would include reducing the number of pixels used per interrogation region, reducing gradient bias and improving the spatial resolution on the critical axis. Related to modifying the shape of the interrogation region is actively changing the size of the search region if a "good"

correlation is not found, e.g., no velocity detected. A preliminary study has been attempted with the current PIV system, but has shown thus far that although more valid vectors are detected, more erroneous vectors are produced if the search region is too large.

Though correlation peak thresholding in conjunction with optimization of the interrogation region size was found to significantly improve the frequency of "good" vectors and decrease the number of vector dropouts, further insight into incorporating signal-to-noise ratios and detection ratios as described by Adrian (1991) could possibly increase the frequency of valid vectors.

To use a valid vector detection scheme as described by Adrian (1991), all correlation values must be properly normalized. Normalization is needed so a fixed signal-to-noise ratio, referred to as the detectablility criterion by Adrian (1991) and usually the ratio between the largest correlation peak to either the second highest correlation peak or the background correlation level, can be applied to all correlation processes. Standard correlation methods use the number of exposed pixels within the interrogation region for normalization. This procedure is not entirely correct for cross-correlation processes, which do not use an extended search region, employed with multiple-exposure image data since a bias is introduced into the correlation as the correlation process traverses the interrogation region. This occurs because the total number of pixels which may correlate with an exposed pixel decreases as the correlation process proceeds over the interrogation region in the downstream direction, e.g., the number of samples per average changes, complicating the normalization process. The extended search region cross-correlation bypasses this complication, but another normalization complication arises. The number of exposed pixels now becomes ambiguous as the search region is no longer contained by the interrogation region. Currently, correlation values are normalized by the combined

number of exposed pixels within the interrogation region and within the boundaries defined by the movement of the search region, as seen in Figure 4.5. However, it is unclear that this is the correct method of normalization; further study is needed to evaluate the normalization process.

Error detection during post-processing of velocity data has been used with varying degrees of success by Adrian (1991) and Chakrabarti (1992). Software currently exists for this purpose but has not been used in the present study. The local standard deviation method (LSD) of Chakrabarti (1992) appears to be the simplest applied to published data and is promising. LSD uses the average of the eight surrounding vectors and the local standard deviation of the vectors to define an "allowable" deviation in both magnitude and direction, of a local vector from its neighbors. This process may be tailored to a specific flow field to optimize the process. Some interactive error detection by inspection is still required. The LSD method currently needs valid vectors surrounding the vector in question to determine its validity and to produce a new vector value if needed.

Currently, the five largest peaks within the search region are retained for later use. These peaks however are not now used as possible replacement peaks if the first peak is rejected as a valid value for say by implementation of the LSD method of Chakrabarti (1992). However, Adrian (1991) suggests this as an efficient way of replacing invalid vectors. The idea is that vectors still containing information deduced from the actual flow field, rather than averaging surrounding vectors, is a more reliable method of obtaining a replacement vector.

6.3   Final Comments

The present PIV system is in the development stage and can be significantly improved upon. It has however, been shown to be effective in measuring the fully-developed turbulent pipe flow within the glycerin tunnel facility. The main advantages of the present system are the availability of continuous beam laser power sources and the availability of standard rotating mirror components. Transposing the system upon another flow field should not be difficult assuming proper seeding densities and proper particle images may be obtained.

It is likely that the use of double pulsed Nd:Yag lasers would improve the quality of the glycerin tunnel data. Several velocity corrections associated with continuous beams sweeping through the flow field would be negated. Furthermore, though light sheet attenuation would still exist, a pulsed laser system may reduce the effects of laser beam attenuation, away from the test section wall because of the increase in illumination energy. A 0.01 Joule per pulse Nd:Yag pulsed laser has approximately 7.5 times the energy as the 2.5 watt continuous laser, used for the present study, when taking into account the time it takes the continuous beam to sweep through the image field in one picture frame. Though yet unevaluated, the higher energy output of the pulsed laser may help homogenize the background contrast with respect to particle images throughout the entire image field, reducing image processing related errors.

REFERENCES

Abbott, M., 1994, "The Power of PIV," TSI Seminar on Particle Image Velocimetry.

Adrian, R. J., 1991, "Particle Imaging Technique for Experimental Fluid Mechanics," *Annual Review of Fluid Mechanics*, Vol. 23, pp. 261-304.

Adrian, R. J., 1988, "Statistical Properties of Particle Image Velocimetry Measurements in Turbulent Flow," *Laser Anemometry in Fluid Mechanics, Vol. III (Ladoan Institute Superior Technico, Lisbon, Portugal)*, pp. 115-129.

Adrian, R. J., 1986, "Image Shifting Technique to Resolve Directional Ambiguity in Double-Pulsed Velocimetry," *Applied Optics [Optical Society of America]*, Vol. 25, No. 21.

Adrian, R. J., 1986, "Multi-Point Optical Measurements of Simultaneous Vectors in Unsteady Flow-A Review," *International Journal of Heat and Fluid Flow*, Vol. 7, pp. 127-145.

Adrian, R. J., 1984, "Scattering Particle Characteristics and Their Effects on Pulsed Laser Measurements of Fluid Flow: Speckle Velocimetry vs. Particle Image Velocimetry," *Applied Optics*, Vol. 23, No. 11, pp. 1690-1691.

Agui, J. C., Jimenez, J., 1987, "On the Performance of Particle Tracking," *Journal of Fluid Mechanics*, Vol. 185, pp. 447-468.

Altman, D. B., 1991, "Statistics of Optimal Particle Streak Photography," *Physics of Fluids*, Vol. 3, No. 9.

Antonia, R. A., Teitel, M. J., Kim, L., Browne, L. W. B., 1993, "Low Reynolds Number Effects in a Fully Developed Turbulent Channel Flow," *Journal of Fluid Mechanics*, Vol. 236, pp. 579-605.

Bakewell, H. P., 1966, "An Experimental Investigation of the Viscous Sublayer in Turbulent Pipe Flow," Ph.D. Thesis, The Pennsylvania State University.

Barker, D. B., Fourney, M. E., 1977, "Measuring Fluid Velocities with Speckle Patterns," *Opt. Lett.*, Vol. 1, pp. 135-137.

Buchhave, P., 1992, "Particle Image Velocimetry-Status and Trends," *Experimental Thermal and Fluid Science*, Vol. 5, pp. 586-604.

Chakrabarti, S., 1992, "Development of a Digital-Based Particle Image Velocimetry (PIV) Technique," MS Thesis, Michigan State University.

Chevrin, P. A., 1988, "The Structure of Reynolds Stress in the Near Wall Region of a Turbulent Pipe Flow," Ph.D. Thesis, The Pennsylvania State University.

Cline, C., Deustch, S., 1993, "On Elevated RMS Levels in Wall-Bounded Turbulent Flows when Measured by Laser Doppler Velocimetry," *Experiments in Fluids*, Vol. 15, pp. 130-132.

Coleman, K. W., Steele, W. G., *Experimentation and Uncertainty Analysis for Engineers*, John Wiley and Sons, Inc., New York, 1989.

Dong, R., Chu, S., Katz, J., 1992, "Quantitative Visualization of the Flow Within the Volume of a Centrifugal Pump. Part A: Technique," *Journal of Fluids Engineering*, Vol. 114, pp. 390-403.

Dumoulin, C. L., Souza, S. P., Hart H. R., 1987, "Rapid Scan Magnetic Resonance Angiography," *Magnetic Resonances in Medicine*, Vol. 5, pp. 238.

Eggels, J. G. M., Unger, F., Weiss, M. H., Westerwell, J., Adrian, R. J., Friedrich, R., Nieuwstadt, F. T. M., 1994, "Fully Developed Transient Pipe Flow: A Comparison Between Direct Numerical Simulation and Experiment," *Journal of Fluid Mechanics*, Vol. 268, pp. 175-209.

Farrell, P. V., 1991, "Particle Sizing and Velocity Measurements Using Particle Image Velocimetry," *FLUCOME '91*, ASME, pp. 423-434.

Fincham, A., Blackwelder, R., Spedding, G., Need Year, "Current Constraints of Digital Particle Tracking in Fluid Flows," *American Physics Society*, Vol. 36, No. 10, p. 2692.

Fontaine, A. A., 1993, "Suppression of the Near Wall Burst Process of a Fully-Developed Turbulent Pipe Flow," Ph. D. Thesis, The Pennsylvania State University.

Fingerson, L. M., Adrian, R. J., Menon, R. K., Kaufman, S. L., 1991, "Data Analysis, Laser Doppler Velocimetry and Particle Image Velocimetry," TSI Short Course Text.

Gharib, M., Willert C., 1988, "Particle Tracing: Revisited," First National Fluid Dynamics Conference, pp. 1935-1943.

Gharib, M., Willert C., 1989, "Particle Tracking: Revisited," in Advances Fluid Mechanics Measurements, Edited by Gad-el-Hak, Springer Verlag, pp. 109-199.

Goodman, J. W., *Introduction to Fourier Optics*, McGraw-Hill, New York, 1968.

Gonzales, R. C., Woods, R. E., *Digital Image Processing*, Addison-Wesley, 1992.

Grant, I., Liu, A., 1990, "Directional Ambiguity Resolution in Particle Image Velocimetry by Pulse Tagging," *Experiments in Fluids*, Vol. 10, pp. 71-76.

Grant, I., Owens, E. H., 1990, "Confidence Interval Estimates in PIV Measurements of Turbulent Flows," *Applied Optics*, Vol. 29, No. 10, pp. 1400-1402.

Grant, I., Zhao, Y., Tan, Y., Stewart, J. N., 1991, "Three Component Flow Mapping: Experiences in Stereoscopic PIV and Holographic Velocimetry," *Laser Anemometry*, Vol. 1, ASME.

Grant, S., 1992, Internal Correspondence, Applied Research Laboratory, The Pennsylvania State University.

Guezennec, Y. G., Kiritsis, N., 1990, "Statistical Investigation of Errors in Particle Image Velocity," *Experiments in Fluids*, Vol. 10, pp. 138-146.

Hassan, Y. A., Canaan, R. E., 1991, "Simultaneous Velocity Field Measurements of Bubbles and Surrounding Fluid by Pulsed Laser Velocimetry," *Laser Anemometry*, Vol. 1, pp. 387-401.

Huang, H. T., Fiedler, H. E., Wang, J. J, 1993, "Limitation and Improvement of PIV. Part I: Limitation of Conventional Techniques Due to Deformation of Particle Image Patterns," *Experiments in Fluids*, Vol. 15, pp. 168-174.

Johnson, S. A., et al., 1976, "Reconstructing Three-Dimensional Fluid Velocity Vector Fields from Acoustic Transmission Measurement," *Acoustical Holography*, Vol. 7, pp. 307-326.

Kawahashi, M., Hosoi, K., 1991, "Dual-beam-sweep laser speckle velocimetry," *Experiments in Fluids*, Vol. 11, pp. 278-280.

Keane, R. D., Adrian, R. J., 1990, "Optimization of Particle Image Velocimeters: Part I. Double Pulsed Systems," *Measurement Science and Technology*, Vol. 1, pp. 1202-1215.

Keane, R. D., Adrian, R. J., 1991, "Optimization of Particle Image Velocimeters: Part II. Multiple Pulsed Systems," *Measurement Science and Technology.*, Vol. 2, pp. 963-974.

Kim, Y. G., 1991, "Quantitative Flow Visualization and Numerical Simulation of Lid Driven Rotating Flow," Ph.D. Dissertation, Department of Mechanical Engineering, The University of Iowa.

Kimura, Takamori, 1986, "Image Processing of Flow Around a Circular Cylinder by Varying a Correlation Technique," *Proceedings of the Fourth International Symposium on Flow Visualization I*, Hemisphere Publ. Co., pp. 221-226.

Komine, H., Brosnan, S. J., 1991, "Instantaneous, Three-Component Doppler Global Velocimetry," *Laser Anemometry*, Vol. 1, ASME.

Landreth, C. C., Adrian, R. J., 1990, "Measurement and Refinement of Velocity Data Using High Image Density Analysis in Particle Image Velocimetry," *Applications of Laser Anemometry to Fluid Mechanics (ed. R. J. Adrian et al.)*, pp. 484-497, Springer.

Laurenco, L., 1986, "Theory and Applications of Particle Image Displacement Velocimetry," von Karman Institute for Fluid Dynamics Lecture Series 1986-09, Flow Visualization and Image Processing, (J.-M. Buchlin, dir.).

Lourenco, L. M., Krothapalli, A., Smith, C. A., 1989, "Particle Image Velocimetry Advances in Fluid Mechanic Measurements," (Lecture notes in Engineering 45, Ed. M. Gad-el-Hak, Springer-Verlag), pp. 127-199.

Lourenco, L. M., Krothapalli, A., 1987, "The Role of Photographic Parameter in Laser Speckle of Particle Image Displacement Velocimetry," *Experiments in Fluids*, Vol. 5, pp. 29-32.

Lourenco, L. M., Krothapalli, A., 1986, "Noninvasive Experimental Technique for the Measurements of Unsteady Velocity Fields," *AIAA Journal*, Vol. 24, No. 10, pp. 1715-1717.

Merzkirch, W., *Flow Visualization*, Second Edition, New York, Hartcourt Bruce Jovanovich, 1987.

Post, M. E., Trump, D. D., Goss, L. P., Hanock, R. D., 1994, "Two-Color Particle Image Velocimetry Using a Single Argon-ion Laser," *Experiments in Fluids*, Vol. 16, pp. 263-272.

Prandtl, L., Tietjens, O., 1934, *Applied Hydro and Aerodynamics*, Dover.

Prasad, A. K., Adrian, R. J., Landreth, C. C., Offutt, P. W., 1992, "Effect of Resolution on Speed and Accuracy of Particle Image Velocimetry Interrogation," *Experiments in Fluids*, Vol. 13, pp. 105-116.

Rockwell, D., Magness, C., Towfighi, J., Akin, O., Corcoran, T., 1993, "High Image-Density Particle Image Velocimetry Using Laser Scanning Techniques," *Experiments in Fluids*, Vol. 14, pp. 183-192.

Rubinow, S. I., Keller, J. B., 1961, "The Transverse Force on a Spinning Sphere Moving in a Viscous Fluid," *Journal of Fluid Mechanics*, Vol. 11, pp. 447-459.

Shekarriz, A., Fu, T. C., Katz, J., Liu, H. L., Huang, T. T., 1992, "Study of Junction and Tip Vortices Using Particle Displacement Velocimetry," AIAA Journal, Vol. 30, No. 1, pp. 145-152.

Simpkins, P. G., Dudderan, T. D., 1978, "Laser Speckle Measurements of Transient Benard Convection," *Journal of Fluid Mechanics*, Vol. 89, pp. 665-671.

Sinha, S. K., 1988, "Improving the Accuracy and Resolution of Particle Image or 'Laser' Speckle Velocimetry," *Experiments in Fluids*, Vol. 6, pp. 67-68.

Spalding, D. B., 1961, "A Single Formula for the Law of the Wall," *Journal of Applied Mechanics*, Vol. 28, pp. 455-457.

Sridhar, G., Ran, B., Katz, J., 1991, "Implementation of Particle Image Velocimetry to Multi-Phase Flow," *Cavitation and Multiphase Flow Forum*, ASME, Vol. 109, pp. 205-210.

Taylor, A. M. K. P., 1992, "Optically-Based Measurement Techniques for Dispersed Two-Phase Flows," in *Combustion Flow Diagnostics,* R. F. G. Durao, Editor, Kluwer Academic Publishers, Amsterdam, pp. 233-289.

Tennekes, H., Lumley, J. C., *A First Course in Turbulence*, MIT Press, 1972.

Wei, T., Willmouth, W. W., 1989, "Reynolds Number Effects on the Structure of a Turbulent Channel Flow," *Journal of Fluid Mechanics*, Vol. 204, pp. 57-95.

White, F. M., *Viscous Fluid Flow*, McGraw-Hill, 1974.

Willert, C. E., Gharib, M., 1991, "Digital Particle Image Velocimetry," *Experiments in Fluids*, Vol. 10, pp. 181-193.

ARL

H. L. Petrie
S. Deutsch
A. A. Fontaine
M. L. Billet
K. J. Farrell
M. W. McBride
T. E. McDevitt
M. L. Jonson
G. C. Lauchle
T. A. Brungart
D. E. Capone
M. J. Erickson
T. Cawley
R. S. Meyer
S. D. Young
E. C. Myer
H. L. Petrie